

13 **Abstract**

14 Land evapotranspiration (ET) plays a crucial role in Earth's water-carbon cycle, and
15 accurately estimating global land ET is vital for advancing our understanding of land-
16 atmosphere interactions. Despite the development of numerous ET products in recent
17 decades, widely used products still possess inherent uncertainties arising from using
18 different forcing inputs and imperfect model parameterizations. Furthermore, the lack
19 of sufficient global in-situ observations makes direct evaluation of ET products
20 impractical, impeding their utilization and assimilation. Therefore, establishing a
21 reliable global benchmark dataset and exploring evaluation methodologies for ET
22 products is paramount. This study aims to address these challenges by (1) proposing a
23 collocation-based method that considers non-zero error cross-correlation for merging
24 multi-source data and (2) employing this merging method to generate a long-term
25 daily global ET product at resolutions of 0.1° (2000-2020) and 0.25° (1980-2022),
26 incorporating inputs from ERA5L, FluxCom, PMLv2, GLDAS, and GLEAM. The
27 resulting product is the Collocation-Analyzed Multi-source Ensembled Land
28 Evapotranspiration Data (CAMELE). CAMELE exhibits ~~excellent~~promising
29 performance across various vegetation coverage types, as validated against in-situ
30 observations. The evaluation process yielded Pearson correlation coefficients (R) of
31 0.63 and 0.65, root-mean-square-errors (RMSE) of 0.81 and 0.73 mm/d, unbiased
32 root-mean-square-errors (ubRMSE) of 1.20 and 1.04 mm/d, mean absolute errors
33 (MAE) of 0.81 and 0.73 mm/d, and Kling-Gupta efficiency (KGE) of 0.60 and 0.65
34 on average over resolutions of 0.1° and 0.25° , respectively. In addition, comparisons
35 indicate that CAMELE can effectively characterize the multi-year linear trend, mean
36 average, and extreme values of ET. However, it exhibits a tendency to overestimate
37 seasonality. In summary, we propose a reliable set of ET data that can aid in
38 understanding the variations in the water cycle and has the potential to serve as a
39 benchmark for various applications.

40 1. Introduction

41 Land evapotranspiration (ET) plays a critical role in the global water and energy
42 cycles, encompassing various processes such as soil evaporation, vegetation
43 transpiration, canopy interception, and surface water evaporation (Zhang et al., 2019;
44 Zhao et al., 2022; Lian et al., 2018). Accurately estimating global land
45 evapotranspiration is vital for understanding the hydrological cycle and land-
46 atmosphere interactions, as it serves as an intermediary variable connecting soil
47 moisture, ~~and~~ air temperature and humidity (Miralles et al., 2019; Gentile et al.,
48 2019). Therefore, providing a reliable ET dataset as a benchmark for further research
49 is crucial.

50 In recent decades, numerous studies have focused on estimating global land
51 evapotranspiration, resulting in many datasets ([Yang et al., 2023](#)). However,
52 discrepancies often arise among these simulations due to algorithm and principle
53 variations (Restrepo-Coupe et al., 2021; Han and Tian, 2020). Additionally,
54 evaluating ET products is challenging due to the limited availability of global-scale
55 observations, which hampers their direct use (Pan et al., 2020; Baker et al., 2021).

56 The fusion of multi-source data is a suitable option to address these uncertainties.
57 Recent studies have explored several approaches to integrate multiple ET products,
58 including Simple Average (SA) (Ershadi et al., 2014), Bayesian Model Average
59 (BMA) (Hao et al., 2019; Ma et al., 2020; Zhu et al., 2016), Reliability Ensemble
60 Average (REA) (Lu et al., 2021), Empirical Orthogonal Functions (EOF) (Feng et al.,
61 2016) and machine-learning-based methods (Chen et al., 2020; Yin et al., 2021).
62 However, the primary challenge lies in calculating reliable input weights based on a
63 selected "truth" (Koster et al., 2021), which can involve averaging or incorporating
64 other relevant geographical information as a benchmark. ~~Moreover, previous research~~
65 ~~has predominantly focused on regional scale ET estimation, necessitating a more~~
66 ~~straightforward and reliable global simulation method.~~

67 Recently, collocation methods have emerged as promising techniques for estimating

68 random error variances and data-truth correlations in collocated inputs [\(Stoffelen,](#)
69 [1998; Li et al., 2022, 2023c; Park et al., 2023\)](#)~~(Stoffelen, 1998; Li et al., 2022, 2023b;~~
70 ~~Park et al., 2023)~~. These methods consider the errors associated with collocated
71 datasets as an accurate representation of uncertainty without assuming the absence of
72 errors in any datasets. It is important to note that while collocation methods, such as
73 [the triple collocation \(TC\)](#) and [the extended double instrumental variable technique](#)
74 [\(EIVD\)](#), can estimate the variance (or covariance) of random errors, they cannot
75 evaluate the bias of the products. One primary advantage of collocation analysis is
76 that it does not require a high-quality reference dataset (Su et al., 2014; Wu et al.,
77 2021). However, a crucial prerequisite for applying collocation methods is the
78 availability of many spatially and temporally corresponding datasets. For instance, the
79 classic ~~triple collocation (TC)~~ method requires a trio of independent datasets. Su et al.
80 (2014) used the instrumental regression method and considered lag-1 time series as
81 the third input, proposing the single instrumental variable algorithm (IVS). Dong et al.
82 (2019) introduced the lag-1 time series from both inputs, proposing the double
83 instrumental variable algorithm (IVD) for a more robust solution. Gruber et al. (2016a)
84 extended the original algorithm to incorporate more datasets, partially addressing the
85 independence assumption to calculate a portion of error cross-correlation (ECC) [_by](#)
86 [using the extended collocation \(EC\) method](#). Dong et al.(2020a) further proposed the
87 ~~extended double instrumental (EIVD)~~ method, enabling ECC estimation using three
88 datasets. Collocation methods have found widespread application in the evaluation of
89 geophysical variable estimates, including soil moisture (Deng et al., 2023; Ming et al.,
90 2022), precipitation (Dong et al., 2022; Li et al., 2018), ocean wind speed (Vogelzang
91 et al., 2022; Ribal and Young, 2020), leaf area index (Jiang et al., 2017), total water
92 storage (Yin and Park, 2021) sea ice thickness and surface salinity (Hoareau et al.,
93 2018), and near-surface air temperature (Sun et al., 2021).

94 Recently, many studies have utilized collocation approaches to evaluate
95 evapotranspiration products, with the TC method to assess uncertainties. For example,

城代码已更改

96 Barraza Bernadas et al. (2018) considered the uncertainties of ET from the Breathing
97 Earth System Simulator, BESS (Jiang et al., 2020; Jiang and Ryu, 2016), Moderate
98 Resolution Imaging Spectroradiometer, MOD16 (Mu et al., 2011), and a hybrid
99 model; Khan et al. (2018) utilized extended triple collocation (ETC) (McColl et al.,
100 2014) to investigate the reliability of ET from MOD16, The Global Land Data
101 Assimilation System (GLDAS) (Rodell et al., 2004) and the Global Land Evaporation
102 Amsterdam Model (GLEAM) (Martens et al., 2017) over East Asia; Li et al. (2022)
103 employed five collocation methods (e.g., IVS, IVD, TC, EIVD, and EC) to analyze
104 the uncertainties of ET from ERA5-Land (ERA5L) (Muñoz-Sabater et al., 2021),
105 GLEAM, GLDAS, FluxCom (Jung et al., 2019), and the Penman-Monteith-Leuning
106 Evapotranspiration V2 (PMLv2) (Zhang et al., 2019).

107 Moreover, error information derived from collocation analysis is valuable for merging
108 multi-source ~~ET~~ data. This was initially applied by Yilmaz et al. (2012) in the fusion
109 of multi-source soil moisture products and later improved by Gruber et al. (2017) and
110 further applied in the production of the European Space Agency Climate Change
111 Initiative (ESA CCI) global soil moisture product (Gruber et al., 2019). Dong et al.
112 (2020b) also adopted this approach to fusing multi-source precipitation products. In
113 the study of evapotranspiration, Li et al. (2023c) and Park et al.(2023) utilized a
114 weight calculation method that does not consider non-zero ECC and fused multiple
115 ET products in the Nordic and East Asia, respectively, achieving satisfactory fusion
116 results.~~Park et al. (2023) combined three reanalysis-based evaporation (E) and~~
117 ~~transpiration (T) estimates (i.e., ERA5L, GLDAS, and MERRA2) to improve the~~
118 ~~accuracy of evapotranspiration (ET) over East Asia. Li et al. (2023c)(2023b)~~
119 ~~combined four products, including FluxCom, Global Land Surface Satellite (GLASS)~~
120 ~~(Liang et al., 2021), GLEAM, and PMLv2, to improve ET accuracy in the Nordic~~
121 ~~Region.~~

122 Although the above studies have demonstrated that collocation analysis can
123 effectively assess the random error variance of ET (~~evapotranspiration~~) products and

域代码已更改

124 integrate error information from multiple data sources, ~~these studies have primarily~~
125 ~~overlooked a critical aspect: non-zero ECC between ET products~~ ~~these studies did not~~
126 ~~consider the issue of non-zero error covariance (ECC) between different ET products.~~

127 Li et al. (2022) ~~'s~~ global ET product evaluation research revealed clear non-zero ECC
128 conditions between ERA5L ~~and GLEAM and PMLV2~~, GLEAM, PMLv2, and
129 ~~FLUXCOM~~FluxCom. In TC analysis, non-zero ECC can result in significant biases in
130 TC-based results (Yilmaz and Crow, 2014). Furthermore, when using TC-based error
131 information for fusion, it is crucial to consider the information related to ECC, as this
132 can help improve the fusion accuracy (Dong et al., 2020b; Kim et al., 2021b).

133 It is worth noting that non-zero ECC conditions pose unique challenges. Unlike other
134 violations of mathematical assumptions adopted by TC, they cannot be effectively
135 mitigated through rescaling or compensated for by equal magnitude adjustments
136 across inputs. Thus, the implications of non-zero ECC in the context of merging
137 strategies are a critical consideration often overlooked in previous research. This
138 oversight can lead to significant biases and inaccuracies. We aim to bridge this gap by
139 systematically accounting for non-zero ECC in weight calculation, contributing to a
140 more robust and accurate assessment.

141 In this study, we proposed a collocation-based data ensemble method, considering
142 non-zero ECC conditions, for merging multiple ET products to create the Collocation-
143 Analyzed Multi-source Ensembled Land Evapotranspiration data, abbreviated as
144 CAMELE. The second section of this paper presents the selected data information for
145 this study. In the third section, we explained the error calculation method for
146 collocation analysis and the weighted calculation method that considered ECC. The
147 fourth section analyzed the global errors of different ET products obtained through
148 these calculations and the distribution patterns of the corresponding weights. We
149 evaluated the accuracy of the fused products and compared them with existing
150 products using reference values from site measurements. In the fifth section, we
151 discussed the inherent errors in the methods, analyzed the ECC between the products,

152 and compared the differences between different fusion schemes. Finally, in the sixth
 153 section, we summarized the results obtained from this research.

154 2. Datasets

155 We selected five widely used ~~land evapotranspiration (ET)~~ products that spanned the
 156 period from 1980 to 2022. When selecting these products, our aims are to ensure: (1)
 157 consistency in original spatiotemporal resolution among the products; minimize
 158 potential downscaling operations and avoid introducing additional errors; (2) having
 159 three or more products within the same resolution or period; incorporate more
 160 information for effective fusion; (3) products with extensive global observational
 161 sequences: gain basic recognition from the community. While we acknowledge the
 162 existence of other higher-precision products, their integration would require either
 163 downscaling or upscaling other products, potentially introducing uncertainties.
 164 Therefore, we chose the combination outlined in the manuscript. Despite its relatively
 165 lower resolution compared to some products, it still contributes to our understanding
 166 of ET variations, facilitating advantageous exploration. Furthermore, we incorporated
 167 in-situ observations Specifically, and Lu et al. (2021) 's global 0.25° daily-scale ET
 168 product derived using Reliability Ensemble Averaging (denoted as REA) was also
 169 selected for comparative analysis. to compare our merged product comprehensively.
 170 ~~Table 1~~ shows the spatial and temporal resolutions of the input datasets.

171 ~~Table 1~~ **TABLE 1** Summary of evapotranspiration products involved.

Name	Schemes	Resolution	Period	Referenc
ERA5-Land	H-TESSSEL	0.1°	hourly	1950-present (Muñoz Sabater et al., 2021)
GLDAS-2	CLSM/Noah /LSM	0.25°	3-hourly daily	2.0: 1948-2014 2.1: 2000-present 2.2: 2003-present (Li et al., 2019a; Rodell et al., 2004)

设置了格式: 字体: (中文) 黑体, 加粗

设置了格式: 字体: (中文) 黑体

设置了格式: 字体: (中文) 黑体, 加粗

设置了格式: 字体: (中文) 黑体, 加粗

设置了格式: 字体: (中文) 黑体

GLEAM-3.7	GLEAM model	0.25°	daily	3.7a: 1980-2022 3.7b: 2003-2022	(Martens et al., 2017)
PMLv2-v017	Penman-Monteith-Leuning	0.083°	8-day average	2000-2020	(Zhang et al., 2019)
FluxCom	Machine learning	0.083°	8-day average	2001-2015	(Jung et al., 2019)

172 2.1. ERA5-Land

173 The European Centre for Medium-Range Weather Forecasts (ECMWF) produces the
174 latest advanced ~~ERA5 Land dataset, referred to as~~ ERA5L, a global hourly reanalysis
175 dataset with a spatial resolution of 0.1°. It covers the period from January 1950 until
176 approximately one week before the present (Muñoz-Sabater et al., 2021). ERA5-Land
177 is derived from the land component of the ECMWF climate reanalysis, incorporating
178 numerous improvements over previously released versions. It is based on the Tiled
179 ECMWF Scheme for Surface Exchanges over Land incorporating land surface
180 hydrology (H-TESSSEL), utilizing version CY45R1 of the ECMWF's Integrated
181 Forecasting System (IFS). The dataset benefits from atmospheric forcing data, which
182 acts as an indirect constraint on the model-based estimates (Hersbach et al., 2020).
183 The dataset is available through the Climate Change service of the Copernicus Center
184 at <http://cds.climate.copernicus.eu>.
185 Evapotranspiration in ERA5L, defined as "total evaporation," represents the
186 accumulated amount of water that has evaporated from the Earth's surface, including a
187 simplified representation of transpiration from vegetation into the vapor in the air.
188 The soil water and energy balance are computed using standard soil discretization.
189 Readers could consult section 8.6.5 of the IFS documentation (ECMWF, 2014). The
190 original dataset is interpolated from (1801, 3600) to (1800, 3600) using kriging
191 interpolation and then upscaled from an hourly to a daily resolution, changing spatial
192 resolution from 0.1° to 0.25°.

193 **2.2. GLDAS**

194 The Global Land Data Assimilation System (GLDAS) product utilizes advanced data
195 assimilation methodologies, integrating model and observation datasets for land-
196 surface simulations (Rodell et al., 2004). GLDAS employs multiple land-surface
197 models (LSMs), namely Noah, Mosaic, Variable Infiltration Capacity (VIC), and the
198 Community Land Model (CLM). Together, these models generate global
199 evapotranspiration estimates at fine and coarse spatial resolutions (0.01° and 0.25°)
200 and temporal resolutions (3-hourly and monthly). The most recent iteration of
201 GLDAS, version 2, consists of three components: GLDAS-2.0, GLDAS-2.1, and
202 GLDAS-2.2. GLDAS-2.0 relies entirely on the Princeton meteorological forcing input
203 data, providing a consistent temporal series from 1948 to 2014 (Sheffield et al., 2006).
204 The GLDAS-2.1 simulation commences on January 1, 2000, utilizing the conditions
205 from the GLDAS-2.0 simulation. On the other hand, GLDAS-2.2 is simulated from
206 February 1, 2003, employing the conditions from GLDAS-2.0 and forcing with
207 meteorological analysis fields from the ECMWF Integrated Forecasting System (IFS).
208 Additionally, the GRACE satellite's total terrestrial water anomaly observation is
209 assimilated into the GLDAS-2.2 product (Li et al., 2019a).

210 [This study aimed to cover the research period from 1980 to 2022. Non-zero ECC](#)
211 [between the transpiration estimates of GLDAS-2.2 and ERA5L has been reported in a](#)
212 [recent study \(Li et al., 2023a\). Considering the similarities in the calculation of ET](#)
213 [and transpiration of GLDAS and ERA5L, this report partially indicates a correlation.](#)
214 [Therefore, GLDAS-2.0 and GLDAS-2.1 were selected as inputs instead. The](#)
215 ["Evap_tavg" parameter representing evapotranspiration is derived from the original](#)
216 [products and aggregated to a daily scale. For more detailed information on the](#)
217 [GLDAS-2 models, please refer to NASA's Hydrology Data and Information Services](#)
218 [Center at <http://disc.sci.gsfc.nasa.gov/hydrology>.](#)
219 [Despite the same forcing between GLDAS-2.1 and GLDAS-2.2, significant](#)
220 [differences exist between the model results of different GLDAS versions \(Qi et al.,](#)

域代码已更改

221 [2020, 2018; Jiménez et al., 2011](#)). The non-zero ECC will generally still be met
222 [between different versions. Thus, we still need to analyze the non-zero ECC situations](#)
223 [between ERA5L and GLDAS-2.0 and 2.1, which will be assessed in the discussion](#)
224 [sections.](#)

225 ~~In this study, to cover the research period from 1980 to 2022 and address potential~~
226 ~~error homogeneity issues between GLDAS 2.2 and ERA5L (both utilizing ECMWF~~
227 ~~meteorological driving data), we selected GLDAS 2.0 and GLDAS 2.1 as inputs. The~~
228 ~~"Evap_avg" parameter representing evapotranspiration is derived from the original~~
229 ~~products and aggregated to a daily scale. For more detailed information on the~~
230 ~~GLDAS 2 models, please refer to NASA's Hydrology Data and Information Services~~
231 ~~Center at <http://disc.sci.gsfc.nasa.gov/hydrology>.~~

232 **2.4.2.3. GLEAM**

233 The ~~latest~~ version of the Global Land Evaporation Amsterdam Model 3.7 (GLEAM-
234 3.7) dataset (Martens et al., 2017; Miralles et al., 2011) at 0.25° is used. This version
235 of GLEAM provides daily estimations of actual evaporation, bare soil evaporation,
236 canopy interception, transpiration from vegetation, potential evaporation, and snow
237 sublimation ~~from 1980 to 2022~~. The third version of GLEAM contains a new DA
238 scheme, an updated water balance module, and evaporative stress functions. Two
239 datasets that differ only in forcing and temporal coverage are provided:
240 GLEAMv3.7a-43-year period (1980 to 2022) based on satellite and reanalysis
241 (ECMWF) data; GLEAMv3.7b-20-year period (2003 to 2022) based on only satellite
242 data. GLEAMv3.7a is used in this study. The data are freely available on the GLEAM
243 website (<https://www.gleam.eu>).

244 The cover-dependent potential evaporation rate (E_p) is calculated using the Priestley-
245 Taylor equation (Priestley and TAYLOR, 1972). Then a multiplicative stress factor is
246 used to convert E_p into actual transpiration ~~or and~~ bare soil evaporation, which is the
247 function of microwave vegetation optimal depth (VOD) and root-zone soil moisture.

域代码已更改

248 For detailed description, please refer to the paper by [Martens et al., \(2017\)](#)(~~Martens et~~
249 ~~al., 2017~~). The GLEAM data were validated at 43 FluxNet flux sites and have been
250 proven to provide reliable AET estimations (Majozi et al., 2017).

251 2.5.2.4. PMLv2

252 The Penman-Monteith-Leuning version 2 global evaporation model (PMLv2) has
253 been developed based on the Penman-Monteith-Leuning model (Zhang et al., 2019;
254 Leuning et al., 2009). Initially proposed by Leuning et al. (2008), the PML model
255 underwent further enhancements by Zhang et al. (2010). The PML version 1 (PMLv1)
256 incorporates a biophysical model that considers canopy physiological processes and
257 soil evaporation to estimate surface conductance accurately (G_s), which is the focus of
258 the PM-based method. This version was subsequently enhanced by incorporating a
259 canopy conductance (G_c) model that couples vegetation transpiration with gross
260 primary productivity, resulting in the development of PML version 2 (PMLv2) as
261 described by Gan et al. (2018). Zhang et al. (2019) applied the PMLv2 model globally.

262 The daily inputs for this model include leaf area index (LAI), ~~white-sky~~
263 ~~shortwavebroadband~~ albedo, and emissivity obtained from the Moderate Resolution
264 Imaging Spectroradiometer (MODIS), as well as temperature variables (~~daily~~
265 ~~maximum temperature-~~ T_{max} , ~~daily minimum temperature-~~ T_{min} , ~~daily mean~~
266 ~~temperature-~~ T_{avg}), instantaneous variables (~~surface pressure-~~ P_{surf} , ~~atmosphere~~
267 ~~pressure-~~ P_a , ~~wind speed at 10-meter height-~~ U , ~~specific humidity-~~ q), and
268 accumulated variables (~~precipitation-~~ P_{rcp} , ~~inward longwave solar radiation-~~ R_{ln} ,
269 ~~inward shortwave solar radiation-~~ R_s) from GLDAS-2.0. Evaporation is divided into
270 direct evaporation from bare soil (E_s), evaporation from solid water sources (water
271 bodies, snow, and ice) (ET_{water}), and vegetation transpiration (E_c). To ensure its
272 accuracy, the PMLv2-ET model was calibrated against 8-daily eddy covariance data
273 from 95 global flux towers representing ten different land cover types.

274 In this study, we employ the latest version, v017. The data is freely available through

275 the google earth engine [https://developers.google.com/earth-
engine/datasets/catalog/CAS_IGSNRR_PML_V2_v017](https://developers.google.com/earth-
276 engine/datasets/catalog/CAS_IGSNRR_PML_V2_v017).

277 **2.6.2.5. FluxCom**

278 FluxCom is a machine-learning-based approach combining global land-atmosphere
279 energy flux data by combining remote sensing and meteorological data (Jung et al.,
280 2019). To achieve this, FluxCom utilizes various machine-learning regression tools,
281 including tree-based methods, regression splines, neural networks, and kernel
282 methods. The outputs of FluxCom are designed based on two complementary
283 strategies: (1) FluxCom-RS, which exclusively merges remote sensing data to
284 generate high spatial resolution flux data; and (2) FluxCom-RS+METEO, which
285 combines meteorological observations with remote sensing data at a daily temporal
286 resolution. The exclusive use of remote sensing data in the ensemble allows
287 producing gridded flux products at a spatial resolution of 500m, albeit with a
288 relatively low frequency of 8 days. It is important to note that the FluxCom-RS data
289 only covers the period after 2000 due to data availability.

290 In contrast, the merging of meteorological and remote sensing data extends the
291 coverage back to 1980 at the cost of a coarser spatial resolution of 0.5°. For more
292 detailed information about the FluxCom dataset, please refer to the FluxCom website
293 (<http://FluxCom.org/>). The data is freely available upon contacting the authors.

294 In this study, we utilized the FluxCom-RS 8-daily 0.0833° energy flux data and
295 converted the latent heat values to evaporation using ERA5-[LandL](#) aggregated daily
296 air temperature. Furthermore, the original [evaporation-ET](#) data were interpolated to a
297 spatial resolution of 0.1° using the MATLAB Gaussian process regression package.

298 **2.7.2.6. Global in-situ observation: FluxNet**

299 The latest FluxNet2015 4.0 eddy-covariance data were used in our study (Pastorello et
300 al., 2020). Following the filtering process by Lin et al. (2018) and Li et al. (2019b),

301 firstly, only the measured and good-quality gap-filled data were used for quality
302 control. Secondly, we excluded days with rainfall and the subsequent day after rainy
303 events to mitigate the impact of canopy interception (Medlyn et al., 2017; Knauer et
304 al., 2018). Additionally, previous studies have indicated an energy imbalance problem
305 in FluxNet2015 data. Therefore, following the method proposed by Twine et al.
306 (2000), the measured ET data were corrected using the residual method based on
307 energy balance.

308 After data filtering and processing, 212 sites are selected as shown in Figure 1. The
309 selected sites are distributed globally, primarily in North America and Europe. The
310 International-Geosphere–Biosphere Program (IGBP) land cover classification system
311 (Loveland et al., 1999) was employed to distinguish the 13 Plant Functional Types
312 (PFTs) across sites. The IGBP classification was determined based on metadata from
313 the FluxNet official website, including evergreen needle leaf forests (ENF, 49 sites),
314 evergreen broadleaf forests (EBF, 15 sites), deciduous broadleaf forests (DBF, 26
315 sites), croplands (CRO, 20 sites), grasslands (GRA, 39 sites), savannas (SAV, ~~nine~~9
316 sites), mixed forests (MF, ~~nine~~9 sites), closed shrublands (CSH, ~~three~~3 sites),
317 deciduous needle leaf forests (DNF, ~~one~~1 site), open shrublands (OSH, 13 sites),
318 snow and ice (SNO, ~~one~~1 site), woody savannas (WSA, 6 sites) and permanent
319 wetland (WET, 21 sites). Changes in the IGBP classification during the study period
320 are possible, but such information is not publicly available. Interested parties can
321 obtain relevant information by directly contacting the site coordinators.

设置了格式: 字体: 加粗

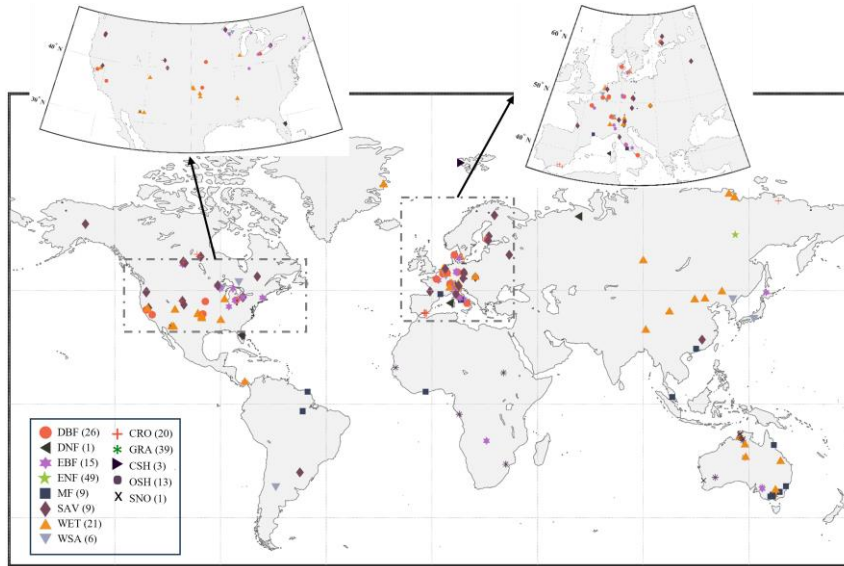


Figure 1 Global distribution of selected FluxNet Sites.

322
323
324

325 4.3. Method

326 In this study, the fusion of products consisted of three steps: (1) the collocation
 327 method (IVD and EIVD) was used to calculate the random error variance of the
 328 selected input products, determine the regionally optimal products, and set an error
 329 threshold; (2) aiming for minimum mean-square-error (MSE), the weights of different
 330 products on each grid were calculated; (3) the products were fused according to the
 331 weights to obtain a long sequence of evapotranspiration products. Since IVD and
 332 EIVD were developed by combining instrumental variable regression and the
 333 extended collocation system, a description of TC and EC algorithms was also
 334 included.

335 4.1.3.1. Triple collocation analysis

336 Since its development in 1998, the implications and formulations of the triple

337 collocation problem have been investigated in many studies. ~~Two notations are~~
 338 ~~proposed, based either on combinations of covariances or cross-multiplied differences~~
 339 ~~between inputs, denoted as difference and covariance notations (Stoffelen, 1998;~~
 340 ~~Dorigo et al., 2010; Su et al., 2014; McColl et al., 2014). These two notations are~~
 341 ~~mathematically identical under the TC-based rescaled scheme (Gruber, 2016). Here,~~
 342 we used difference notation for demonstration.

343 The commonly used error structure for triple collocation analysis (TCA) is:

$$i = \alpha_i + \beta_i \theta + \varepsilon_i \quad (1)$$

344 where $i \in [X, Y, Z]$ are three spatially and temporally collocated data sets; θ is the
 345 unknown true signal for relative geographical variable; α_i and β_i are additive and
 346 multiplicative bias factors against the true signal, respectively; ε_i is the additive zero-
 347 mean random error.

348 The above structure is also a typical instrumental variable (IV) regression. Thus, this
 349 provides another perspective to introduce more variables (>3) (Dong and Crow, 2017;
 350 Su et al., 2014) and polynomial models (Yilmaz and Crow, 2013; De Lannoy et al.,
 351 2007) to the standard TC. We recommend that the readers refer to Su et al. (2014) for
 352 a more detailed discussion on using the IV framework.

353 The basic assumptions adopted in TC are as follows: (i) Linearity between true signal
 354 and data sets, (ii) signal and error stationarity, (iii) independency between random
 355 error and true signal (error orthogonality), (iv) independence between random errors
 356 (zero ~~error cross-correlation, zero-ECC~~). Although many studies have indicated that
 357 some of these assumptions are often violated in practice (Li et al., 2018, 2022; Jia et
 358 al., 2022), the formulation based on these assumptions is still the most robust
 359 implementation (Gruber et al., 2016b). A discussion on these assumptions will be
 360 provided in the discussion section.

361 The data sets first need to be rescaled against an arbitrary reference (e.g., X). The
 362 others are scaled through a TC-based rescaling scheme:

$$Y^X = \beta_Y^X (Y - \bar{Y}) + \bar{X} \quad Z^X = \beta_Z^X (Z - \bar{Z}) + \bar{X} \quad (2)$$

363 The overbar denotes the mean value, and β_Y^X and β_Z^X are the scaling factors as:

$$\left\{ \begin{array}{l} \beta_Y^X = \frac{\beta_X}{\beta_Y} = \frac{\langle (X - \bar{X})(Z - \bar{Z}) \rangle}{\langle (Y - \bar{Y})(Z - \bar{Z}) \rangle} = \frac{\sigma_{XZ}}{\sigma_{YZ}} \\ \beta_Z^X = \frac{\beta_X}{\beta_Z} = \frac{\langle (X - \bar{X})(Y - \bar{Y}) \rangle}{\langle (Z - \bar{Z})(Y - \bar{Y}) \rangle} = \frac{\sigma_{XY}}{\sigma_{ZY}} \end{array} \right. \quad (3)$$

364 where $\langle \cdot \rangle$ is the average operator, σ_{ij} is the covariance of data sets i and j .

365 Subsequently, the error variances could be estimated by averaging the cross-
366 multiplied data set differences as follows:

$$\left\{ \begin{array}{l} \sigma_{\varepsilon_X}^2 = \langle (X - Y^X)(X - Z^X) \rangle \\ \sigma_{\varepsilon_Y}^2 = \beta_Y^{X^2} \sigma_{\varepsilon_Y}^2 = \langle (Y^X - X)(Y^X - Z^X) \rangle \\ \sigma_{\varepsilon_Z}^2 = \beta_Z^{X^2} \sigma_{\varepsilon_Z}^2 = \langle (Z^X - X)(Z^Y - Y^X) \rangle \end{array} \right. \quad (4)$$

367 Expanding the bracket and expressing the rescaling factors yields:

$$\left\{ \begin{array}{l} \sigma_{\varepsilon_X}^2 = \sigma_X^2 - \frac{\sigma_{XY}\sigma_{XZ}}{\sigma_{YZ}} \\ \sigma_{\varepsilon_Y}^2 = \sigma_Y^2 - \frac{\sigma_{YX}\sigma_{YZ}}{\sigma_{XZ}} \\ \sigma_{\varepsilon_Z}^2 = \sigma_Z^2 - \frac{\sigma_{ZX}\sigma_{ZY}}{\sigma_{XY}} \end{array} \right. \quad (5)$$

368 When selecting various scaling references, it is essential to note that the absolute error
369 variances remain consistent. However, this choice can have an impact on the
370 estimation of data sensitivity to the actual signal ($\beta_i^2 \sigma_{\Theta}^2$), which serves as a crucial
371 indicator for comparing spatial error patterns. In order to address the reliance on a
372 specific scaling reference, Draper et al. (2013) introduced the fractional root-mean-
373 squared-error ($fMSE_i$). This measure is obtained by normalizing the unscaled error
374 variance with respect to the true signal variance:

$$fMSE_i = \frac{\sigma_{\varepsilon_i}^2}{\sigma_i^2} = \frac{\sigma_{\varepsilon_i}^2}{\beta_i^2 \sigma_{\Theta}^2 + \sigma_{\varepsilon_i}^2} = \frac{1}{1 + SNR_i} \quad (6)$$

375 where $SNR_i = \frac{\beta_i^2 \sigma_{\Theta}^2}{\sigma_{\varepsilon_i}^2} \in [0,1]$ is the normalized signal-to-noise ratio. $SNR = 0$
376 indicates a noise-free observation, while $SNR = 1$ corresponds that the variances of
377 estimates equal that of the true signal.

378 Following similar ideas, Mccoll et al. (2014) extended the framework to estimate the
 379 data-truth correlation, known as ~~extended triple collocation~~ (ETC):

$$R_i^2 = \frac{\beta_i^2 \sigma_\theta^2}{\beta_i^2 \sigma_\theta^2 + \sigma_{\varepsilon_i}^2} = \frac{SNR_i}{1 + SNR_i} = \frac{1}{1 + NSR_i} \quad (7)$$

$$R_i^2 = 1 - fMSE_i$$

380 In comparison to the conventional coefficient of determination R_{ij} , which is
 381 influenced by data noise and sensitivity. It is important to note that R_i^2 is merely based
 382 on the data set i , whereas R_{ij} is influenced by both data set i and reference j . In other
 383 words, R_i^2 incorporates the dependency on the chosen reference. Thus, TC-derived
 384 $fMSE_i$ and R_i^2 serve as superior indicators for assessing the actual quality of data, as
 385 discussed by Kim et al. (2021b) and Gruber et al. (2020).

386 4.2.3.2. Double instrumental variable technique

387 The assumed error structure in TC is also a typical instrumental variable (IV)
 388 regression. In practical usage, finding three completely independent sets of products is
 389 usually tricky. Su et al. (2014) effectively improve the applicability of the TC method
 390 by using the lag-1 time series (e.g., $X_{t-1} = \alpha_X + \beta_X \theta_{t-1} + \varepsilon_{X,t-1}$) from one of the
 391 two sets of data as the third input for TC. In this way, we only need two independent
 392 products for input.

393 Such process includes another assumption that all data sets contain serially white
 394 errors (i.e., $\langle \varepsilon_{i,t} \varepsilon_{i,t-1} \rangle = 0$, zero auto-correlation). Building upon this, Dong et al.
 395 (2019) utilizes the lag-1 time series from both data sets as inputs and propose ~~a~~ the
 396 more stable ~~double instrumental variable (IVD)~~ method.

397 For a double input $[X, Y$ with $\sigma_{\varepsilon_X \varepsilon_Y} = 0]$, the linear error model and related lag-1
 398 time series can be expressed as:

$$\begin{cases} X = \alpha_X + \beta_X \theta + \varepsilon_X & I = \alpha_X + \beta_X \theta_{t-1} + \varepsilon_{X,t-1} \\ Y = \alpha_Y + \beta_Y \theta + \varepsilon_Y & J = \alpha_Y + \beta_Y \theta_{t-1} + \varepsilon_{Y,t-1} \end{cases} \quad (8)$$

399 where I and J are the lag-1 time series of X and Y , respectively.

400 Assuming product errors are mutually independent and orthogonal to the truth, the
 401 covariance between the products is expressed as:

$$\begin{cases} \sigma_X^2 = \beta_X^2 \sigma_\theta^2 + \sigma_{\varepsilon_X}^2 & \sigma_Y^2 = \beta_Y^2 \sigma_\theta^2 + \sigma_{\varepsilon_Y}^2 \\ \sigma_{XY} = \beta_X \beta_Y \sigma_\theta^2 \\ \sigma_{IX} = \beta_X^2 L_{\theta\theta} & \sigma_{JY} = \beta_Y^2 L_{\theta\theta} \end{cases} \quad (9)$$

402 where $L_{ii} = \langle i_t i_{t-1} \rangle$ is the auto-covariance. Therefore, the IVD-estimated dynamic
 403 range ratio scaling factors yields:

$$s_{ivd} \equiv \frac{\beta_X}{\beta_Y} = \sqrt{\frac{\sigma_{IX}}{\sigma_{JY}}} \quad (10)$$

404 Hence, the random error variances of X and Y can be solved as:

$$\begin{cases} \sigma_{\varepsilon_X}^2 = \sigma_X^2 - \sigma_{XY} * s_{ivd} \\ \sigma_{\varepsilon_Y}^2 = \sigma_Y^2 - \frac{\sigma_{XY}}{s_{ivd}} \end{cases} \quad (11)$$

405 **4.3.3.3. Extended double instrumental variable technique**

406 Furthermore, by adopting the designed matrix in ~~extended collocation (the EC~~
 407 ~~method)~~ (Gruber et al., 2016a), Dong et al. (2020a) present the ~~extended double~~
 408 ~~instrumental variable technique (denoted as EIVD)~~ method to estimate the error
 409 variance matrix with only two independent data sets.

410 For a triplet input $[i, j, k$ with $\sigma_{\varepsilon_i \varepsilon_j} \neq 0]$. The dynamic range ratio scaling factors can
 411 be estimated as follows:

$$s_{ij} \equiv \frac{\beta_i}{\beta_j} = \sqrt{\frac{L_{ii}}{L_{jj}}} \quad (12)$$

412 where $L_{ii} = \langle i_t i_{t-1} \rangle$ is the auto-covariance of inputs. Subsequently, the sensitivity
 413 and absolute error variance of the data set follow:

$$\beta_j^2 \sigma_\theta^2 = \sigma_{ij} \sqrt{\frac{L_{ii}}{L_{jj}}} \quad \sigma_{\varepsilon_j}^2 = \sigma_{ij} \sqrt{\frac{L_{ii}}{L_{jj}}} - \sigma_i^2 \quad (13)$$

414 The cross-multiplied factors can be estimated by:

$$\beta_i \beta_j \sigma_{\theta}^2 = \sigma_{ik} \sqrt{\frac{L_{jj}}{L_{kk}}} = \sigma_{jk} \sqrt{\frac{L_{ii}}{L_{kk}}} \quad \sigma_{\varepsilon_i \varepsilon_j} = \sigma_{ij} - \beta_i \beta_j \sigma_{\theta}^2 \quad (14)$$

415 Hence, for a triplet with the input of $[X, Y, Z]$ with $\sigma_{\varepsilon_X \varepsilon_Y} \neq 0$: the matrix notation of
 416 the above system with $\mathbf{y} = \mathbf{Ax}$ is given as:

$$\mathbf{y} = \begin{pmatrix} \sigma_X^2 \\ \sigma_Y^2 \\ \sigma_Z^2 \\ \sigma_{XY} \\ \sigma_{XZ} \sqrt{\frac{L_{XX}}{L_{ZZ}}} \\ \sigma_{YZ} \sqrt{\frac{L_{YY}}{L_{ZZ}}} \\ \sigma_{ZX} \sqrt{\frac{L_{ZZ}}{L_{XX}}} \\ \sigma_{ZY} \sqrt{\frac{L_{ZZ}}{L_{YY}}} \\ \sigma_{XZ} \sqrt{\frac{L_{YY}}{L_{ZZ}}} \\ \sigma_{YZ} \sqrt{\frac{L_{XX}}{L_{ZZ}}} \end{pmatrix}_{10 \times 1} \mathbf{A} = \begin{pmatrix} \mathbf{I}_{4 \times 4} & \mathbf{0}_{6 \times 4} \\ \mathbf{0}_{6 \times 4} & \mathbf{I}_{4 \times 4} \end{pmatrix}_{10 \times 8} \mathbf{x} = \begin{pmatrix} \beta_X^2 \sigma_{\theta}^2 \\ \beta_Y^2 \sigma_{\theta}^2 \\ \beta_Z^2 \sigma_{\theta}^2 \\ \beta_X \beta_Y \sigma_{\theta}^2 \\ \sigma_{\varepsilon_X}^2 \\ \sigma_{\varepsilon_Y}^2 \\ \sigma_{\varepsilon_Z}^2 \\ \sigma_{\varepsilon_X \varepsilon_Y} \end{pmatrix}_{8 \times 1} \quad (15)$$

417 Likewise, the least-squared solution for unknown \mathbf{x} is then solved by:

$$\mathbf{x} = (\mathbf{A}^T \mathbf{A})^{-1} \mathbf{A}^T \mathbf{y} \quad (16)$$

418 4.4.3.4. Weight Estimation

419 Our objective is to predict an uncertain variable, such as evapotranspiration (ET) over
 420 time at a specific location, by utilizing parent products that may contain random errors.
 421 The underlying concept of weighted averaging is to extract independent information
 422 from multiple data sources to enhance prediction accuracy by mitigating the effects of
 423 random errors. The effectiveness of this approach relies on the independence of the
 424 individual data sources under consideration. Weighted averaging has found
 425 applications in various fields following the influential work of Bates and Granger
 426 (1969), who proposed the optimal combination of forecasts based on a **mean-square**

427 ~~error (minimum MSE)~~ criterion. In this context, the term "optimal" refers to
 428 minimizing the variance of residual random errors in the least squares sense.
 429 Mathematically, this weighted average can be expressed as follows:

$$\bar{x} = \bar{\mathbf{W}}^T \bar{\mathbf{X}} = \sum_{i=1}^N \omega_i x_i \quad (17)$$

430 where \bar{x} is the merged estimate; $\bar{\mathbf{X}} = [x_1, \dots, x_n]^T$ contains the temporally collocated
 431 estimates from N different parent products, which are merged with relative zero-mean
 432 random error $\bar{\mathbf{e}} = [\varepsilon_1, \dots, \varepsilon_n]^T$; and $\bar{\mathbf{W}} = [\omega_1, \dots, \omega_n]^T$ contains the weights assigned
 433 to these estimates, where $\omega_i \in [0,1]$ and $\sum \omega_i = 1$ ensuring an unbiased prediction.

434 The averaging weights can be expressed as the solution to the problem:

$$\min f(\bar{\mathbf{W}}) = \mathbb{E}(\bar{\mathbf{e}}^T \bar{\mathbf{W}})^2 \quad (18)$$

435 where $\mathbb{E}()$ is the operator for mathematical expectation, the solution of this problem is
 436 determined by the individual random error characteristics of the input data sets and
 437 can be derived from their covariance matrix (Bates and Granger, 1969; Gruber et al.,
 438 2017; Kim et al., 2021b):

$$\begin{aligned} \bar{\mathbf{W}} &= (\bar{\mathbf{I}}^T \mathbb{E}(\bar{\mathbf{e}} \bar{\mathbf{e}}^T)^{-1} \bar{\mathbf{I}})^{-1} \mathbb{E}(\bar{\mathbf{e}} \bar{\mathbf{e}}^T)^{-1} \bar{\mathbf{I}} \\ \sigma_{\bar{x}}^2 &= (\bar{\mathbf{I}}^T \mathbb{E}(\bar{\mathbf{e}} \bar{\mathbf{e}}^T)^{-1} \bar{\mathbf{I}})^{-1} \end{aligned} \quad (19)$$

439 where $\mathbb{E}(\bar{\mathbf{e}} \bar{\mathbf{e}}^T)$ is the $N \times N$ error covariance matrix that holds the random error
 440 variance $\sigma_{\varepsilon_i}^2$ of the parent products in the diagonals and relative error covariances $\sigma_{\varepsilon_i \varepsilon_j}$
 441 in the off-diagonals; $\bar{\mathbf{I}} = [1, \dots, 1]^T$ is an ones-vector of length N ; and $\sigma_{\bar{x}}^2$ is the
 442 resulting random error variances of the merged estimate.

443 When only two groups of products are used as input ($N = 2$), it is generally assumed
 444 that the errors between them are independent. In this case, the weights are as follows:

$$\begin{aligned} \mathbb{E}(\bar{\mathbf{e}} \bar{\mathbf{e}}^T) &= \begin{bmatrix} \sigma_{\varepsilon_1}^2 & 0 \\ 0 & \sigma_{\varepsilon_2}^2 \end{bmatrix} \\ \omega_1 &= \frac{\sigma_{\varepsilon_2}^2}{\sigma_{\varepsilon_1}^2 + \sigma_{\varepsilon_2}^2} \quad \omega_2 = \frac{\sigma_{\varepsilon_1}^2}{\sigma_{\varepsilon_1}^2 + \sigma_{\varepsilon_2}^2} \end{aligned} \quad (20)$$

445 In most cases, we can identify three sets of products as inputs ($N = 3$). In this
 446 scenario, we consider the possibility of error homogeneity, assuming a non-zero ECC
 447 exists between inputs 1 and 2. In this case, the error matrix can be represented as:

$$\mathbb{E}(\overline{\mathbf{e}\mathbf{e}^T}) = \begin{bmatrix} \sigma_{\varepsilon_1}^2 & \sigma_{\varepsilon_1\varepsilon_2} & 0 \\ \sigma_{\varepsilon_1\varepsilon_2} & \sigma_{\varepsilon_2}^2 & 0 \\ 0 & 0 & \sigma_{\varepsilon_3}^2 \end{bmatrix} \quad (21)$$

448 The weights can then be written as:

$$\vec{\mathbf{W}} = \begin{cases} \frac{\sigma_{\varepsilon_2}^2 - \sigma_{\varepsilon_1\varepsilon_2}}{(\sigma_{\varepsilon_1}^2\sigma_{\varepsilon_2}^2 - \sigma_{\varepsilon_1\varepsilon_2}^2) * \mathbb{Z}} \\ \frac{\sigma_{\varepsilon_1}^2 - \sigma_{\varepsilon_1\varepsilon_2}}{(\sigma_{\varepsilon_1}^2\sigma_{\varepsilon_2}^2 - \sigma_{\varepsilon_1\varepsilon_2}^2) * \mathbb{Z}} \\ \frac{1}{\sigma_{\varepsilon_3}^2 * \mathbb{Z}} \end{cases} \quad (22)$$

$$\mathbb{Z} = \frac{\sigma_{\varepsilon_1}^2 + \sigma_{\varepsilon_2}^2 - 2\sigma_{\varepsilon_1\varepsilon_2}}{\sigma_{\varepsilon_1}^2\sigma_{\varepsilon_2}^2 - \sigma_{\varepsilon_1\varepsilon_2}^2} + \frac{1}{\sigma_{\varepsilon_3}^2}$$

449 It is essential to acknowledge that before applying these weights for merging the data
 450 sets, it is necessary to address any existing systematic differences. Typically, this is
 451 achieved by rescaling the data sets to a standardized data space. Consequently, the
 452 weights can be derived from the rescaled data sets using Eq (2)-(3) and converge
 453 accordingly. This procedure ensures the accuracy and reliability of the merged data
 454 sets for further analysis.

455 If ECC is not considered (i.e., setting $\sigma_{\varepsilon_1\varepsilon_2} = 0$), Eq (22) represents the weight
 456 calculation method commonly used in most TC fusion studies. ~~This method was
 457 initially applied by Yilmaz et al. (2012) in the fusion of multi-source soil moisture
 458 products and later improved by Gruber et al. (2017) and further applied in the
 459 production of the ESA CCI global soil moisture product (Gruber et al., 2019). Dong et
 460 al. (2020b) also adopted this approach to fusing multi-source precipitation products.
 461 In the study of evapotranspiration, Li et al. (2023e)(2023b) and Park et al.(2023)
 462 utilized a weight calculation method that does not consider non-zero ECC and fused
 463 multiple ET products in the Nordic and East Asia, respectively, achieving satisfactory~~

域代码已更改

464 ~~fusion results.~~

465 In contrast to the fusion studies mentioned above for evapotranspiration products, for
466 the first time, the consideration of non-zero ECC is incorporated into the fusion
467 process and integrated into the weight calculation. Yilmaz and Crow (2014) have
468 demonstrated that TC underestimates error variances when the zero ECC assumption
469 is violated. Li et al. (2022), in their evaluation study of global ET products using the
470 collocation method, also indicated the existence of error homogeneity issues between
471 commonly used ET products (such as ERA5L and GLEAM), necessitating the
472 consideration of the influence of non-zero ECC. The merging technique employed in
473 this study provides a more explicit characterization of product errors and facilitates
474 the derivation of more reliable weight coefficients, thereby achieving [superior](#)
475 [promising](#) fusion outcomes.

476 The differences in results are evaluated at the site scale by contrasting the scenarios
477 without considering non-zero ECC and directly using simple averages to compare and
478 validate the advantages of the weight calculation method used in our study.

479 4.5.3.5. Merging combination

480 In this study, we employ five commonly used global land surface ~~evapotranspiration~~
481 ~~(ET)~~ET products as described in the datasets section. PMLv2 and FluxCom-[RS](#) have
482 an original resolution of 0.083° and an 8-day average. In this research, they are
483 interpolated to 0.1° resolution, and the values for each data period of 8 days are kept
484 consistent. For example, the values for March 5 to March 12, 2000, are the same. ~~ET~~
485 ~~values often exhibit variability over an 8-day period, making the use of an 8-day~~
486 ~~average to represent temporal dynamics potentially introducing further uncertainties.~~

487 This operation is performed to ensure adequate data for the collocation analysis (Kim
488 et al., 2021a). ~~We openly acknowledge the possible sources of error and express our~~
489 ~~commitment to addressing and improving them in future work, and any potential~~
490 ~~errors resulting from it will be discussed in the discussion section.~~

491 As mentioned in the methodology section, it is vital to consider the issue of random
492 error homogeneity among different products before applying the collocation method.
493 Although EC or EIVD methods can be used to calculate the ECC between specific
494 pairs of products, it is necessary to determine which pairs of products have non-zero
495 ECC conditions. In previous research, Li et al.(2022) employed five collocation
496 methods (IVS/IVD/TC/EIVD/EC) to analyze the performance of five sets of ET
497 products (ERA5L/~~GLEAMv3~~/PMLv2/FluxCom/~~GLDAS2~~/~~GLEAMv3~~/PMLv2) at the
498 global scale, and applied EC and EIVD methods to calculate the ECC between
499 different products. The results indicated a relatively significant error homogeneity
500 between PMLv2 and FluxCom at a resolution of 0.1° (with a global average ECC of
501 approximately 0.3). The error homogeneity could be attributed to both products
502 utilizing GLDAS meteorological data as input, despite their different methods for ET
503 estimation. At a resolution of 0.25°, ERA5L and GLEAM exhibited a more apparent
504 error correlation (with a global average ECC of approximately 0.4). Considering the
505 long temporal data of GLEAMv3 version a, ECMWF meteorological data was chosen
506 as the driving force, making the error correlation between the two products
507 predictable.

508 Therefore, this study assumes that non-zero ECC situations occur between PMLv2-
509 FluxCom and ERA5L-GLEAM. We also calculated the possible ECC situations
510 among other products, presented in the discussion section and the appendix. Based on
511 the analysis, our assumed non-zero ECC situations align reasonably well with the
512 actual circumstances.

513 In addition, previous research suggests that the IVD method outperforms the IVS
514 method in scenarios involving two sets of inputs, while the EIVD method is
515 considered more reliable than the TC method in situations with three sets of inputs (Li
516 et al., 2022; Kim et al., 2021a). Therefore, in this study, the IVD and EIVD methods
517 are selected for computation based on different combinations of inputs. ~~Table 2~~
518 ~~Table 2~~ presents the data and methods used during corresponding periods. When

519 only two sets of products are available, we employ the IVD method for fusion and
 520 calculate weights using Eq. (20). When three sets of products are available, we utilize
 521 the EIVD method for fusion and calculate weights using Eq. (22).

522 **Table 2.** Combination of inputs and accessible methods

Scenario 1 (0.1°)		
Period	Selected Inputs	Method
(2000.02.26-2000.12.31)	ERA5L/ PMLv2	IVD
(2001.01.01-2015.12.27)	ERA5L/ FluxCom/ PMLv2	EIVD
(2015.12.28-2020.12.26)	ERA5L/ PMLv2	IVD
Scenario 2 (0.25°)		
Period	Selected Inputs	Method
(1980.01.01-1999.12.31)	ERA5L/ GLDAS20/ GLEAMv3.7a	EIVD
(2000.01.01-2022.12.31)	ERA5L/ GLDAS21/ GLEAMv3.7a	

设置了格式: 字体: (中文) 黑体

523 It should be noted that the same product can have different versions. In this study,
 524 appropriate versions are selected based on the following principles: (1) Selection
 525 based on the corresponding data coverage duration and ensuring more products to
 526 gain more information; (2) Choosing the latest version while considering the
 527 assumption of non-zero ECC conditions; (3) Making efforts to select the exact
 528 product versions for different periods, to avoid uncertainties caused by version
 529 changes. We selected a subset of sites to compare the fusion results using different
 530 versions, and the corresponding details will be presented in the discussion section.

531 4.6.3.6. Evaluation indices

532 Five statistical indicators, namely Root-mean-squared-error (*RMSE*), Pearson's
 533 correlation coefficient (*R*), Mean-absolute-error (*MAE*), unbiased *RMSE* (*ubRMSE*)
 534 and Kling-Gupta Efficiency (*KGE*), are selected for comparison with existing
 535 products. The relative equations are shown as follows:

$$RMSE = \sqrt{\frac{\sum_{i=1}^n (sim_i - obs_i)^2}{n}} \quad (23)$$

$$R = \frac{\sum_{i=1}^n (sim_i - \overline{sim})(obs_i - \overline{obs})}{\sqrt{\sum_{i=1}^n (sim_i - \overline{sim})^2 \sum_{i=1}^n (obs_i - \overline{obs})^2}} \quad (24)$$

$$-1 \leq R \leq 1$$

$$MAE = \frac{1}{n} \sum_{i=1}^n |sim_i - obs_i| \quad (25)$$

$$ubRMSE = \sqrt{\frac{\sum_{i=1}^n [(sim_i - \overline{sim}) - (obs_i - \overline{obs})]^2}{n}} \quad (26)$$

536 Where *sim* is the simulations, *obs* is the observation as reference.

537 The modified KGE (Kling et al., 2012) ~~(Gupta et al., 2009)~~ offers insights into
 538 reproducing temporal dynamics and preserving the distribution of time series, which
 539 are increasingly used to calibrate and evaluate hydrological models (Knoben et al.,
 540 2019). For a better understanding of the KGE statistic and its advantages over the
 541 addressed several shortcomings in Nash-Sutcliffe Efficiency (NSE), please refer to
 542 Gupta et al. (2009). The equation is given by and are increasingly used for calibration
 543 and evaluation (Knoben et al., 2019), given by:

$$KGE = \frac{1}{\sqrt{(r-1)^2 + \left(\frac{\sigma_{sim}}{\sigma_{obs}} - 1\right)^2 + \left(\frac{\sigma_{sim}/\mu_{sim}}{\sigma_{obs}/\mu_{obs}} - 1\right)^2}} \quad (27)$$

544 Where σ_{obs} and σ_{sim} are the standard deviations of observations and simulations;
 545 μ_{obs} and μ_{sim} are the mean of observations and simulations. Similar to *NSE*, *KGE* = 1
 546 indicates perfect agreement of simulations, while *KGE* < 0 reveals that the average of
 547 observations is better than simulations (Towner et al., 2019).

548 5.4. Results

549 In this study, we aimed to compare and evaluate the performance of fused products at
 550 both site and global scales. ~~Specifically, Lu et al. (2021)'s global 0.25° daily scale ET~~
 551 ~~product derived using Reliability Ensemble Averaging (denoted as REA) was also~~
 552 ~~selected for comparative analysis.~~ At the site scale, the performance of the fused

设置了格式: 字体: 11 磅

设置了格式: 字体: 11 磅

设置了格式: 字体: 11 磅

设置了格式: 字体: 11 磅

设置了格式: 字体: 11 磅

设置了格式: 字体: 11 磅

设置了格式: 字体: 11 磅

设置了格式: 字体: 11 磅

设置了格式: 字体: 11 磅

设置了格式: 字体: 11 磅

设置了格式: 字体: 11 磅

设置了格式: 字体: 11 磅

设置了格式: 字体: 11 磅

设置了格式: 字体: 11 磅

设置了格式: 字体: 11 磅

设置了格式: 字体: 11 磅

设置了格式: 字体: 11 磅

设置了格式: 字体: 11 磅

设置了格式: 字体: 11 磅

设置了格式: 字体: 11 磅

设置了格式: 字体: 11 磅

设置了格式: 字体: 11 磅

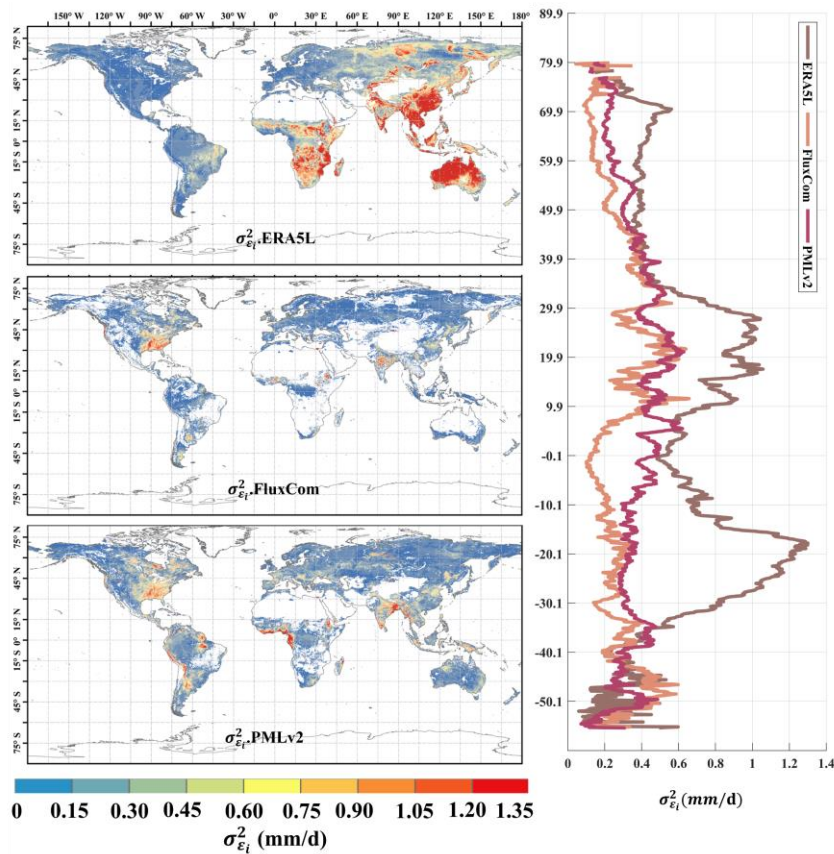
设置了格式: 字体: 11 磅

设置了格式: 字体: 11 磅

553 products was evaluated against 212 FluxNet observations and compared with other
 554 products, including the simple average. At the global scale, the mean and temporal
 555 variations of the land surface ET calculated by the fused products were compared
 556 with those of other products.

557 **5.1.4.1. Analysis of error variances and weights**

558 This section analyzed the random error variances and assigned weights of the 0.1° and
 559 0.25° inputs obtained using the EIVD method. This section examines the random error
 560 variances and identifies the predominant product based on assigned weights for the
 561 0.1° and 0.25° inputs obtained through the EIVD method.

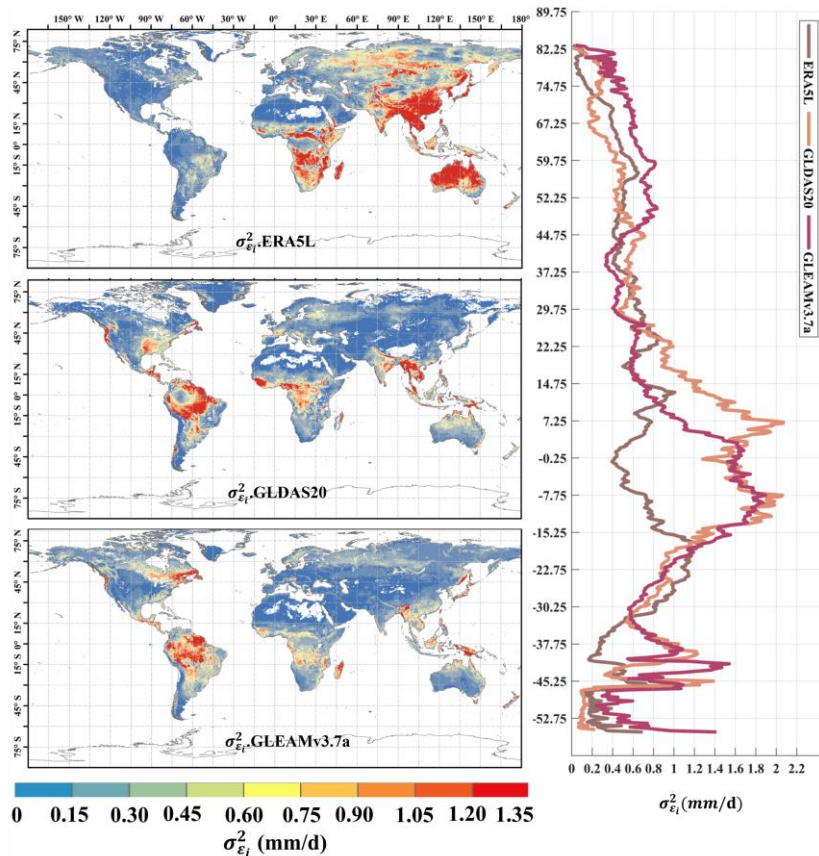


562 **Figure 21** Global distribution of absolute error variances ($\sigma_{\epsilon_i}^2$) of ERA5L, FluxCom,
 563

564 and PMLv2 using EIVD at 0.1° from 2001 to 2015, depicted alongside corresponding
565 variation curves of average $\sigma_{\varepsilon_i}^2$ with latitude.

566 ~~Figure 2~~~~Figure 1~~~~Figure 1~~~~Figure 1~~ represents the random errors of the correlation
567 products calculated using the EIVD method from 2001 to 2015 at 0.1°, where a non-
568 zero ECC is assumed between FluxCom and PMLv2. The areas with missing values
569 are due to the absence of data from either FluxCom or PMLv2 in those regions. The
570 global random error variances (mean \pm standard deviation) obtained using the EIVD
571 method are as follows: ERA5L: 0.58 ± 0.53 mm/day, FluxCom: 0.12 ± 0.13 mm/day,
572 PMLv2: 0.17 ± 0.14 mm/day. These results indicate that FluxCom performs best
573 overall, while ERA5L performs the poorest. Regarding spatial distribution, regions
574 with more significant random errors in ERA5L are mainly located in East Asia,
575 Australia, and southern Africa. On the other hand, FluxCom and PMLv2 show
576 relatively more considerable uncertainties in the southeastern United States. The
577 latitude distribution reveals that ERA5L has the highest uncertainty, primarily in the
578 vicinity of 20° to 30° north and south, consistent with its spatial distribution.

579 It is important to note that due to missing data in specific regions at 0.1°, such as
580 Northern Africa, the Sahara Desert region, Northwestern China, and Australia, the
581 error results obtained may not accurately reflect the performance of FluxCom and
582 PMLv2 in these areas. Considering the current results, we can cautiously conclude
583 that FluxCom and PMLv2 demonstrate better performance. Future data
584 supplementation in these regions would further enhance our ability to analyze the
585 products' accuracy.



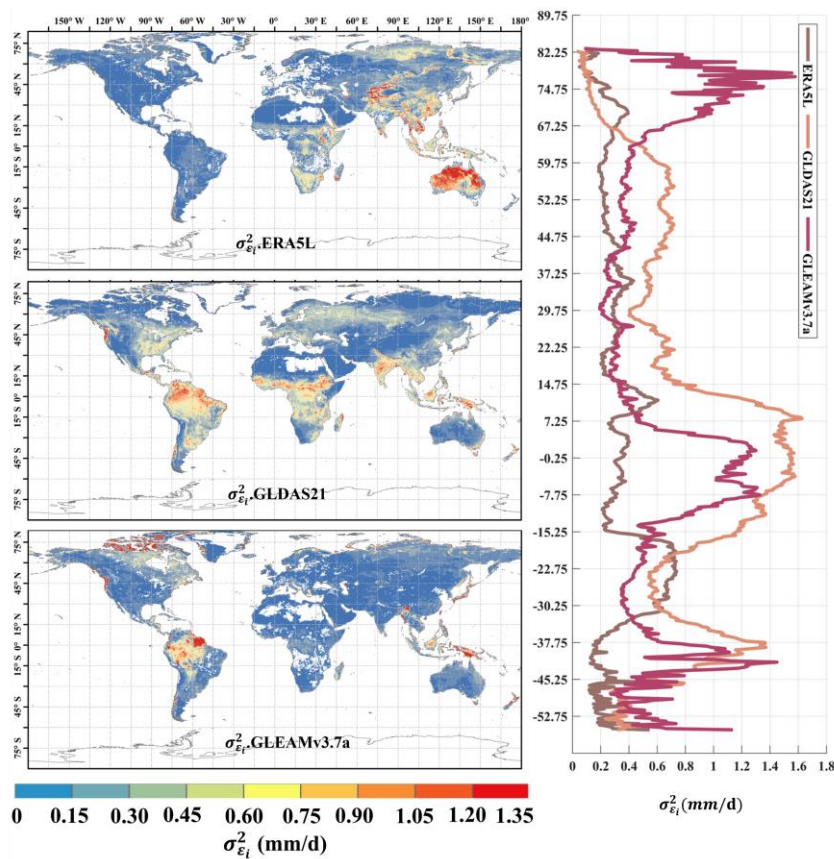
586

587 **Figure 32** Global distribution of absolute error variances ($\sigma_{\epsilon_i}^2$) of ERA5L, GLDAS2.0,
 588 and GLEAMv3.7a using EIVD at 0.25° from 1980 to 1999, depicted alongside
 589 corresponding variation curves of average with latitude.

590 The distribution of random error variance for ERA5L (0.59 ± 0.58 mm/d), GLDAS2.0
 591 (0.37 ± 0.44 mm/d), and GLEAMv3.7a (0.38 ± 0.36 mm/d) from 1980 to 1999 at 0.25°
 592 is shown in **Figure 3**~~Figure-2~~**Figure-2**. Here, we assumed a non-zero ECC between
 593 ERA5L and GLEAM. The ERA5L data was resampled from a 0.1° resolution to 0.25° ,
 594 and its error distribution pattern is like that of the 0.1° resolution. It exhibits higher
 595 uncertainties in East Asia, Australia, and southern Africa. GLDAS and GLEAM
 596 exhibit relatively higher uncertainty over the southeastern United States and the
 597 Amazon Plain. GLDAS and GLEAM show similar performance among the three

598 products, while ERA5L performs relatively worse. Regarding the average distribution
 599 with latitude, ERA5L demonstrates a more even distribution, whereas GLDAS and
 600 GLEAM exhibit relatively higher uncertainties in tropical regions.

601 [The ET calculations in both GLDAS and GLEAM involve complex surface](#)
 602 [parameterization processes. In tropical regions, the high non-heterogeneity in land](#)
 603 [covers poses a challenge, and the 0.25° resolution grid may not capture the intricacies](#)
 604 [of the underlying surface conditions. This mismatch could impact the](#)
 605 [parameterization process, leading to errors. Future work could involve in-depth model](#)
 606 [analyses or sensitivity experiments to identify sources of error in complex ET models,](#)
 607 [facilitating improvements.](#)



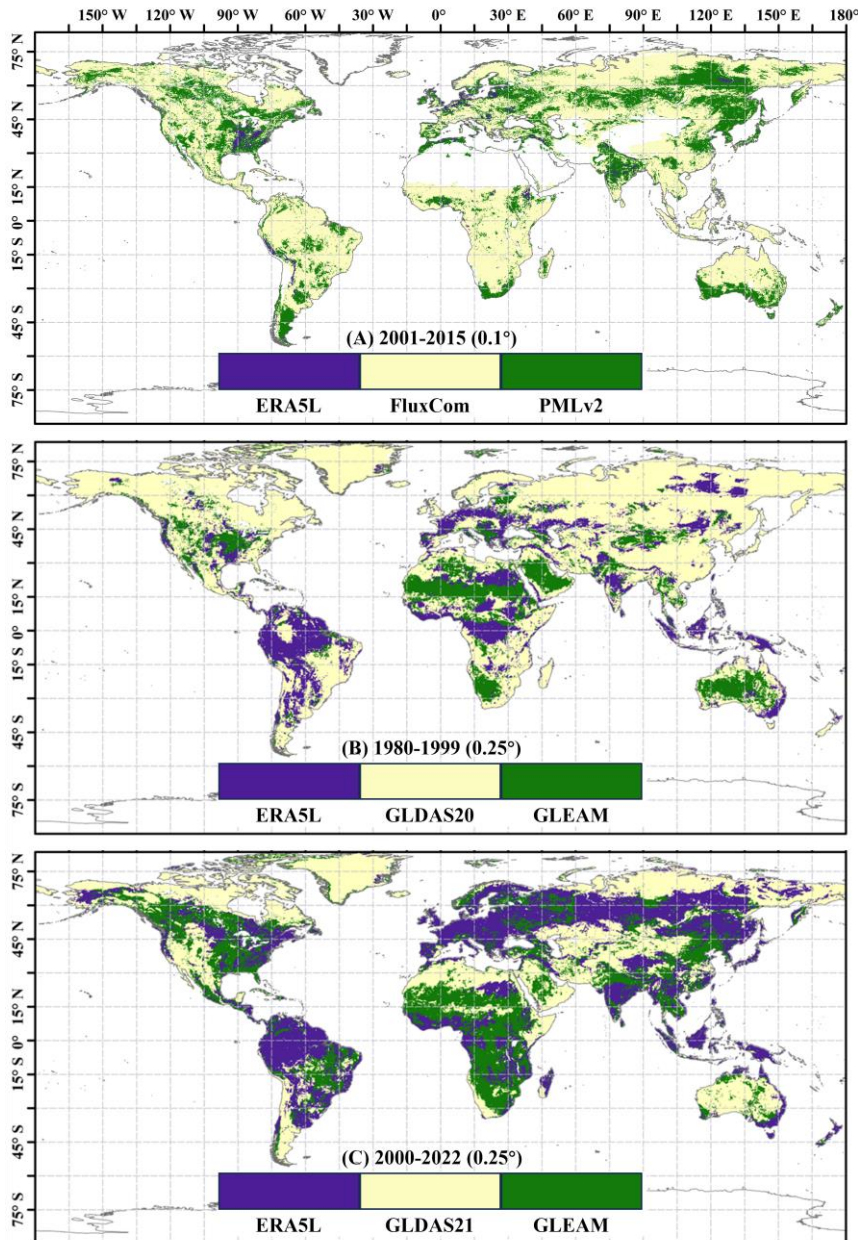
608
 609 **Figure 43** Global distribution of absolute error variances ($\sigma_{\epsilon_i}^2$) of ERA5L, GLDAS2.1,

610 and GLEAMv3.7a using EIVD at 0.25° from 2000 to 2022, depicted alongside
611 corresponding variation curves of average with latitude.

612 In addition, ~~Figure 4~~~~Figure 3~~~~Figure 3~~ presents the distribution of random error
613 variance for ERA5L (0.32 ± 0.33 mm/d), GLDAS2.1 (0.35 ± 0.29 mm/d), and
614 GLEAMv3.7a (0.38 ± 0.36 mm/d) from 2000 to 2022 at a resolution of 0.25°. The
615 non-zero ECC assumption was made between ERA5L and GLEAM. In this
616 combination, ERA5L shows significantly lower errors than in previous periods,
617 indicating improved ERA5L performance during this time frame. However, ERA5L
618 still exhibits more significant errors in the East Asia and Australia regions compared
619 to the other two datasets. The overall errors for GLDAS and GLEAM have also
620 decreased, but there are still random error variances exceeding 1.0 mm/d in the
621 Amazon plain and Indonesia region. Regarding the latitudinal distribution, ERA5L
622 shows relatively smooth changes, while GLDAS and GLEAM exhibit similar trends.
623 However, GLEAM demonstrates a noticeable increase in errors near the Arctic.

624 Next, in ~~Figure 5~~~~Figure 4~~~~Figure 4~~, we present the dominant product for each grid
625 cell in the three scenarios, where dominance refers to the product with the highest
626 assigned weight. The results in ~~Figure 5~~~~Figure 4~~~~Figure 4~~ indicate that at 0.1°
627 resolution, the weights for FluxCom and PMLv2 are significantly higher than ERA5L,
628 aligning with the error calculations presented in ~~Figure 2~~~~Figure 1~~~~Figure 1~~. This
629 underscores the effectiveness of error and weight analysis based on collocation in
630 reflecting product performance, thereby allowing for a rational adaptation of weights.
631 At 0.25° resolution, the dominant regions for ERA5L, GLDAS-2, and GLEAM
632 products are relatively balanced. In the fusion scenario from 1980 to 1999, GLDAS20
633 predominantly covers the Northern Hemisphere, while GLEAM dominates the
634 Southern Hemisphere, with ERA5L prevalent in the Amazon region. However, in the
635 fusion scenario from 2000 to 2022, GLEAM's dominant region significantly expanded,
636 primarily covering the central United States and southeastern China. The Amazon
637 region continues to be dominated by ERA5L. The variation in dominant products

638 highlights that the calculation of product weights evolves with changes in the fusion
639 scenario. The error and weight computation methods based on collocation can only
640 provide the minimum MSE solution for a given combination of inputs. It is important
641 to note that changes in inputs will impact the results.~~Dominant~~ 部分



642
 643 **Figure 543** Map of the prevailing product at individual pixels based on scenario-
 644 specific weights.

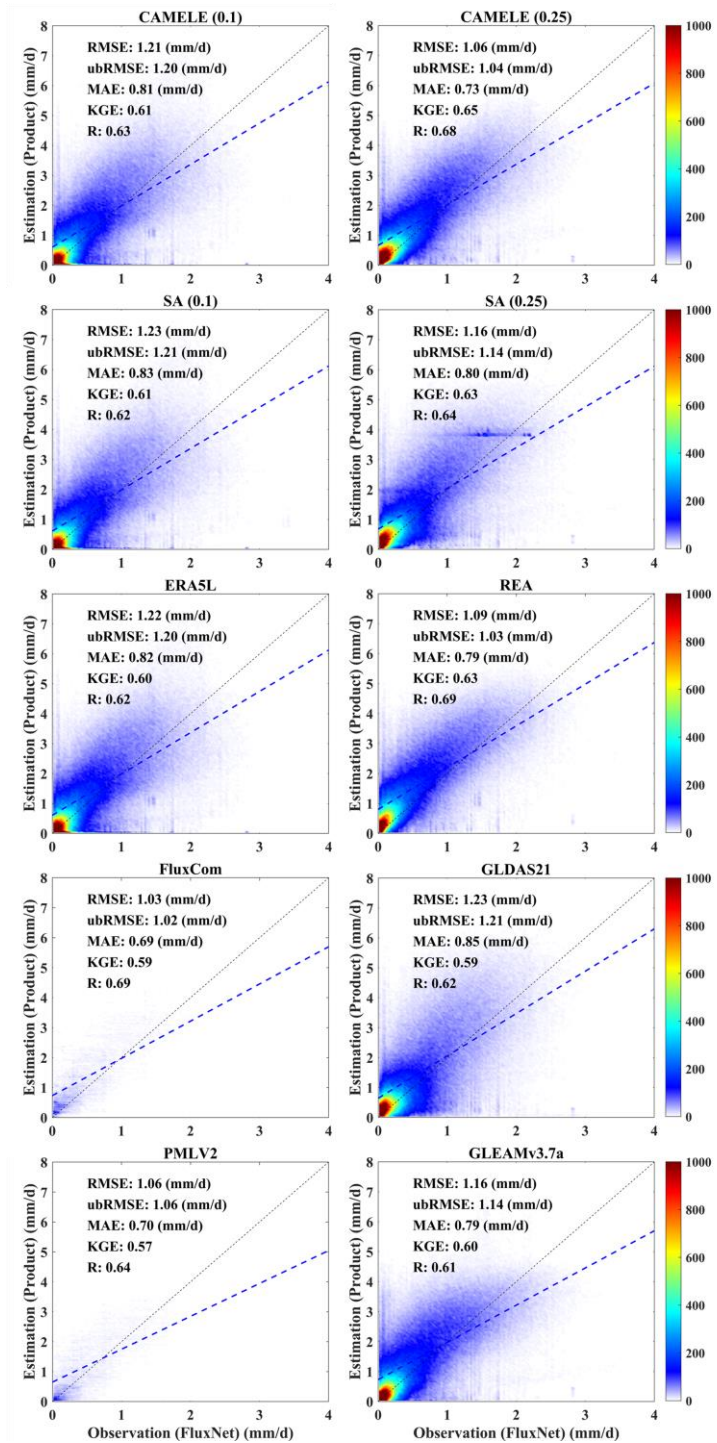
645 For the analysis at a resolution of 0.1°, we also applied the IVD method to calculate

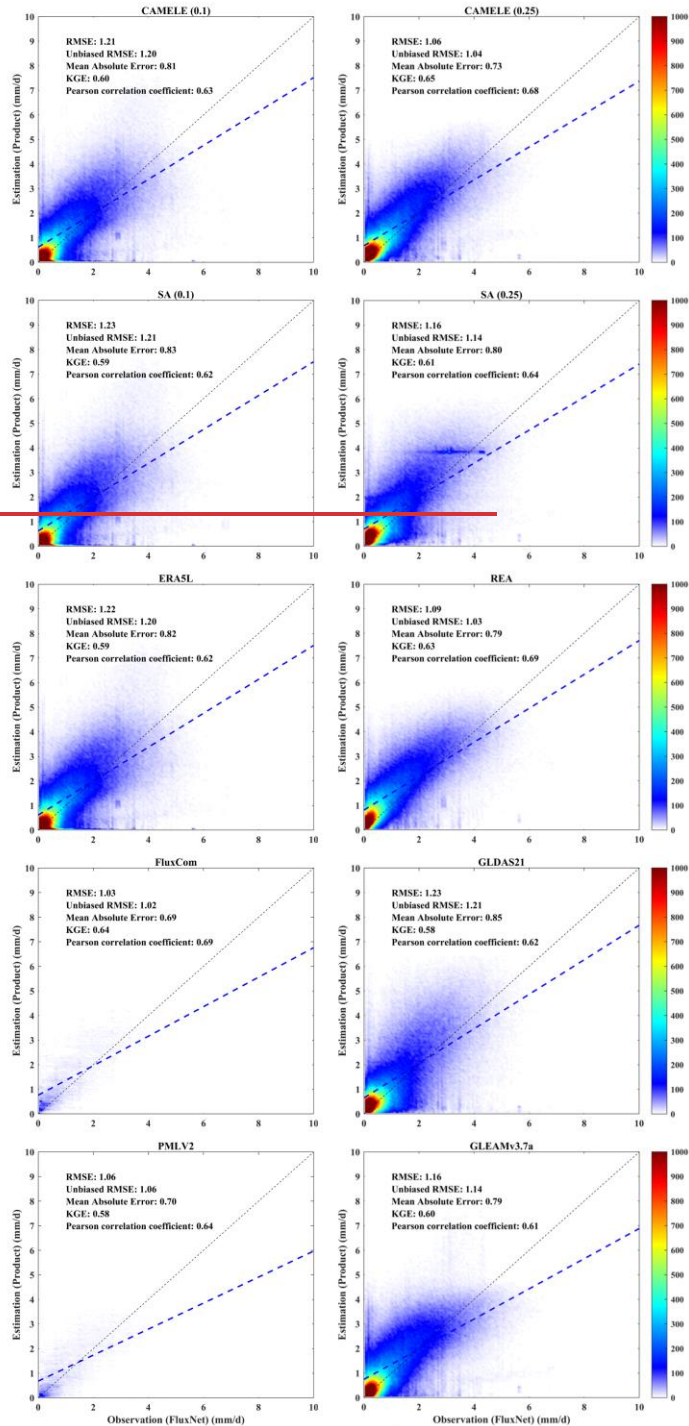
646 the errors between ERA5L and PMLv2 for two time periods: 2000 and 2015 to 2020.
647 Since the analysis of product errors is not the focus of this paper, we provide the
648 results of the IVD in the appendix. Grids with higher random error variances
649 correspond to smaller weights when calculating the weights. The weight distribution
650 calculated at different time intervals is available in the appendix.

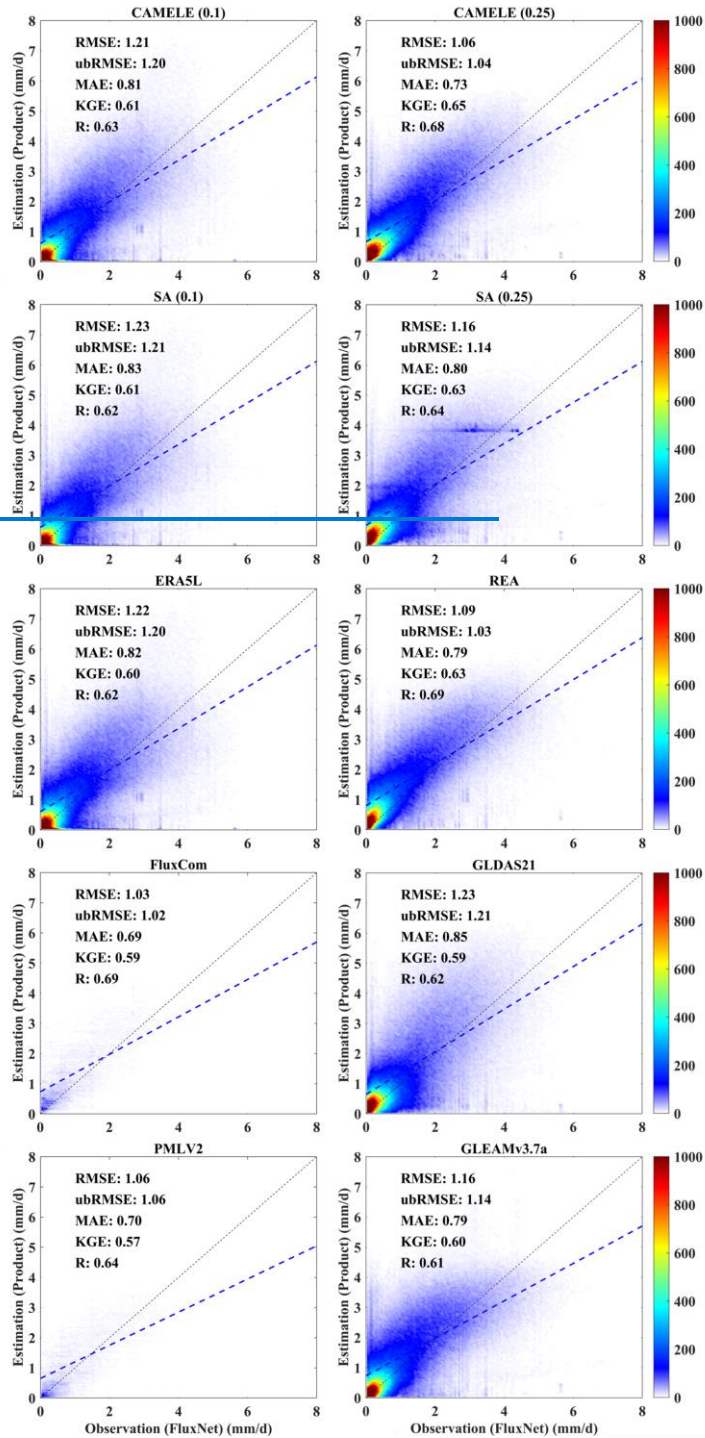
651 5.2.4.2. Site-scale evaluation and comparison

652 At the site scale, the performance of CAMELE was compared with FluxNet as the
653 reference. In this subsection, ~~Figure 6~~~~Figure 5~~~~Figure 4~~ ~~Figure 4~~ and ~~Table 3~~~~Table~~
654 ~~3~~~~Table 3~~~~Table 3~~ correspond to each other, as they integrate data from 212 sites for all
655 available periods, allowing for a comparative analysis of the performance of different
656 products at different times. Similarly, ~~Figure 7~~~~Figure 6~~~~Figure 5~~ and ~~Table 4~~~~Table~~
657 ~~4~~~~Table 4~~ correspond to each other, where different product metrics were calculated
658 for each site, and the calculated metric results were subjected to statistical analysis.

659







663 **Figure 654** Scatter plots of product corresponding to the available period data from
 664 212 FluxNet sites. The colorbar represents the density, with darker colors indicating
 665 higher concentration. The left and right columns present results for 0.1° and 0.25°
 666 resolutions, respectively, with "SA" indicating the results for simple average.

667 Relevant statistical metrics are annotated in their respective figures.

668 The scatter plots in ~~Figure 6~~~~Figure 5~~~~Figure 4~~ demonstrate that CAMELE
 669 consistently performs at 0.1° and 0.25° resolutions. At 0.1° resolution, FluxCom and
 670 PMLv2 showed superior performance with fewer data points due to their original 8-
 671 day average resolution. CAMELE exhibited a performance like ERA5L. At 0.25°
 672 resolution, CAMELE performed comparably to the other datasets, demonstrating
 673 reasonable accuracy. Notably, there was an improvement in the KGE and R indices.
 674 The fitted line closely approximated the 1:1 line, indicating a solid agreement with the
 675 observed values. Moreover, the results obtained from the simple average were also
 676 acceptable, but SA (0.25°) had a concentration of data points between (2-4 mm/d),
 677 possibly due to the inputs having a high concentration within that range. The
 678 assumption that a simple average implies equal performance of each product on every
 679 grid cell is inaccurate; variations in performance exist among different products
 680 across distinct grid cells (regions). ~~Theoretically, the simple average assumes that each~~
 681 ~~product performs equally on each grid cell, which does not accurately reflect the real-~~
 682 ~~world conditions.~~

683 **Table 3** Average values of different metrics for CAMELE and other fusion schemes
 684 corresponding to the available period data from 212 FluxNet sites. The bolded
 685 sections indicate the schemes with the best performance in their respective metrics.

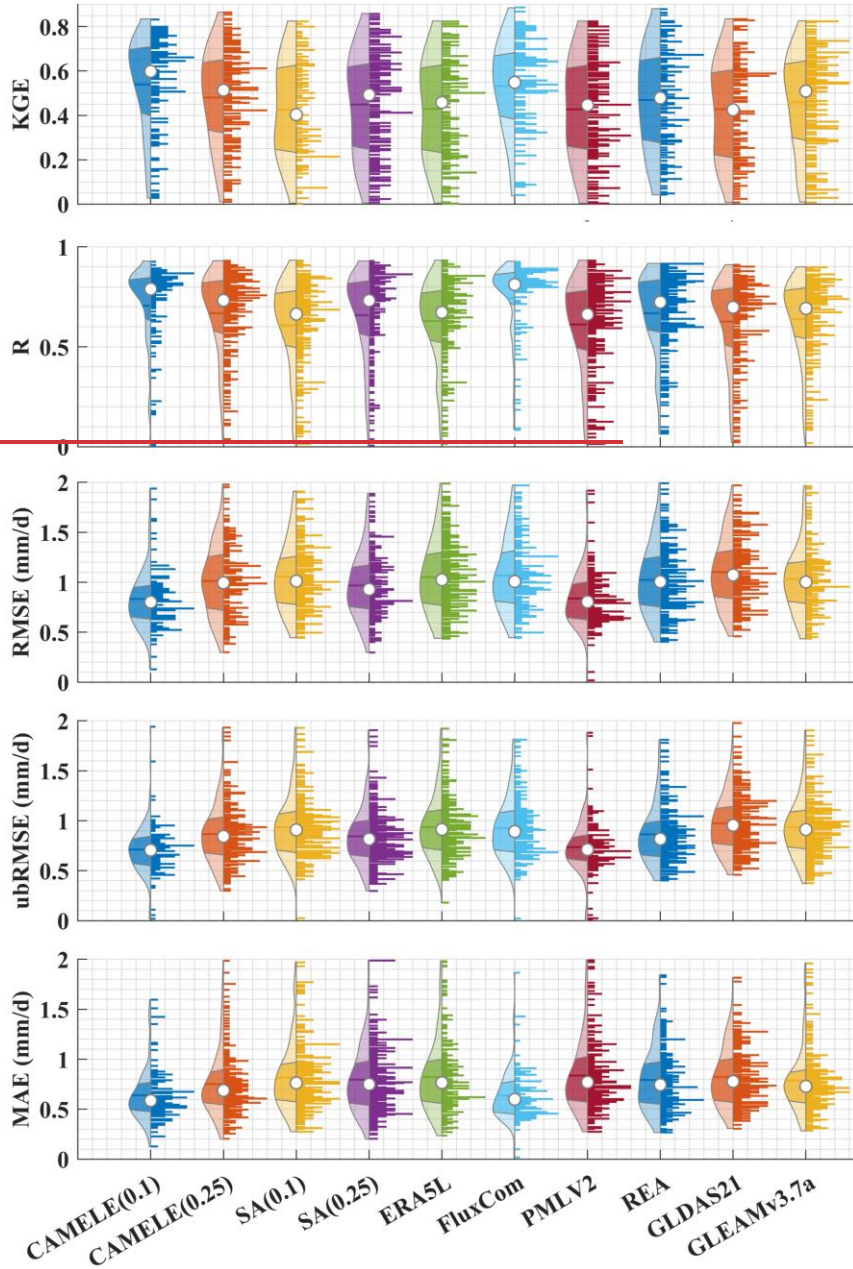
	Product	RMSE (mm/d)	ubRMSE (mm/d)	MAE (mm/d)	KGE	R
	CAMELE	1.21	1.20	0.81	0.6061	0.63
	SA	1.23	1.21	0.83	0.5961	0.62
0.1°-daily	ERA5L	1.22	1.20	0.82	0.5960	0.62
	FluxCom	1.03	1.02	0.69	0.6459	0.69
	PMLv2	1.06	1.06	0.70	0.5857	0.64

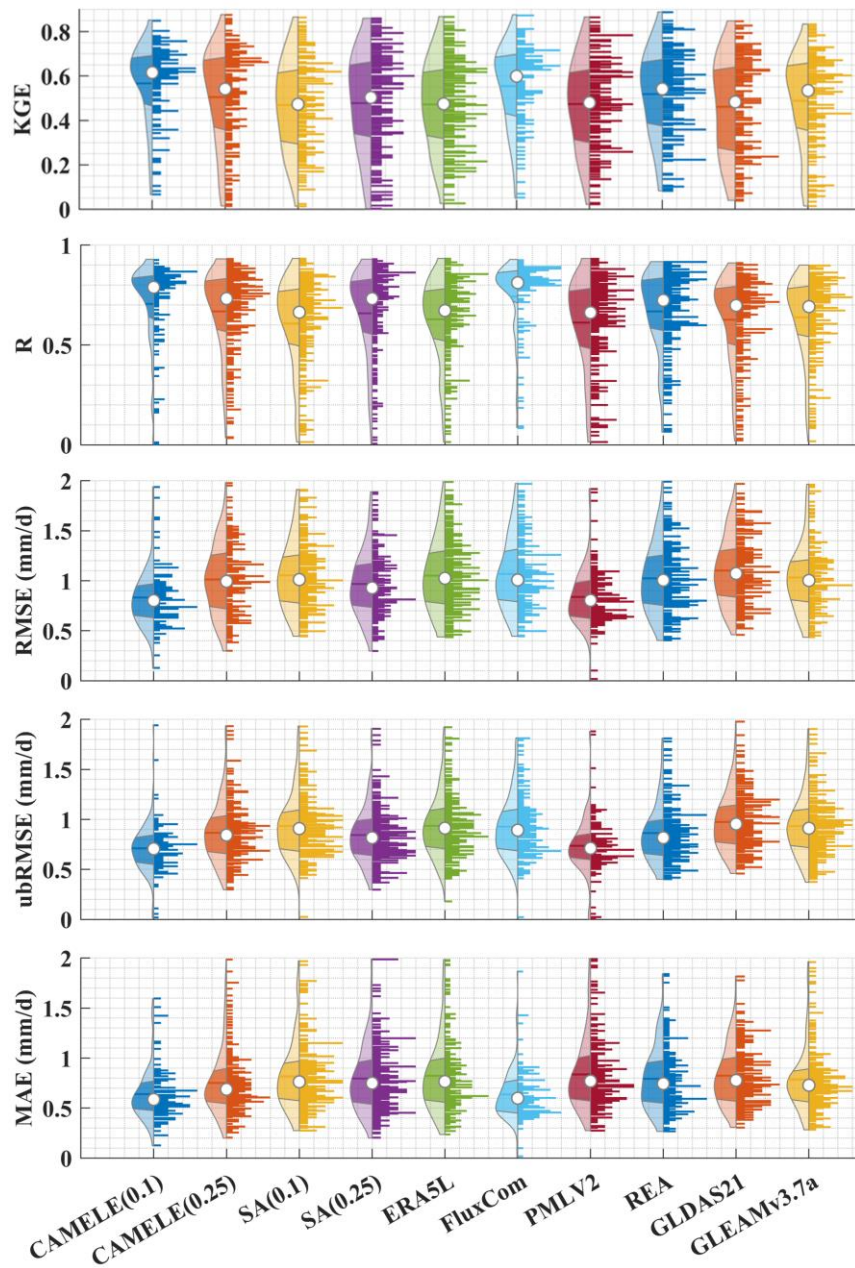
	CAMELE	1.06	1.04	0.73	0.65	0.68
	SA	1.16	1.14	0.80	0.64 0.63	0.64
0.25°-daily	REA	1.09	1.03	0.79	0.63	0.69
	GLDAS21	1.23	1.21	0.85	0.58 0.59	0.62
	GLEAMv3.7a	1.16	1.14	0.79	0.60	0.61

686 The information in ~~Table 3~~**Table 3** corresponds to ~~Figure 6~~**Figure 5** and
687 presents the results of various product indicators. The bolded parts indicate the
688 products with the best corresponding indicators. The results indicate that CAMELE
689 performed well at both 0.1° and 0.25° resolutions, mainly showing improvements in
690 the KGE and R indicators. FluxCom exhibited the best performance; however,
691 considering that this product utilized FluxNet sites for result calibration, this
692 phenomenon is reasonable. In this study, we pooled the data from all 212 available
693 periods at the stations as a reference without considering the differences between
694 individual sites. This approach provided an initial validation of the reliability of
695 CAMELE at all sites.

696 The information in ~~Figure 7~~**Figure 6**~~Figure 5~~ corresponds to the data presented in
697 ~~Table 4~~**Table 4**~~Table 4~~, which involves the calculation of five indicators at each site,
698 followed by statistical analysis of these indicators. From the distribution of the violin
699 plots, it can be observed that a violin plot with a closer belly to 1 indicates better
700 results in terms of the R and KGE indicators. CAMELE performs ~~exceptionally~~-well
701 overall, closely resembling PMLv2 and FluxCom. On the other hand, the results
702 obtained from ~~the~~ Simple Average are relatively poorer. Regarding the RMSE,
703 ubRMSE, and MAE indicators, a violin plot with a closer belly to 0 suggests ~~more~~
704 ~~minor~~**less** errors. ~~CAMELE demonstrates a notable enhancement in performance at~~
705 ~~the 0.1° level. This suggests that the fusion method effectively reduces errors,~~
706 ~~aligning with the original intention of weight calculation, and it compares favorably~~
707 ~~with the products used in the merging scheme~~~~CAMELE shows a significant~~
708 ~~improvement in performance at the 0.1° level. This indicates that the fusion method~~
709 ~~effectively reduces errors, aligning with the original intention of weight calculation.~~

710 Additionally, FluxCom and PMLv2 also exhibit minimal errors, which is expected
711 considering their utilization of FluxNet sites for error correction. Furthermore, SA
712 shows significantly larger errors. Although the simple average method can
713 compensate for positive and negative errors between inputs in some instances, it can
714 also lead to error accumulation, as evidenced by the results in the violin plots.
715





717

718

719

Figure 765 Violin plots obtained by aggregating five different statistical indicators, calculated separately for each site. In each violin plot, the left side represents the

720 distribution, with the shaded area indicating the box plot, the dot representing the
 721 mean, and the right side showing the histogram.

722 **Table 4** Average values of indicators corresponding to different products, calculated
 723 based on the comprehensive results obtained for each site. The bolded sections
 724 indicate the schemes with the best performance in their respective metrics.

Product	RMSE (mm/d)	ubRMSE (mm/d)	MAE (mm/d)	KGE	R	
0.1°-daily	CAMELE	0.83	0.71	<u>0.64</u>	<u>0.5457</u>	0.71
	SA	1.05	0.93	0.82	<u>0.4347</u>	0.61
	ERA5L	1.05	0.94	0.82	<u>0.4347</u>	0.63
	FluxCom	1.07	0.93	<u>0.64</u>	<u>0.5355</u>	0.74
	PMLv2	0.84	0.74	0.84	<u>0.4347</u>	0.61
0.25°-daily	CAMELE	1.03	0.87	0.75	<u>0.5149</u>	0.67
	SA	0.97	0.84	0.80	<u>0.4548</u>	0.66
	REA	1.02	0.86	0.80	<u>0.4748</u>	0.67
	GLDAS21	1.10	0.97	0.83	<u>0.4346</u>	0.63
	GLEAMv3.7a	1.03	0.93	0.79	<u>0.4649</u>	0.64

设置了格式: 字体: 加粗

设置了格式: 字体: 非加粗

725 **Table 4** presents the average values of different metrics in **Figure**
 726 **5**, boldly highlighting the optimal products corresponding to each
 727 metric. It can be observed that CAMELE exhibits significant improvements in
 728 performance at a resolution of 0.1°, particularly in terms of the error metrics RMSE
 729 and ubRMSE, surpassing other products. This further confirms the effectiveness of
 730 our fusion scheme in reducing product errors. Additionally, although the performance
 731 of CAMELE at a resolution of 0.25° is comparable to other products, there is still a
 732 slight decline compared to its performance at 0.1°. This can be attributed partly to the
 733 inherent errors in the input products and partly to the decreasing representativeness of
 734 FluxNet, which serves as the reference at the 0.25° grid. Nevertheless, we can still
 735 consider CAMELE to have good accuracy.



Figure 876



738

739

740

741

742

743

744

745

746

747

Heatmaps of five statistical indicators, where each row corresponds to the mean value for all sites of the specific PFT, and each column corresponds to a product. The product with the best performance for that PFT is highlighted in bold within each row. (a)-(c) represent three error indicators: RMSE, ubRMSE, and MAE; (d)-(e) represent two goodness-of-fit indicators: KGE and R. Heatmap of five indicators calculated separately for each site, classified by PFTs. The top right corner indicates the number of sites corresponding to each type.

Table 5 Optimal product corresponding to different PFTs under various statistical indicators against observations from FluxNet sites

IGBP (n-sites)	RMSE (mm/d)	ubRMSE (mm/d)	MAE (mm/d)	KGE	R	
<i>CRO</i> (20)	CAMELE	CAMELE	CAMELE	PMLv2	CAMELE	
<i>CSH</i> (3)		PMLv2		FluxCom	FluxCom	
<i>DBF</i> (26)		CAMELE		CAMELE		REA
<i>DNF</i> (1)			FluxCom			CAMELE
<i>EBF</i> (15)			CAMELE			GLEAM
<i>ENF</i> (49)			FluxCom		CAMELE	
<i>GRA</i> (39)			PMLv2		CAMELE	CAMELE
<i>MF</i> (9)	CAMELE	CAMELE	CAMELE	REA	FluxCom	
<i>OSH</i> (13)			FluxCom	CAMELE		
<i>SAV</i> (9)			CAMELE	REA		
<i>SNO</i> (1)			PMLv2	FluxCom		CAMELE
<i>WET</i> (21)			CAMELE	CAMELE		
<i>WSA</i> (6)			CAMELE	CAMELE		

748 Furthermore, we classified 212 sites according to PFTs and analyzed the statistical
749 indicators of different PFTs corresponding to each site. The results are represented in
750 [Figure 8](#)~~Figure 7~~~~Figure 6~~ as a heatmap, and the corresponding optimal products for
751 other PFTs sites are marked in [Table 5](#)~~Table 5~~~~Table 5~~. The results show that
752 CAMELE performs the best in almost all PFTs categories, as indicated by various
753 indicators. While on sites where other products perform better, CAMELE's indicators
754 are comparable to the optimal products, albeit slightly inferior. This indicates that our
755 fusion approach effectively combines the advantages of different products, resulting
756 in superior fusion results across different vegetation types.

757 [From the results, it is evident that CAMELE performs well across various vegetation](#)
758 [types. To delve deeper into the reasons behind this performance, we conduct site-scale](#)
759 [analyses at two resolutions, evaluating errors and computed weights for different](#)
760 [PFTs sites. These are visualized in radar chart format in \[Figure 9\]\(#\)~~Figure 8~~~~Figure 7~~.](#)

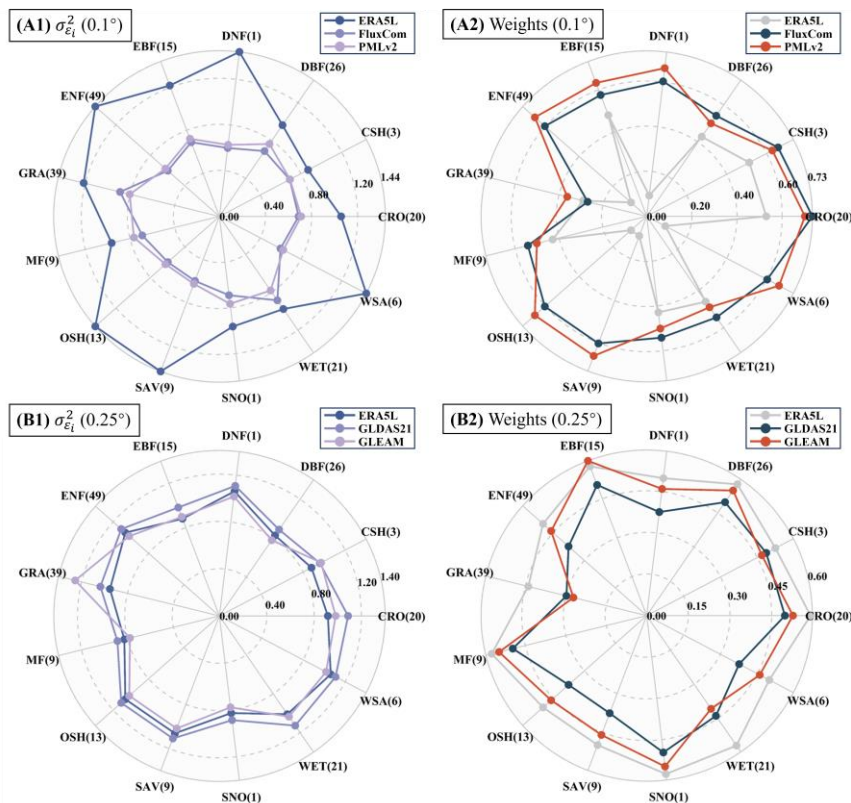


Figure 986 Mean collocation-based errors and weights of different products at various PFTs sites at (A) 0.1° and (B) 0.25° resolutions. The parentheses next to each PFTs name denote the corresponding number of sites.

The results from **Figure 9** ~~Figure 8~~ **Figure 7** demonstrate that the error-weighting calculation method based on collocation effectively considers the error situation of inputs, thereby providing reasonable weight assignments. At 0.1° resolution, ERA5L's error is significantly higher across all PFTs than FluxCom and PMLv2, resulting in relatively lower corresponding weights. FluxCom and PMLv2 exhibit closer performance, with higher weights at most PFT sites. At 0.25° resolution, ERA5L, GLDAS21, and GLEAM perform more evenly, with minimal differences, resulting in closer weights. The weights for different inputs vary noticeably with changes in PFTs, depending on the performance of other products within the same combination.

774 Products with more significant errors correspondingly have lower weights, affirming
775 the rationale behind the fusion method. However, it is essential to note that the
776 presented results depict the mean values of errors and weights across all sites; there
777 might be variations among sites with the same PFTs.

778 In summary, using the filtered daily-scale data from 212 FluxNet sites as a reference,
779 we conducted a benchmark analysis with CAMELE and demonstrated its good fit
780 with the observed data. Additionally, by comparing the performance of different
781 products at each site, we further illustrated that CAMELE exhibits similar or slightly
782 improved accuracy and minor errors compared to existing products.

783 5.3.4.3. Global comparison~~Assessment and comparison of-of~~ **multi-year average** 784 **and linear trend**

785 In this section, we will first analyze and compare the performance of CAMELE with
786 other products in estimating the multi-year mean and extreme values of ET at the site
787 scale. Subsequently, a global-scale analysis will be conducted for the same periods
788 (0.1°: 2001 to 2015; 0.25°: 2000 to 2017) to examine the distribution of multi-year
789 daily average ET calculated by different products. For site comparisons, we have
790 selected monthly mean ET values and three quantiles (5th, 50th, and 95th) to
791 represent the products' performance in estimating ET's average and extreme
792 values.~~This section will compare the multi year average daily scale~~
793 ~~evapotranspiration distributions and their linear trends between CAMELE and other~~
794 ~~products at resolutions of 0.1° and 0.25°. Due to the varying available periods of~~
795 ~~different products, the results presented here are based on calculations using data from~~
796 ~~all available periods, and the corresponding periods are indicated in each figure.~~

797 **Figure 9**~~Table 6;~~

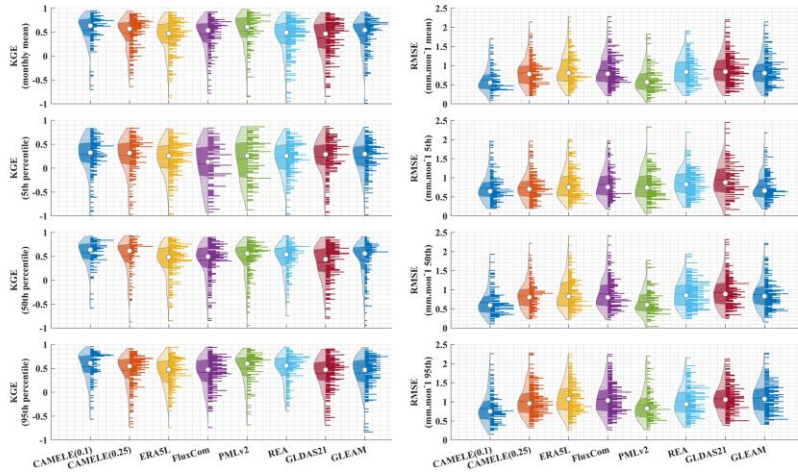


Figure 109 Violin plots depicting the KGE and RMSE metrics calculated for CAMELE and other products based on the monthly mean, 5th, 50th, and 95th percentiles at each FluxNet site. The left four columns represent KGE plots, while the right four columns represent RMSE plots. The dots in the violin plots represent the median, and the horizontal lines represent the mean.

Table 664 Average values of KGE and RMSE corresponding to different products, calculated based on the results obtained for each site. The bolded sections indicate the schemes with the best performance in their respective metrics.

Product		KGE			
		Mean	5 th	50 th	95 th
0.1°-daily	CAMELE	0.54	0.28	0.57	0.54
	ERA5L	0.41	0.21	0.40	0.42
	FluxCom	0.45	0.09	0.42	0.42
	PMLv2	0.52	0.19	0.46	0.50
0.25°-daily	CAMELE	0.47	0.26	0.50	0.45
	REA	0.40	0.21	0.46	0.50
	GLDAS21	0.37	0.23	0.37	0.40
	GLEAMv3.7a	0.43	0.22	0.42	0.40
Product		RMSE (mm/mon)			
		Mean	5 th	50 th	95 th
0.1°-daily	CAMELE	0.63	0.73	0.66	0.83

设置了格式: 上标
 设置了格式: 上标
 设置了格式: 上标
 设置了格式: 字体: Times New Roman, 小四, 加粗
 设置了格式: 字体: 加粗
 设置了格式: 字体: Times New Roman, 小四, 加粗
 设置了格式: 字体: 加粗
 设置了格式: 字体: Times New Roman, 小四, 加粗
 设置了格式: 字体: Times New Roman, 小四, 加粗
 设置了格式: 字体: Times New Roman, 小四
 设置了格式: 字体: Times New Roman, 小四
 设置了格式: 字体: Times New Roman, 小四
 设置了格式: 字体: Times New Roman, 小四
 设置了格式: 字体: Times New Roman, 小四
 设置了格式: 字体: Times New Roman, 小四
 设置了格式: 字体: Times New Roman, 小四
 设置了格式: 字体: Times New Roman, 小四
 设置了格式: 字体: Times New Roman, 小四
 设置了格式: 字体: Times New Roman, 小四
 设置了格式: 字体: Times New Roman, 小四, 加粗
 设置了格式: 字体: Times New Roman, 小四, 加粗
 设置了格式: 字体: 加粗
 设置了格式: 字体: Times New Roman, 小四, 加粗
 设置了格式: 字体: Times New Roman, 小四
 设置了格式: 字体: Times New Roman, 小四
 设置了格式: 字体: Times New Roman, 小四
 设置了格式: 字体: Times New Roman, 小四
 设置了格式: 字体: Times New Roman, 小四
 设置了格式: 字体: Times New Roman, 小四
 设置了格式: 字体: Times New Roman, 小四
 设置了格式: 字体: Times New Roman, 小四
 设置了格式: 字体: Times New Roman, 小四
 设置了格式: 字体: Times New Roman, 小四
 设置了格式: 字体: Times New Roman, 小四
 设置了格式: 字体: Times New Roman, 小四
 设置了格式: 字体: Times New Roman, 小四, 加粗
 设置了格式: 字体: Times New Roman, 小四, 加粗
 设置了格式: 字体: Times New Roman, 小四, 加粗

	<u>ERA5L</u>	<u>0.89</u>	<u>0.83</u>	<u>0.91</u>	<u>1.09</u>
	<u>FluxCom</u>	<u>0.87</u>	<u>0.83</u>	<u>0.89</u>	<u>1.07</u>
	<u>PMLv2</u>	<u>0.63</u>	<u>0.80</u>	<u>0.68</u>	<u>0.91</u>
	<u>CAMELE</u>	<u>0.81</u>	<u>0.74</u>	<u>0.84</u>	<u>1.01</u>
<u>0.25°-daily</u>	<u>REA</u>	<u>0.86</u>	<u>0.85</u>	<u>0.88</u>	<u>1.01</u>
	<u>GLDAS21</u>	<u>0.90</u>	<u>0.95</u>	<u>0.93</u>	<u>1.08</u>
	<u>GLEAMv3.7a</u>	<u>0.85</u>	<u>0.75</u>	<u>0.88</u>	<u>1.10</u>

设置了格式: 字体: Times New Roman, 小四

设置了格式: 字体: Times New Roman, 小四

设置了格式: 字体: Times New Roman, 小四

设置了格式: 字体: Times New Roman, 小四

设置了格式: 字体: Times New Roman, 小四

设置了格式: 字体: Times New Roman, 小四

设置了格式: 字体: Times New Roman, 小四

设置了格式: 字体: Times New Roman, 小四

设置了格式: 字体: Times New Roman, 小四, 加粗

设置了格式: 字体: 加粗

设置了格式: 字体: Times New Roman, 小四

设置了格式: 字体: Times New Roman, 小四

设置了格式: 字体: Times New Roman, 小四

设置了格式: 字体: Times New Roman, 小四, 加粗

设置了格式: 字体: Times New Roman, 小四, 加粗

设置了格式: 字体: Times New Roman, 小四, 加粗

设置了格式: 字体: Times New Roman, 小四

设置了格式: 字体: Times New Roman, 小四

设置了格式: 字体: Times New Roman, 小四

设置了格式: 字体: Times New Roman, 小四

设置了格式: 字体: Times New Roman, 小四, 加粗

设置了格式: 字体: Times New Roman, 小四

设置了格式: 字体: Times New Roman, 小四

设置了格式: 字体: Times New Roman, 小四

设置了格式: 字体: Times New Roman, 小四

设置了格式: 字体: Times New Roman, 小四

设置了格式: 字体: Times New Roman, 小四

设置了格式: 字体: Times New Roman, 小四

设置了格式: 字体: Times New Roman, 小四

设置了格式: 字体: Times New Roman, 小四

设置了格式: 字体: Times New Roman, 小四

设置了格式: 字体: Times New Roman, 小四

设置了格式: 字体: Times New Roman, 小四

设置了格式: 字体: Times New Roman, 小四

设置了格式: 字体: Times New Roman, 小四

设置了格式: 字体: Times New Roman, 小四

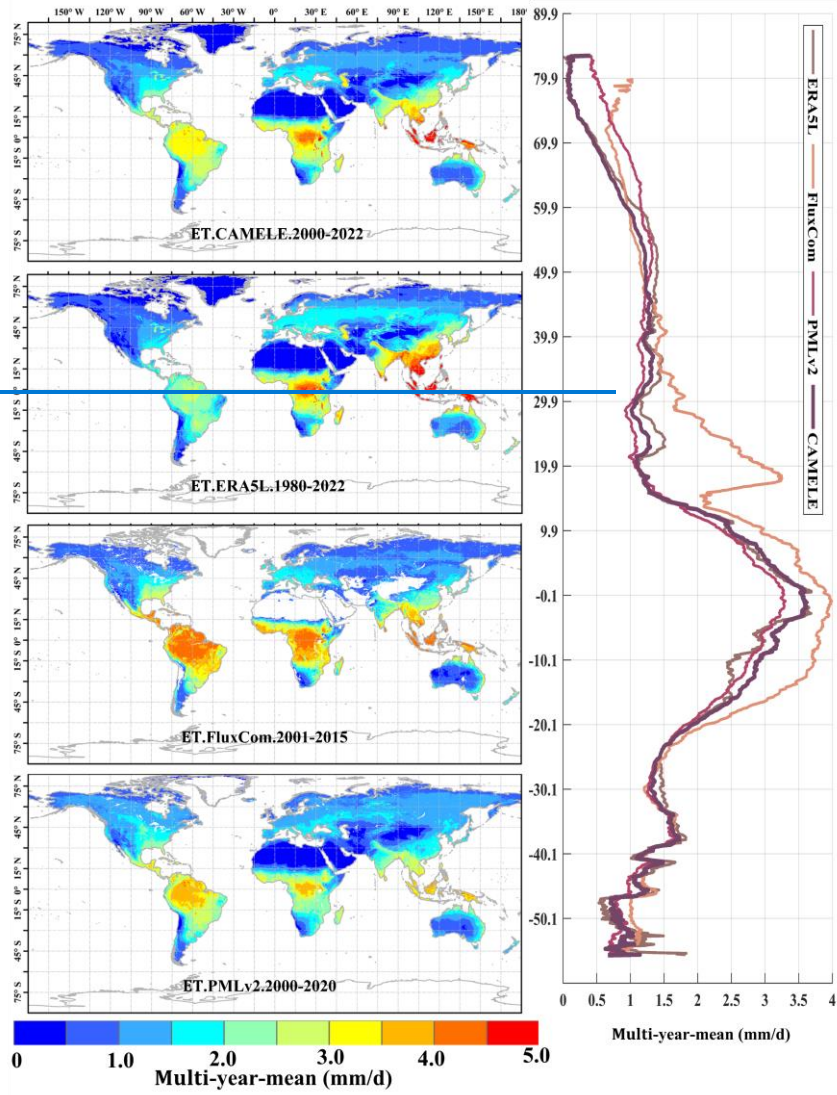
设置了格式: 字体: Times New Roman, 小四

设置了格式: 字体: Times New Roman, 小四

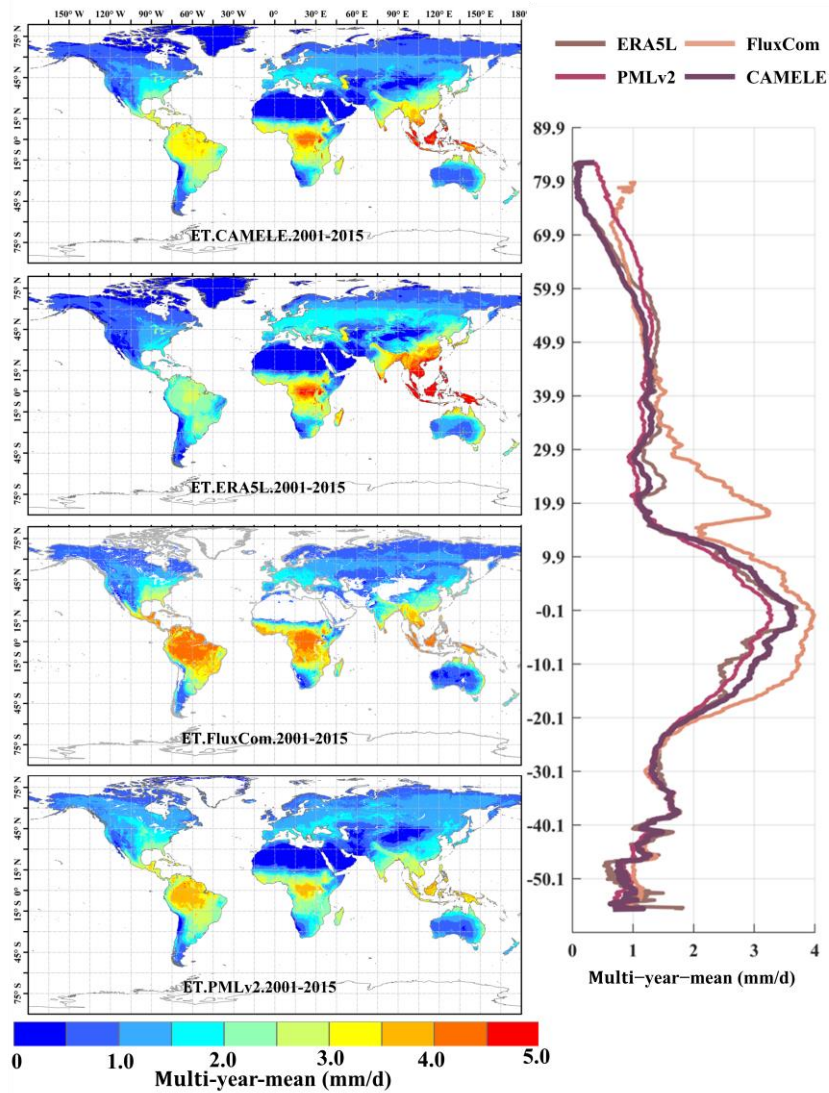
带格式的: 居中

807 The information in Figure 10 corresponds to the data presented in
 808 Table 6, which involves the calculation of KGE and RMSE at each
 809 site, followed by statistical analysis. From the distribution of the violin plots, it can be
 810 observed that a violin plot with a closer belly to 1 indicates better results in terms of
 811 the KGE.
 812 The results show that CAMELE outperforms other products in the estimation of
 813 monthly averages and the 5th, 50th, and 95th percentiles at both 0.1° and 0.25°
 814 resolutions. Its performance in capturing monthly averages is noteworthy, with a
 815 noticeable improvement in the KGE and RMSE metrics relative to the inputs.
 816 Examining the results for percentiles, CAMELE shows a relatively poorer estimation
 817 for shallow values (5th percentile) but still demonstrates some improvement
 818 compared to the input data, albeit influenced by input errors.
 819 At 0.1°, PMLv2 and FluxCom perform just below the fusion result, aligning with the
 820 previous error and weight analysis. At 0.25°, GLEAM and REA closely follow
 821 CAMELE, with REA exhibiting slightly better estimation results for extremely high
 822 values (95th percentile) than CAMELE. Despite this, the analysis results still indicate
 823 that the products obtained reflect well the multi-year averages and extremes of ET,
 824 holding promise as reliable products for analyzing ET variations.

Figure 8



826



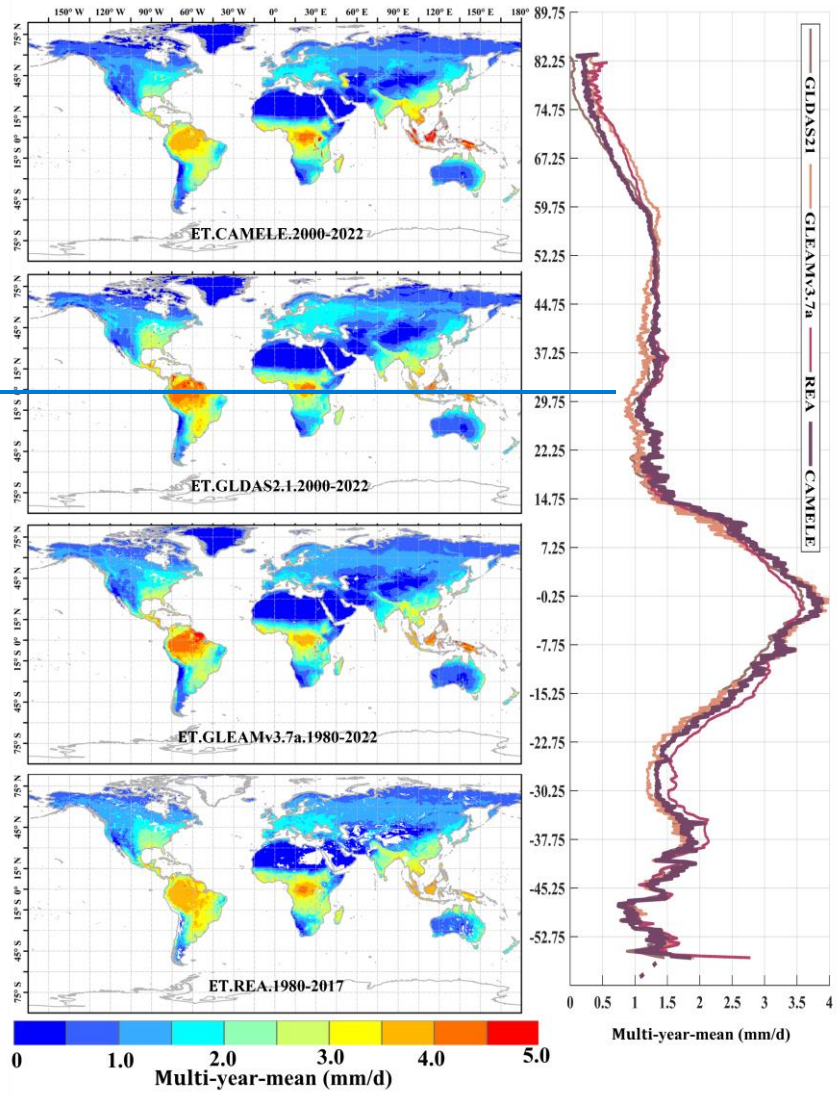
827

828 **Figure 1107** **FIGURE.7** Global distribution of multi-year daily average ET at 0.1°
 829 for CAMELE, ERA5L, FluxCom, and PMLv2, depicted alongside corresponding
 830 variation curves of average with latitude.

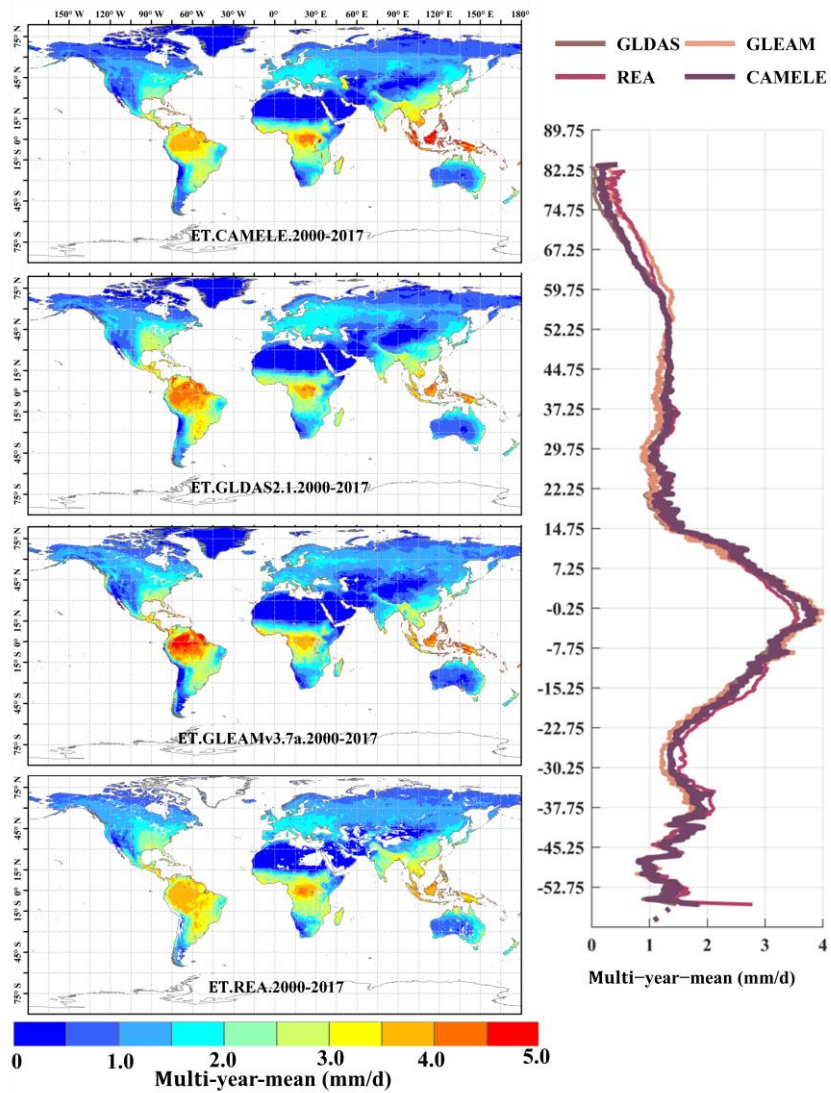
831 The results in **Figure 11** **Figure-10** **Figure-7** indicate significant differences in the
 832 multi-year daily average distribution of global evapotranspiration (ET) among
 833 different products. Specifically, ERA5L shows noticeably higher values in East Asia

834 than other products, while FluxCom and PMLv2 exhibit higher values in the Amazon
835 rainforest and southern Africa regions. This distribution pattern is consistent with the
836 error results obtained from the EIVD calculation, indicating that these products
837 possess certain uncertainties in the regions. In terms of the latitudinal distribution
838 pattern, except for FluxCom, which displays distinct fluctuations, the variability
839 among the other products is relatively similar. This suggests that despite spatial
840 differences among the different products, they maintain consistency in the overall
841 quantity.

842 ~~Figure 12~~~~Figure 11~~~~Figure 9~~ presents the results with a resolution of 0.25° . It can be
843 observed that compared to the 0.1° distribution, the spatial distribution of annual
844 average evapotranspiration (ET) is more consistent among different products at 0.25° ,
845 showing larger ET values in tropical regions. The main differences are concentrated
846 in the Amazon rainforest and the Congo Basin, where GLEAM and GLDAS results
847 are higher than REA's. The assigned weights for REA's inputs (MERRA2, GLDAS,
848 and GLEAM.) are approximately equal in these two regions, each contributing about
849 one-third to the overall calculation~~REA utilizes MERRA2 as input data, while~~
850 ~~GLDAS and GLEAM have weights of approximately close to 1/3 each~~ (Lu et al.,
851 2021). This balanced allocation results in the REA being distributed among them
852 roughly equally over multiple years in these two regions. Therefore, the distribution
853 ~~of REA falls between GLDAS and GLEAM, which is understandable.~~ The latitude
854 variation plots show that the results from each product are very close, providing
855 additional evidence for the reliability of CAMELE.

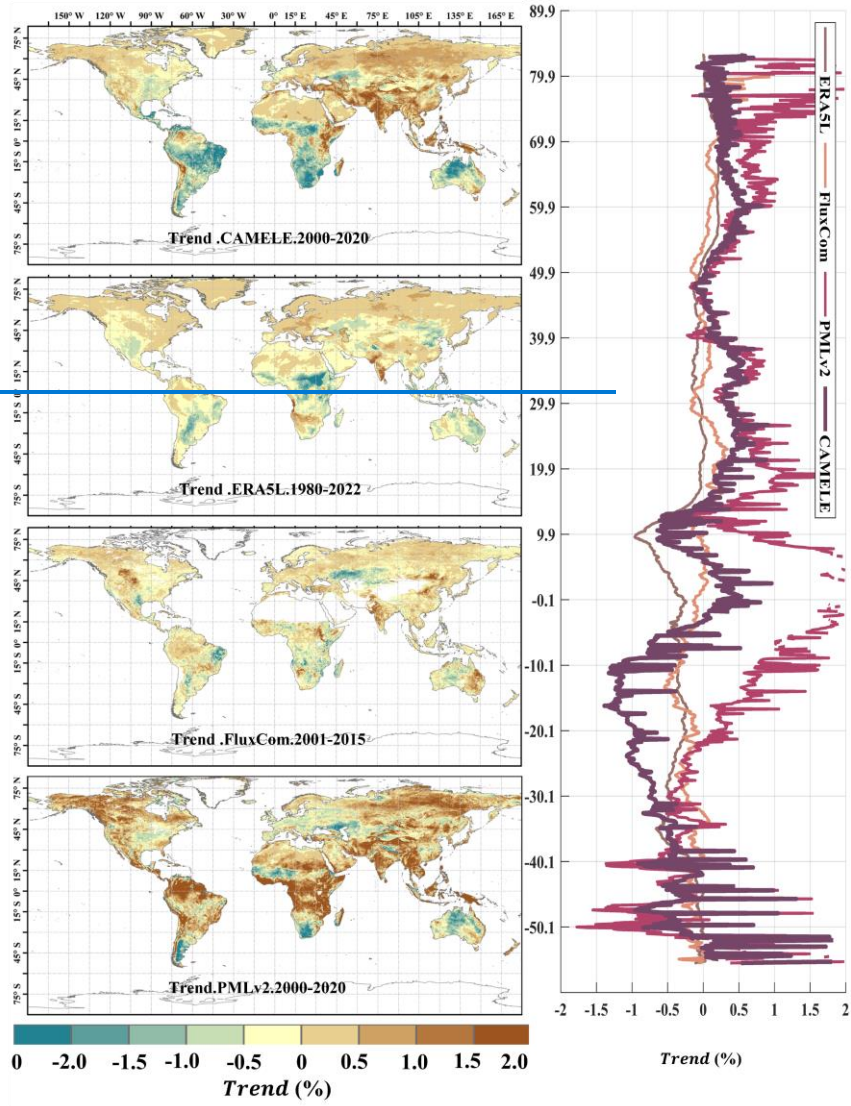


856
857

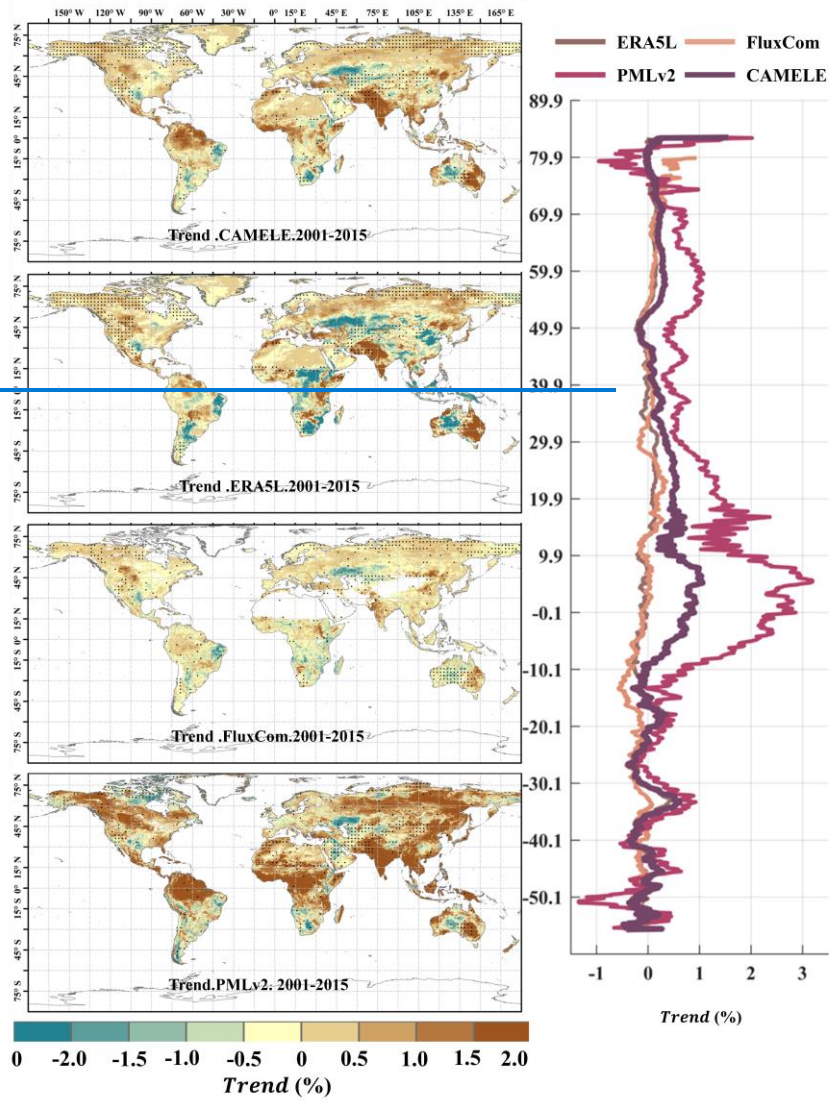


858

859 **Figure 12118FIGURE.8** Global distribution of multi-year daily average ET at 0.25°
 860 for CAMELE, GLDAS2.1, GLEAMv3.7a, and REA, depicted alongside
 861 corresponding variation curves of average with latitude.



862



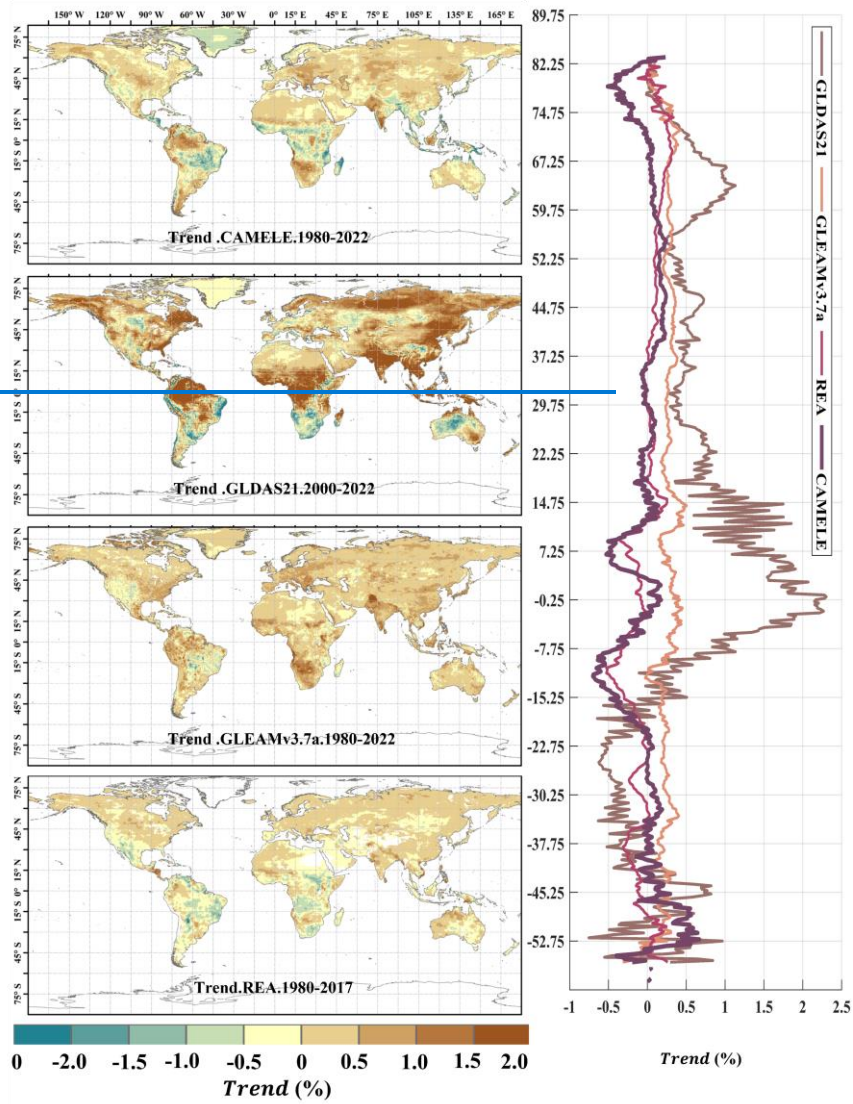
863

864

865

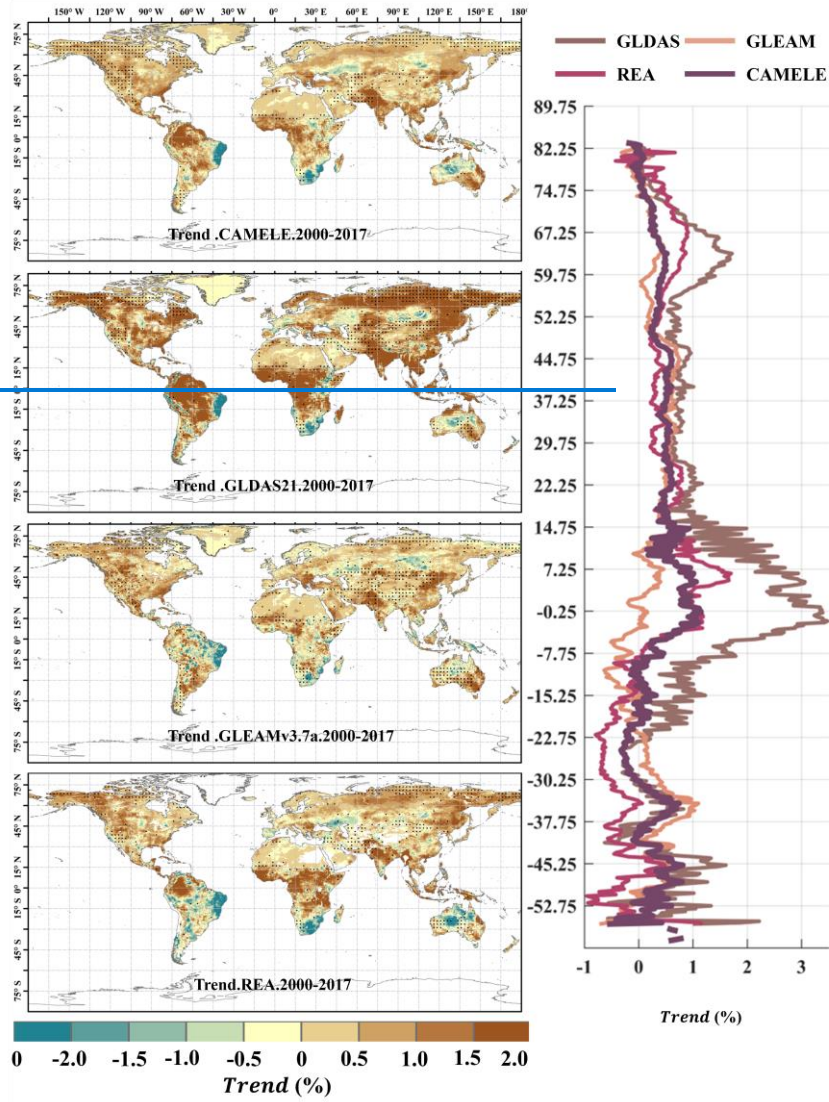
866

Figure 109 **FIGURE.9** Global distribution of multi-year linear trend at 0.1° for CAMELE, ERA5L, FluxCom, and PMLv2, depicted alongside corresponding variation curves of average with latitude. (图名要改)



867

868



869

870 **Figure 11** **FIGURE.10** Global distribution of multi year linear trend at 0.25° for
 871 CAMELE, GLDAS2.1, GLEAMv3.7a, and REA, depicted alongside corresponding
 872 variation curves of average with latitude. (图名要改)

873 **Figure 10** **Figure 10** Figures 9 and **Figure 11** **Figure 11** present the linear trends of
 874 multi year daily scale evapotranspiration (ET) calculated for different products at

875 resolutions of 0.1° and 0.25°, respectively. The corresponding latitude dependent
876 variations of the rate of change are shown on the right side. It can be observed that the
877 differences in linear trends among the different products are more significant than the
878 multi year averages, and in some regions, they even exhibit opposite trends. For
879 example, at 0.1° resolution, PMLv2 shows a global increase of 1.0% in ET in most
880 regions, while the results from CAMELE, ERA5L, and PMLv2 indicate a slight
881 decrease in ET in the Amazon rainforest, southern Africa, and northwestern Australia.
882 Among them, CAMELE exhibits a more pronounced decreasing trend. At 0.25°
883 resolution, except for GLDAS2.1, which shows an apparent global increase in ET, the
884 results from CAMELE, GLEAMv3.7a, and REA indicate more minor variations in
885 global ET.

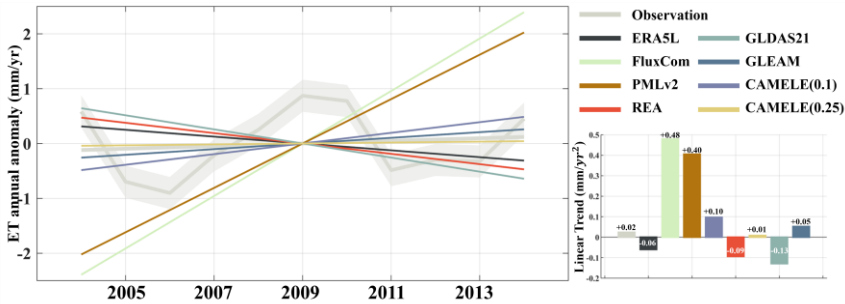
886 To calculate the linear trend more reasonably, we focused on the available years for
887 different products without uniformly applying the same time range, as this could
888 introduce specific impacts on the comparison of results. Furthermore, it can be
889 observed that the linear trend obtained at 0.25° is milder than that of 0.1°. The grid
890 size and the characteristics of the data itself influence this. This disparity can be
891 ascribed to a confluence of factors, prominently including variances in grid size and
892 inherent data attributes. Such nuances in trend outcomes illuminate the complexities
893 associated with working across diverse datasets.

894 In parallel, it is worth noting that, despite the regional disparities that may arise when
895 contrasting the trends by CAMELE with inputs, a noteworthy consistency emerges
896 when examining these trends along latitudinal gradients. This notable alignment
897 signifies the robustness of CAMELE to some extent. It underscores the capacity of
898 CAMELE to capture ET patterns, providing further insights for the scientific
899 community.

900 4.4. Assessment and comparison of linear trend and seasonality

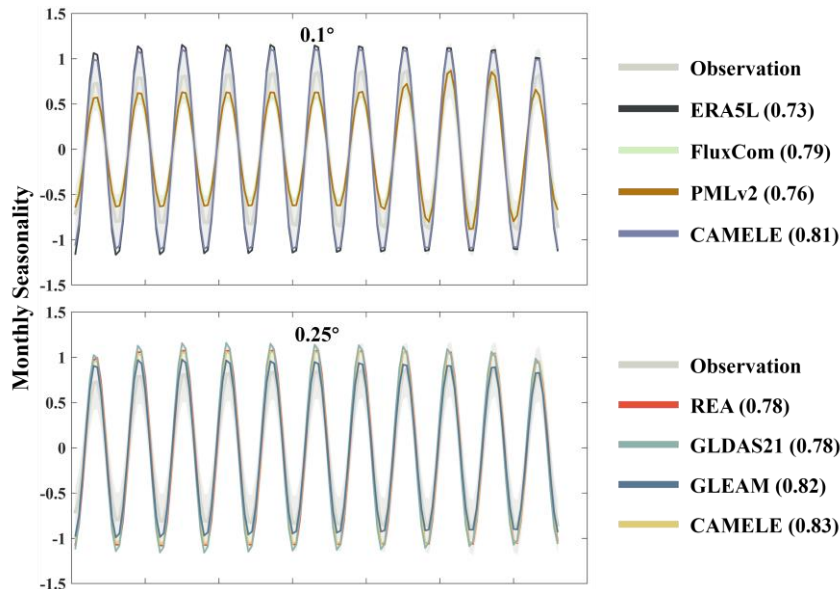
901 In this section, we first validate and compare the performance of CAMELE with other

902 [products in estimating multi-year trends and seasonality at the site scale. Due to the](#)
 903 [inconsistent time lengths of FluxNet sites, trends at many sites are not significant.](#)
 904 [Therefore, we deliberately selected 13 sites with continuous evapotranspiration \(ET\)](#)
 905 [observations for the same 11-year period \(2004 to 2014\) and with significant trends.](#)
 906 [The annual ET values for each year were calculated as the mean of the 13 sites for](#)
 907 [that year, allowing the computation of linear trends and seasonality. We employed](#)
 908 [singular spectrum analysis \(SSA\), which assumes an additive decomposition \$A = LT\$](#)
 909 [+ \$ST + R\$. In this decomposition, \$LT\$ represents the long-term trend in the data, \$ST\$ is](#)
 910 [the seasonal or oscillatory trend \(or trends\), and \$R\$ is the remainder.](#)



911
 912 **Figure 131214** [Comparison of linear trend from 2004 to 2014 among 13 FluxNet](#)
 913 [sites using CAMELE and other products. The trends have been subjected to SSA](#)
 914 [decomposition, removing seasonality. The gray enveloping line represents the mean](#)
 915 [plus the standard deviation of the 13 sites.](#)

设置了格式: 字体: 非加粗



916

917

918

919

920

921

922

923

924

925

926

927

928

929

930

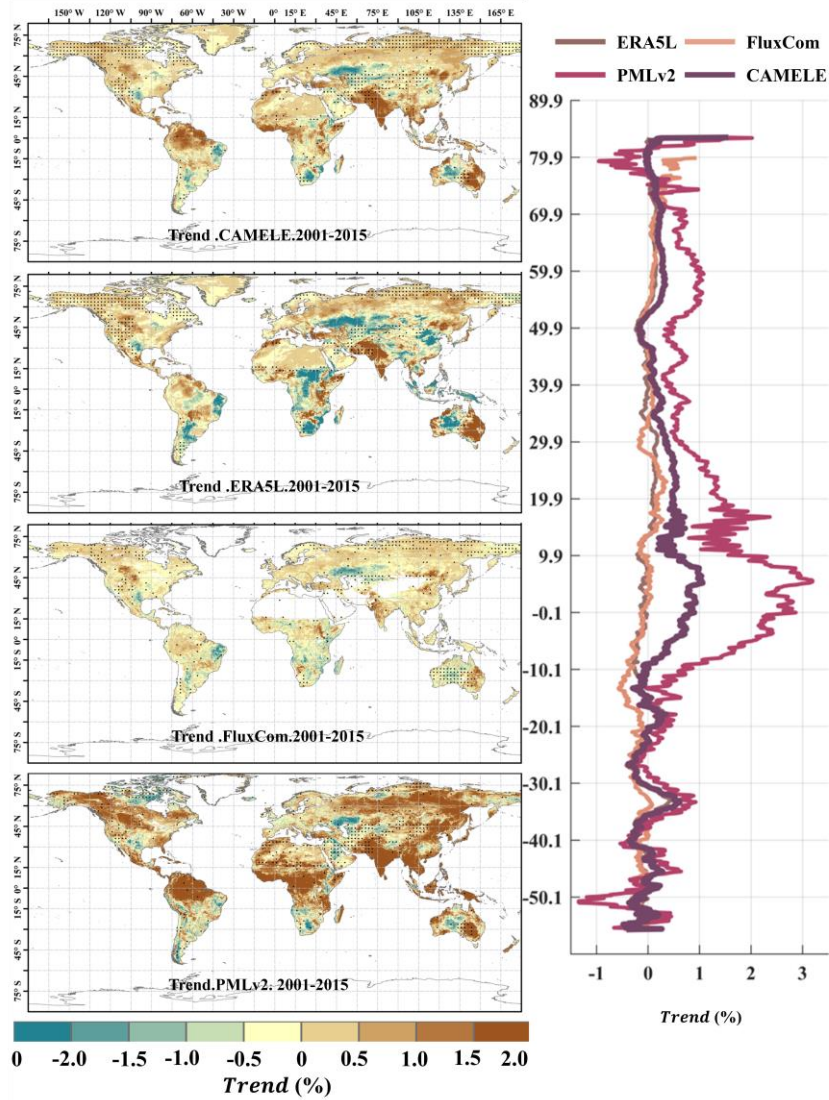
931

932

Figure 14 Comparison of seasonal variations from 2004 to 2014 among 13 FluxNet sites using CAMELE and other products. The seasonality has been obtained through SSA decomposition, with the gray area representing the observed values. The parentheses in each product name indicate the KGE coefficient comparing with the observed values.

Figure 13 In **Figure 13** **Figure 12** **Figure 12** and **Figure 14** **Figure 13** **Figure 13**, based on observations from FluxNet sites, we analyzed the performance of CAMELE and other products in estimating the linear trend and seasonality of ET over multiple years. It is important to note that we only present the analysis results for 13 sites with continuous 11-year observations, and the performance of different ET products in trend estimation at individual sites still varies, not fully reflecting the overall performance on all grids in terms of trend and seasonality. Nevertheless, such a comparison can still provide valuable insights. Examining the results of the linear trend, both PMLv2 and FluxCom exhibit a significant upward trend, well above the observations. On the contrary, ERA5L, GLDAS, and REA show a noticeable downward trend, while CAMELE demonstrates

933 a gradual upward trend closer to the observations. Additionally, GLEAM slightly
934 outperforming CAMELE at a resolution of 0.25°. Overall, CAMELE shows good
935 agreement with site observations in capturing the multi-year linear trend of ET.
936 Continuing with the analysis of seasonality, the KGE index comparing each product's
937 results with observed values is provided in parentheses next to the product name.
938 Generally, all products exhibit a good representation of ET's seasonal variations.
939 CAMELE's 0.1° seasonal results closely match FluxCom (with the two lines almost
940 overlapping). However, the fluctuations it reflects are higher than the observed values.
941 This is likely due to keeping the 8-day average results of FluxCom consistent with
942 PMLv2 every 8 days, and the variability in ET primarily originates from ERA5L
943 results. This aspect may need improvement in subsequent research, ~~suggesting a~~
944 ~~potential need for improvement in future research.~~ At 0.25°, CAMELE's seasonal
945 representation is closer to the observed results. The differences in CAMELE's
946 performance at the two resolutions are mainly attributed to input variations, which we
947 discuss in the following section as potential areas for improvement.
948 The results indicate that CAMELE effectively captures the multi-year changes in ET,
949 but at 0.1°, it tends to overestimate seasonal fluctuations. We further generated global
950 maps of multi-year linear trends in ET, estimating trends using Theil–Sen's slope
951 method and testing significance with the Mann–Kendall method. The dotted areas
952 indicate trends passing a significance test at a 5% level.



953

954

955

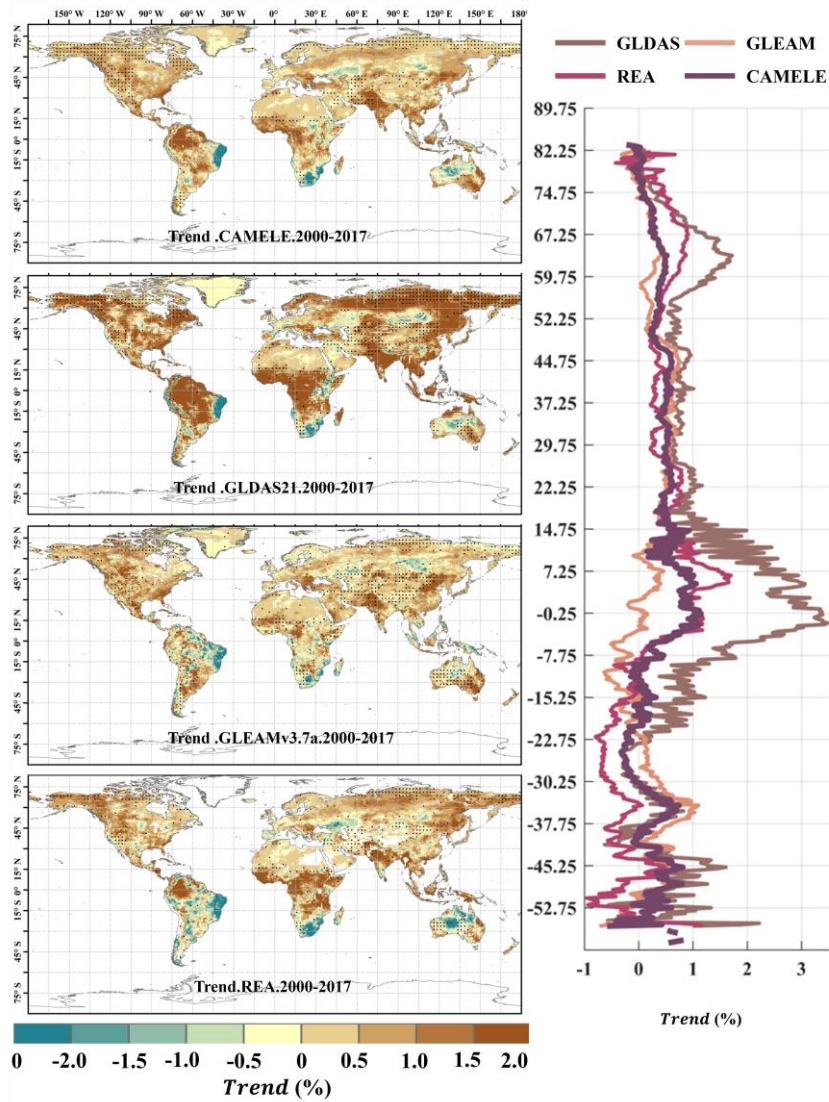
956

957

958

959

Figure 151411 [Global distribution of multi-year linear trend at 0.1° for CAMELE, ERA5L, FluxCom, and PMLv2, depicted alongside corresponding average trend with latitude. The trend is estimated with Theil–Sen’s slope method, and the significance level is tested with the Mann–Kendall method. The dotted area indicates that the trend has passed the significance test at 5 % level.](#)



960

961 **Figure 16** [Global distribution of multi-year linear trend at 0.25° for CAMELE,](#)
 962 [GLDAS2.1, GLEAMv3.7a, and REA, depicted alongside corresponding average](#)
 963 [trend with latitude. The trend is estimated with Theil–Sen’s slope method, and the](#)
 964 [significance level is tested with the Mann–Kendall method. The dotted area indicates](#)
 965 [that the trend has passed the significance test at 5 % level.](#)

966 **Figure 15** [Figure 14](#) [Figure 14](#) [Figure 11](#) and [Figure 16](#) [Figure 15](#) [Figure 12](#) present

域代码已更改

域代码已更改

967 [the linear trends of multi-year daily scale evapotranspiration \(ET\) calculated for](#)
968 [different products at resolutions of 0.1° and 0.25°, respectively. The corresponding](#)
969 [latitude-dependent variations of the rate of change are shown on the right side. It can](#)
970 [be observed that the differences in linear trends among the different products are more](#)
971 [significant than the multi-year averages, and in some regions, they even exhibit](#)
972 [opposite trends. For example, at 0.1° resolution, PMLv2 shows a global increase of](#)
973 [1.0% in ET in most regions, while the results from CAMELE, ERA5L, and PMLv2](#)
974 [indicate a milder increase in ET in the Amazon rainforest, southern Africa, and](#)
975 [northwestern Australia. At 0.25° resolution, except for GLDAS2.1, which shows an](#)
976 [apparent global increase in ET, the results from CAMELE, GLEAMv3.7a, and REA](#)
977 [indicate milder variations in global ET.](#)

978 **6.5. Discussion**

979 **6.1.5.1. Impact of underlying assumptions in collocation analysis**

980 [The collocation analysis system relies on key assumptions, including linearity \(linear](#)
981 [regression model\), stationarity \(unchanged probability distribution over time\), error](#)
982 [orthogonality \(independence between random error and true signal\), and zero error](#)
983 [cross-correlation \(independence between random errors\). Potential error](#)
984 [autocorrelation is considered with lag-1 \[day\] series. Various studies have examined](#)
985 [the validity and impact of these assumptions](#)~~The collocation analysis system relies on~~
986 ~~several fundamental assumptions, namely: (i) Linearity: a linear regression model that~~
987 ~~describes the relationship between the true signal and the datasets; (ii) Stationarity:~~
988 ~~the unconditional joint probability distribution of the signal and the random error of~~
989 ~~estimates remains unchanged when shifted in time; (iii) Error Orthogonality:~~
990 ~~independence between the random error of estimates (e.g., evapotranspiration product)~~
991 ~~and the true signal (assumed unknown true evapotranspiration value); and (iv) Zero~~
992 ~~Error Cross Correlation: independence between random errors of relevant datasets.~~

993 ~~Additionally, potential error autocorrelation must be considered when incorporating~~
994 ~~the lag 1 [day] series into the triplet (Kim et al., 2021b; Dong et al., 2020a, 2019).~~

995 Numerous studies have examined the validity of these assumptions and their impact
996 on the outcomes if violated (Tsamalis, 2022; Duan et al., 2021; Gruber et al., 2020).

997 ~~Thus, we will provide a concise and accurate account of the implications resulting~~
998 ~~from breaches of these assumptions.~~

999 The linearity assumption shapes the error model by including additive and
1000 multiplicative biases and zero-mean random error. Although some studies have
1001 explored the application of a nonlinear rescaling technique (Yilmaz and Crow, 2013;
1002 Zwieback et al., 2016), those efforts are primarily limited to soil moisture signals and
1003 often fail to accurately represent the true signal unless all datasets share a similar
1004 signal-to-noise ratio (SNR). However, it is worth noting that after rescaling processes,
1005 such as cumulative distribution function (CDF) matching or climatology removal, the
1006 resulting time series (anomalies) are often considered linearly related to the truth since
1007 higher-order error terms are removed. In addition, multiplicative relationships have
1008 been more commonly identified in rainfall products (Li et al., 2018). In contrast,
1009 collocation analysis within the context of ET products frequently suggests that linear
1010 relationships are reasonable (Li et al., 2022; Park et al., 2023). Therefore, the linear
1011 error model remains a robust implementation, though it has the potential for
1012 improvement through rescaling techniques. ~~(Li et al., 2018)(Li et al., 2022; Park et al.,~~
1013 ~~2023)~~

1014 Regarding violating the stationarity assumption, the evapotranspiration signal does
1015 not strictly adhere to this characteristic. However, by collocating triplets with similar
1016 magnitude variations, the influence of this violation is minimized. Nonetheless,
1017 disparities in climatology between datasets can still arise for various reasons (Su and
1018 Ryu, 2015). Several proposed alternatives aim to address this issue, such as removing
1019 the climatology of inputs (Stoffelen, 1998; Yilmaz and Crow, 2014; Draper et al.,
1020 2013) and subsequently analyzing the random error variance of the anomalies (Dong

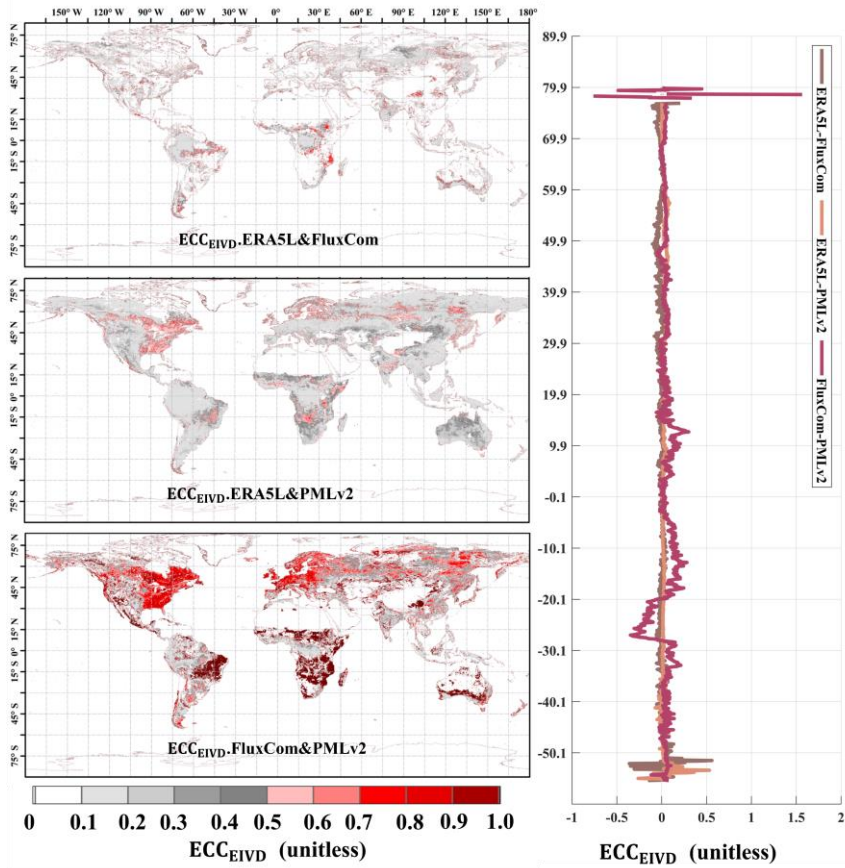
1021 et al., 2020b). Nevertheless, obtaining a reliable estimation of climatology proves
1022 challenging in practice.

1023 The assumption of error orthogonality assumes independence between random error
1024 and true signal, i.e., $\sigma_{\varepsilon_i\theta} = 0$. A few studies have examined this assumption. Yilmaz
1025 and Crow (2014) investigated such violations using four in situ sites and concluded
1026 that the impact is negligible since rescaling mitigates or compensates for bias.
1027 Additionally, non-orthogonality results in non-zero error cross-correlation (ECC),
1028 although the latter is considered more important. Vogelzang et al. (2022) also
1029 investigated this violation recently and demonstrated minimal second-order impact.

1030 Non-zero ECC conditions introduce more substantial bias in the results compared to
1031 other violations mainly due to two reasons: (1) they cannot be mitigated by rescaling;
1032 (2) they cannot be compensated even with equal magnitude for all inputs; and (3) they
1033 have been frequently reported in recent studies for various variables (Li et al., 2018,
1034 2022; Gruber et al., 2016b). Gruber et al. (2016a) proposed the extended collocation
1035 method, which effectively addresses the ECC of selected pairs. Moreover, the EIVD
1036 method adopts the error cross-correlation framework. In the following section, we
1037 will analyze the ECC between pairs.

1038 **6.2.5.2. Analysis of error cross-correlation**

1039 This study assumes non-zero ECC (Error-Correction Coefficient) conditions exist
1040 between FluxCom and PMLv2 at 0.1° and between ERA5L and GLEAM at 0.25° .
1041 However, non-zero ECC conditions were also possible between other pairs. Therefore,
1042 we presented the EIVD-based ECC results of various pairs.



1043

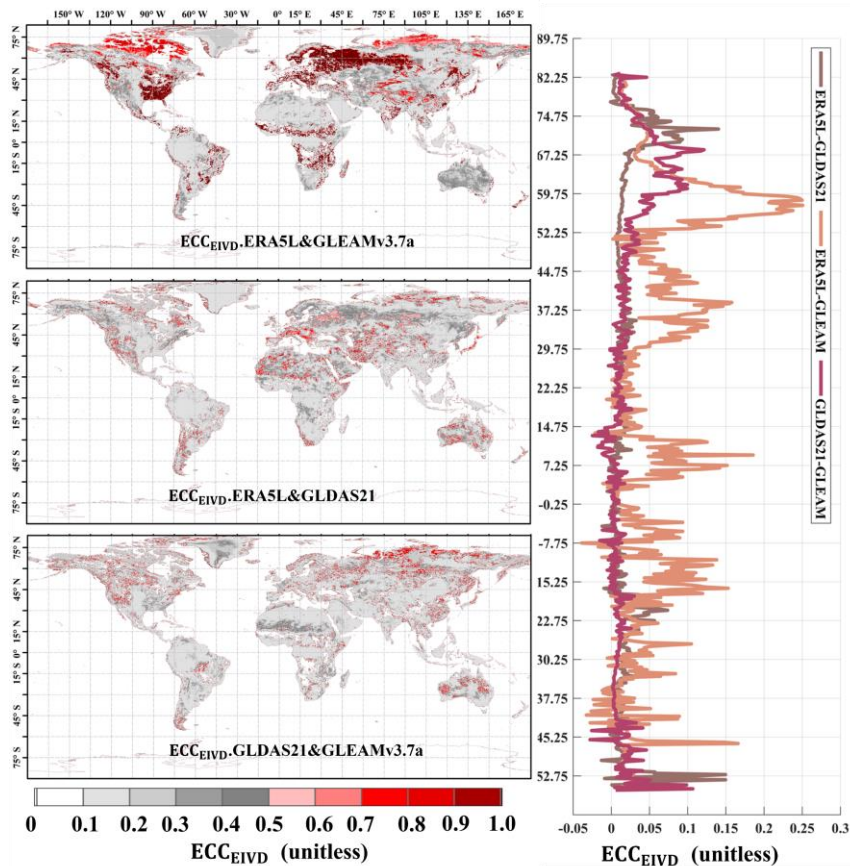
1044

1045

1046

1047

Figure 171311 **FIGURE-11** Global Distribution of estimated error cross-correlation (ECC) between ERA5L, FluxCom, and PMLv2 pairwise using EIVD alongside relevant variation curves of average with latitude.



1048
 1049 **Figure 18** ~~Figure 12~~ Global Distribution of estimated error cross-correlation
 1050 (ECC) between ERA5L, GLEAMv3.7a, and GLDAS21 pairwise using EIVD
 1051 alongside relevant variation curves of average with latitude.
 1052 As depicted in ~~Figure 17~~ ~~Figure 13~~ ~~Figure 12~~ ~~Figure 11~~ and ~~Figure 18~~ ~~Figure~~
 1053 ~~14~~ ~~Figure 13~~ ~~Figure 12~~, at a resolution of 0.1°, the ~~Error to Covariance~~ (ECC) values
 1054 of FluxCom and PMLv2 were notably higher than those of ERA5L-FluxCom and
 1055 ERA5L-PMLv2. The global average ECC value for FluxCom-PMLv2 was 0.16, and
 1056 regions with high ECC values were identified in the eastern United States, most of
 1057 Europe, and the western Amazon, areas densely covered by measurement sites. Since
 1058 both FluxCom and PMLv2 incorporated corrections based on FluxNet measurement

1059 sites, there is likely some overlap between the sites used by both products in the high
1060 ECC regions. This partially explains the shared source of random errors between the
1061 two datasets.

1062 The global error correlations of GLEAM-GLDAS and ERA5L-GLDAS are relatively
1063 low. The random error of ERA5L correlates with that of GLEAM, primarily in arid
1064 regions such as the Sahara Desert, Northwest China, and central Australia, where the
1065 average ECC exceeds 0.20. The global average ECC of ERA5L-GLEAM is
1066 approximately 0.14. A higher error correlation is observed for ERA5L-GLEAM, with
1067 a mean ECC value of 0.26, which is expected since meteorological information from
1068 ECMWF is reanalyzed for both datasets. However, ECC values for GLEAM-GLDAS
1069 and ERA5L-GLDAS are generally low globally, supporting the assumption of zero
1070 ECC for these two pairs.

1071 Our findings highlight the significant impact of Error Cross Correlation (ECC)
1072 between FluxCom-PMLv2 and ERA5L-GLEAM at 0.1° and 0.25° resolutions,
1073 respectively. Mathematically, when a triplet exhibits a high ECC value (>0.3)
1074 between two sets, it indicates a preference for the remaining independent product as
1075 the "better" one, potentially leading to an underestimation of its error variance.
1076 However, it is essential to note that the overall ECC values for other pairs are
1077 relatively small, suggesting that the zero ECC assumptions can be considered valid
1078 for these pairs across most areas. Therefore, these assumptions are unlikely to affect
1079 the relevant results of uncertainties significantly. Nevertheless, we have considered
1080 the non-zero ECC condition between FluxCom-PMLv2 and ERA5L-GLEAM in this
1081 study, as it requires careful consideration.

1082 **6.3.5.3. Comparison of different fusion schemes**

1083 In this section, we conducted comparisons in three aspects: (1) comparing the
1084 performance of CAMELE at different resolutions; (2) comparing the performance of
1085 different change fusion schemes, explicitly changing the input products' versions

1086 (GLDAS21 to GLDAS20 or GLDAS22, GLEAMv3.7a to v3.7b); and (3) comparing
 1087 the performance of the results obtained without considering the ECC impact.

1088 We conducted a comprehensive comparison of our fusion approach with several
 1089 alternative schemes. Specifically, these schemes encompassed utilizing only ERA5L
 1090 and PMLV2 at 0.1° based on the IVD method (Comb1), changing the versions of
 1091 GLDAS2 and GLEAM at 0.25° based on the EIVD method (Comb2-5), and two TC
 1092 fusion approaches at 0.1° and 0.25°, which did not incorporate ECC.

1093 It should be noted that the Comb2 scheme, which includes GLDAS20, covers the
 1094 period from 1980 to 2014, while the other 0.25° comparison schemes (Comb3-5) span
 1095 from 2003 to 2022. We compared the results of three schemes in the fusion process at
 1096 a resolution of 0.25°. The first combination consisted of ERA5L, GLDAS22, and
 1097 GLEAMv3.7a (Comb1). The second input combination consisted of ERA5L,
 1098 GLDAS22, and GLEAMv3.7b (Comb2). The third input combination consisted of
 1099 ERA5L, GLDAS2.1, and GLEAMv3.7b (denoted as Comb3). These three
 1100 combinations used for comparison corresponded to the period from February 2003 to
 1101 December 2022. The combinations based on TC (assuming zero ECC) -assuming zero
 1102 ECC (Zero ECC) had the same inputs as CAMELE at both resolutions.

1103 **Table 765Table 6** Average metrics for CAMELE and other fusion schemes at all
 1104 sites. The bolded sections indicate the schemes with the best performance in their
 1105 respective metrics.

Product	RMSE (mm/d)	ubRMSE (mm/d)	MAE (mm/d)	KGE	R
CAMELE (0.1)	0.83	0.71	0.64	0.5457	0.71
CAMELE (0.25)	1.03	0.87	0.75	0.4951	0.67
<u>ERA5L+PMLV2</u>	<u>1.131.20</u>	<u>1.000.95</u>	<u>0.890.94</u>	<u>0.460.43</u>	<u>0.610.68</u>
<u>(Comb1-0.1 IVD)Comb1</u>					
<u>ERA5L+GLDAS20+GLEAMv3.7a</u>	<u>1.09</u>	<u>0.89</u>	<u>0.87</u>	<u>0.44</u>	<u>0.66</u>
<u>(Comb2-0.25 EIVD)</u>					
<u>ERA5L+GLDAS22+GLEAMv3.7a</u>	<u>1.20</u>	<u>0.95</u>	<u>0.94</u>	<u>0.44</u>	<u>0.68</u>
<u>(Comb3-0.25 EIVD)</u>					
<u>ERA5L+GLDAS22+GLEAMv3.7b</u>	<u>1.191.19</u>	<u>0.940.94</u>	<u>0.930.93</u>	<u>0.440.44</u>	<u>0.690.69</u>
<u>(Comb4-0.25 EIVD)Comb2</u>					
<u>ERA5L+GLDAS21+GLEAMv3.7b</u>	<u>1.051.05</u>	<u>0.900.90</u>	<u>0.800.80</u>	<u>0.490.47</u>	<u>0.690.69</u>
<u>(Comb5-0.25 EIVD)Comb3</u>					

- 格式化表格
- 设置了格式: 字体: 倾斜
- 带格式的: 行距: 单倍行距
- 设置了格式: 字体: 倾斜
- 设置了格式: 字体: 倾斜
- 设置了格式: 字体: 倾斜
- 带格式的: 行距: 单倍行距
- 设置了格式: 字体: 倾斜
- 带格式的: 行距: 单倍行距

<u>ERA5L+FluxCom+PMLv2</u> <u>(Zero-ECC-0.1 / TC)Zero-ECC (0.1)</u>	1.06	0.91	0.80	<u>0.4446</u>	0.60
<u>ERA5L+GLDAS21+GLEAMv3.7a</u> <u>(Zero-ECC-0.25 / TC)Zero-ECC</u> <u>(0.25)</u>	1.26	1.03	0.99	<u>0.3839</u>	0.61

设置了格式: 字体: 倾斜

带格式的: 行距: 单倍行距

设置了格式: 字体: 倾斜

带格式的: 行距: 单倍行距

1106 According to the information in the table, CAMELE (0.1°) results were superior in all
1107 indicators. Firstly, when comparing the performance of CAMELE at resolutions of
1108 0.1° and 0.25°, it was observed that the fused product performed slightly worse at the
1109 0.25° resolution. ~~This could be attributed to the variations in the input products.~~
1110 Additionally, the representative of FluxNet sites at the 0.25° resolution decreased,
1111 leading to degraded statistical indicators.

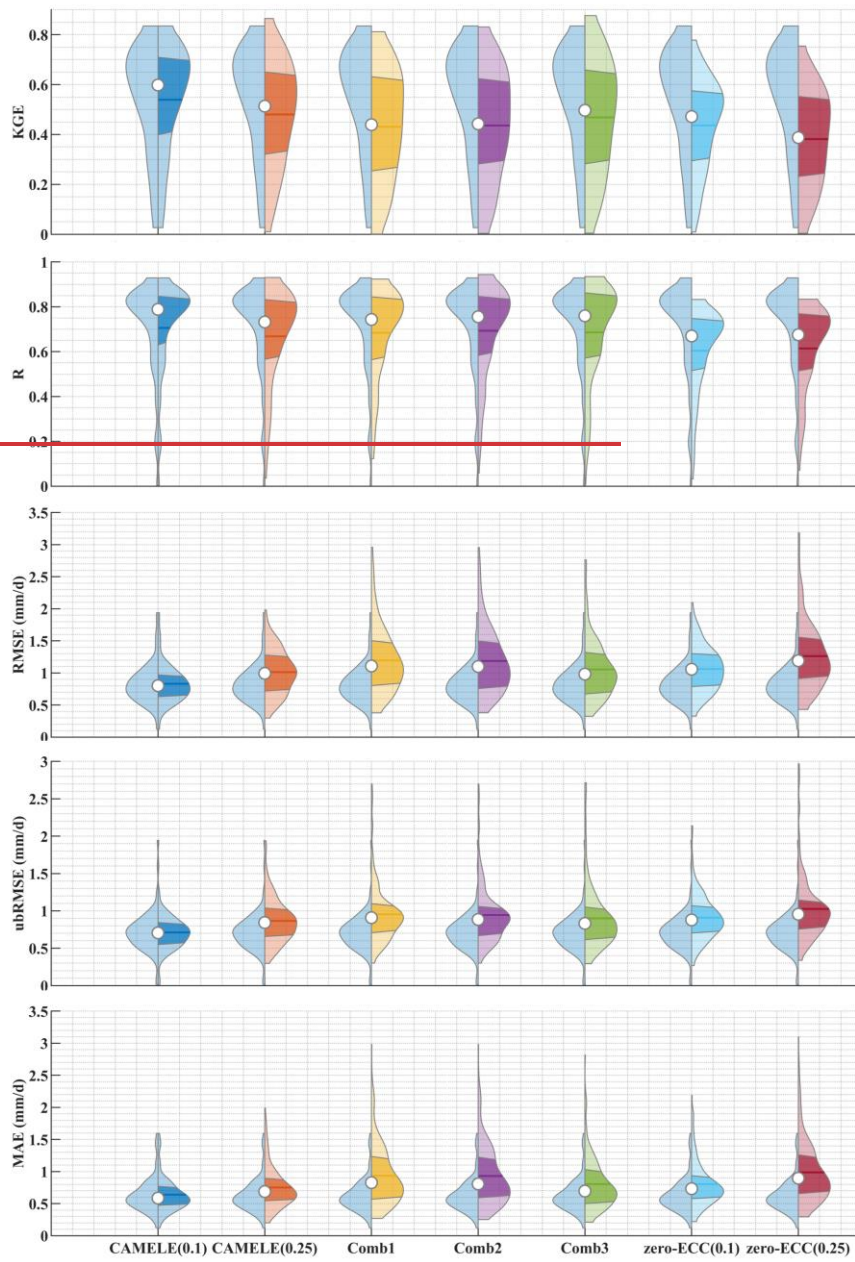
1112 At the 0.1° resolution, we conducted a comparison of results obtained by exclusively
1113 fusing ERA5-Land and PMLv2. Multiple indicators indicated that this approach did
1114 not enhance the accuracy of ET estimates and fell significantly short of the scheme
1115 employed in CAMELE. This implies that using only two product sets as input did not
1116 allow for effective error analysis through collocation analysis, resulting in suboptimal
1117 fusion results. More importantly, the limitation of employing only two datasets
1118 prevented us from effectively acquiring error information through collocation analysis
1119 (Dong et al., 2020a, 2019). Consequently, we made the strategic decision to ensure
1120 the inclusion of three datasets as inputs, facilitating the utilization of the EIVD
1121 method and maintaining methodological consistency between the 0.1° and 0.25°
1122 resolutions.

1123 Furthermore, when comparing the results of different fusion schemes, ~~mainly~~
1124 ~~focusing on the differences~~ between CAMELE and Comb1 to Comb2-53 at the 0.25°
1125 resolution, CAMELE performed better regarding error metrics (RMSE, ubRMSE,
1126 MAE). The differences in fitting metrics (KGE, R) were insignificant, indicating that
1127 the choice of fusion scheme primarily affected the errors of the fusion results. The
1128 relatively poorer performance of other fusion schemes could be due to the lack of
1129 consideration for non-zero ECC. For example, non-zero ECC between GLDAS-2.2
1130 and ERA5L has been reported in a recent study GLEAMv3.7b and GLDAS2.2 (Li et

1131 ~~al., 2023a)employed the satellite data from MODIS, introducing random error~~
1132 ~~homogeneity between the two datasets.~~

1133 For the comparative analysis of the GLDAS2.0 and GLDAS2.1 schemes, the usage of
1134 GLDAS2.1 yielded better performance. The GLDAS-2.1 simulation leverages
1135 conditions from the GLDAS-2.0 simulation, with improved models driven by a
1136 combination of datasets. Previous research has demonstrated that GLDAS-2.1 offers
1137 improvements in the regional-scale simulation of hydrological variables compared to
1138 GLDAS-2.0 (Qi et al., 2018, 2020). Consequently, we chose to incorporate GLDAS-
1139 2.1 data for as much of the time series as possible.

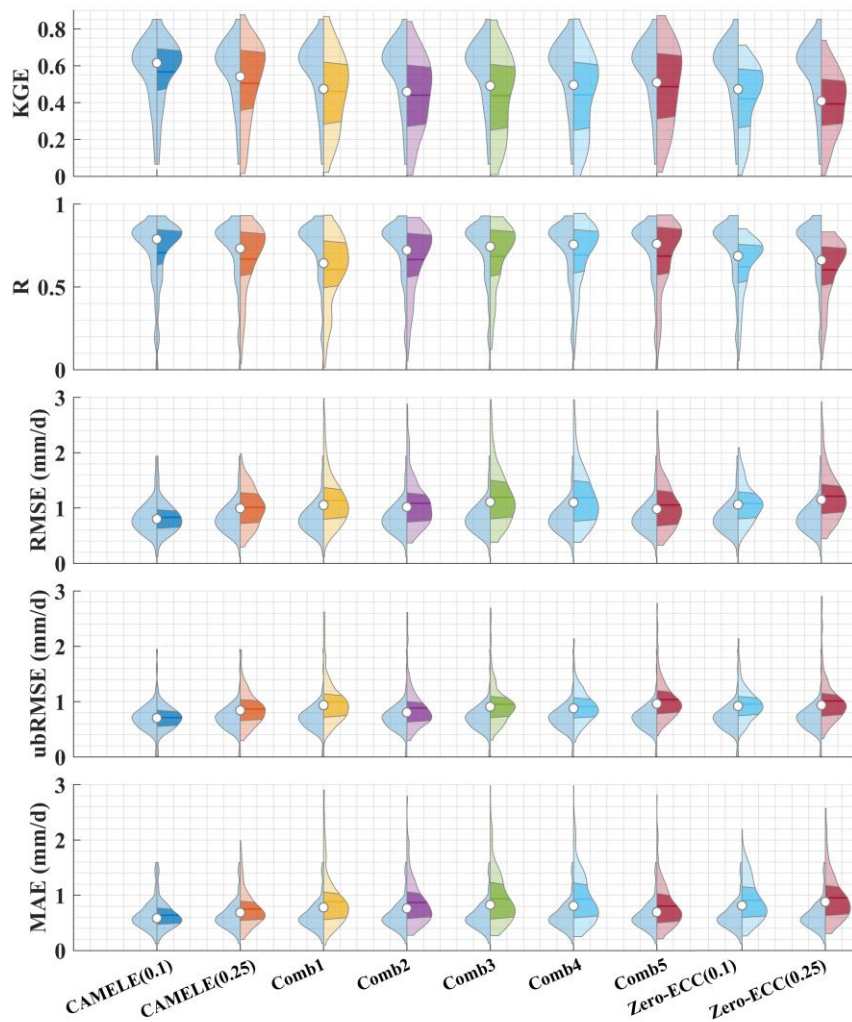
1140 Moreover, when comparing the fusion effects with and without considering non-zero
1141 ECC conditions, it was evident that considering ECC information could effectively
1142 improve the performance of the fused product, which further demonstrated the
1143 reliability and advantages of the fusion method employed in this study.



带格式的: 两端对齐

1|144

1|145



1146

1147 **Figure 191613Figure-13** Violin plot comparing KGE, R, RMSE, ubRMSE and MAE
 1148 of CAMELE with other fusion schemes. The right half of each violin plot represents
 1149 the distribution, with shaded areas indicating the box plot, where the horizontal line
 1150 corresponds to the median and the dot represents the mean. The left half represents
 1151 the results of CAMELE (0.1°) for comparison.

1152 We further provided violin plots for different metrics, comparing the results of each
 1153 fusion scheme to CAMELE (0.1°) as shown in Figure 19Figure-15. The results

1154 indicated that the fusion schemes adopted were significantly superior to other
1155 schemes based on the distribution of results for all metrics across all sites. Regarding
1156 KGE and R, CAMELE's results were concentrated near 1 for most sites. Regarding
1157 RMSE, ubRMSE, and MAE, their results were concentrated below one mm/d. The
1158 results in the plots also suggested that CAMELE performed slightly worse at 0.25°
1159 compared to 0.1° but still outperformed ~~the other~~ combination results ~~of Comb1 to~~
1160 ~~Comb3~~. Additionally, comparing CAMELE and the zero-ECC scheme in the plots
1161 further highlighted the importance of considering non-zero ECC conditions.

1162 **5.4. Potential Applications and Future Enhancements**

1163 In this section, we delve into the potential applications of our product and outline our
1164 commitment to future enhancements to maintain its accuracy and relevance.

1165 Here, we identify three potential applications for our transpiration product: (1) Global
1166 ET Trends: Our product facilitates global-scale analysis of current ET patterns and
1167 long-term trends, essential for comprehending ecosystem responses to evolving
1168 environmental conditions in a warming climate; (2) Transpiration-to-
1169 Evapotranspiration Ratio: Our merging approach can fuse multi-source global gridded
1170 transpiration data, allowing for the examination of the transpiration-to-
1171 evapotranspiration ratio. This analysis can enhance water resource management and
1172 water availability predictions in diverse regions; (3) Attribution analysis: Our product
1173 is a valuable tool for attribution analysis, helping researchers identify the drivers of
1174 patterns. This knowledge is crucial for understanding the roles of climate variability,
1175 land-use changes, and other factors in shaping terrestrial water fluxes.

1176 Furthermore, we are committed to enhancing our product proactively. Key strategies
1177 include: (1) Data Update and Validation: To ensure our product's continued accuracy
1178 and reliability, we will prioritize regularly updating the data used in this study to the
1179 latest versions. By adopting this approach, we aim to provide users with results that
1180 reflect the latest advancements in scientific knowledge; (2) Enhanced Integration and

带格式的: 多级符号 + 级别: 2 + 编号样式: 1, 2, 3, ... + 起
始编号: 1 + 对齐方式: 左侧 + 对齐位置: 0 厘米 + 缩进位
置: 1 厘米

1181 Error Reduction: We continually refine estimates by incorporating additional data
1182 sources and implementing extended collocation method to minimize errors; (3)
1183 Integration of High-Resolution Regional ET Data: Recognizing the significance of
1184 regional-scale insights, we will focus on improving the accuracy of CAMELE by
1185 integrating higher-resolution regional ET data. This integration will enable more
1186 precise regional estimation.
1187 In summary, these endeavors collectively represent our commitment to maintaining
1188 our product's quality and relevance, ensuring its value for the scientific community.

1189 **4.6. Conclusion**

1190 This study used a collocation-based approach for merging data considering non-zero
1191 conditions. We successfully generated a long-term daily CAMELE evapotranspiration
1192 (ET) product at resolutions of 0.1° (2000 to 2020) and 0.25° (1980 to 2022) by
1193 integrating five widely used datasets: ERA5L, FluxCom, PMLv2, GLDAS, and
1194 GLEAM. The key findings of our study are as follows:

- 1195 1. Collocation analysis methods proved to be a reliable tool for evaluating ET
1196 products without a reference dataset. This approach shows promising potential for
1197 error characterization, especially in regions with limited data availability or on a
1198 global scale. The evaluation results provided valuable insights into the data
1199 merging process.
- 1200 2. Compared to five input products, REA, and simple average, the CAMELE product
1201 performed well when evaluated against FluxNet flux tower data. While CAMELE
1202 may not excel in all individual metrics, it effectively reduces errors associated
1203 with the input products. Although it may not have been the best in all metrics, the
1204 overall performance was satisfactory. The result showed Pearson correlation
1205 coefficients (R) of 0.63 and 0.65, root-mean-square errors (RMSE) of 0.81 and
1206 0.73 mm/d, unbiased root-mean-square errors (ubRMSE) of 1.20 and 1.04 mm/d,
1207 mean absolute errors (MAE) of 0.81 and 0.73 mm/d, and Kling-Gupta efficiency

带格式的: 多级符号 + 级别: 1 + 编号样式: 1, 2, 3, ... + 起
始编号: 1 + 对齐方式: 左侧 + 对齐位置: 0 厘米 + 缩进位
置: 0.75 厘米

1208 (KGE) of 0.60 and 0.65 on average over resolutions of 0.1° and 0.25°,
1209 respectively. This robust performance is especially evident when assessing its
1210 comprehensive station-scale evaluation.

1211 3. For different plant functional types (PFTs), the CAMELE product outperformed
1212 the five input products, REA, and simple average in most PFTs. Although
1213 FluxCom and PMLv2 performed slightly better than CAMELE at some PFT sites,
1214 considering that both utilized FluxNet sites for product calibration, it indirectly
1215 demonstrates the ~~excellent~~ promising and robust performance of
1216 CAMELE performance of CAMELE.

1217 4. Based on site-scale observations, CAMELE effectively captures the multi-year
1218 linear trend of ET. The accuracy of the multi-year mean value depicted by
1219 CAMELE is improved compared to the input data. Moreover, it accurately
1220 characterizes extreme ET values. However, there is a slight overestimation in
1221 representing the seasonality, which needs further improvement in future research.

1222 5. When utilizing the error information derived from collocation analysis for
1223 merging, it is crucial to consider the potential presence of non-zero error
1224 compensation conditions (ECC). Comparing the merging schemes with and
1225 without considering non-zero ECC, it was found that considering ECC improves
1226 the accuracy of the merging process. Additionally, when using collocation
1227 analysis, it is necessary to identify which products may have ECC in advance,
1228 providing more effective support for data merging and obtaining more accurate
1229 product error information.

1230 In conclusion, our proposed collocation-based data merging approach demonstrates
1231 the promising potential for merging ET products. The resulting CAMELE product
1232 exhibited good overall performance at site-based and regional scales, meeting the
1233 requirements for more detailed research. Furthermore, further evaluation of the
1234 merged product in specific regions is necessary to improve its accuracy. In future
1235 studies, dynamic weights could be computed by considering suitable merging periods

1236 for different products to enhance the quality of the merged product, and more
1237 sophisticated combination schemes could be explored to improve accuracy.

1238 **Author Contribution**

1239 C.L. conceived and designed the study, collected and analyzed the data, and wrote the
1240 manuscript. H.Y participated in the study design, provided intellectual insights, and
1241 reviewed the manuscript for important intellectual content. Z.L. and W.Y provided
1242 substantial input in the study design and data interpretation and revised the manuscript.
1243 Z.T., J.H., and S.L. guided the research process and critically reviewed the manuscript.
1244 All authors have read and approved the final version of the manuscript.

1245 **Competing interests**

1246 The authors declare that they have no conflict of interest.

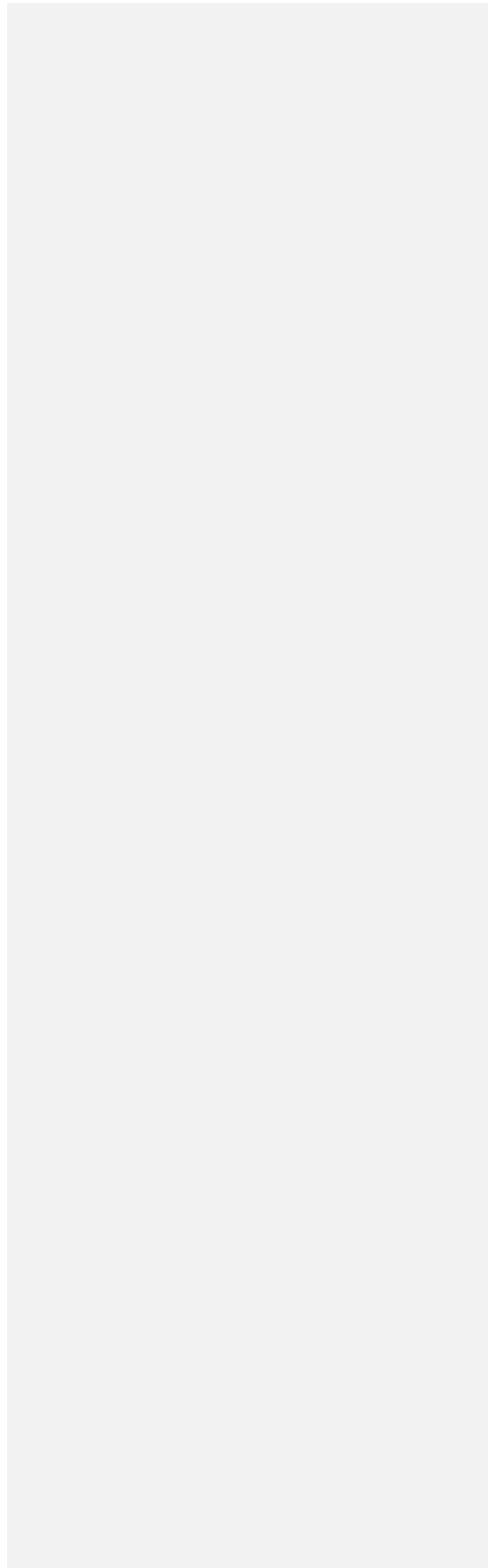
1247 **Acknowledgments**

1248 This research was supported by the China National Key R&D Program (grant no.
1249 2022YFC3002802), the National Natural Science Foundation of China (grant nos.
1250 51979140, [52309022](#) and 42041004), and the Key Research and Development
1251 Program of Yunnan Province, China (grant no. 202203AA080010).

1252 **Data and code availability**

1253 The datasets utilized in this research can be accessed through the links provided in the
1254 Dataset Section. The CAMELE products are available via
1255 <https://doi.org/10.5281/zenodo.5704736> (Li et al., 2023b)(Li et al., 2023a). The data
1256 is distributed under a Creative Commons Attribution 4.0 License. Additionally, we
1257 provide example MATLAB codes to read and plot CAMELE data and employ IVD
1258 and EIVD methods to merge the inputs. Please refer to the latest version., 202306.

域代码已更改



1261 **Reference**

- 1262 Baker, J. C. A., Garcia-Carreras, L., Gloor, M., Marsham, J. H., Buermann, W., da
1263 Rocha, H. R., Nobre, A. D., de Araujo, A. C., and Spracklen, D. V.:
1264 Evapotranspiration in the Amazon: spatial patterns, seasonality, and recent trends in
1265 observations, reanalysis, and climate models, *Hydrology and Earth System Sciences*,
1266 25, 2279–2300, <https://doi.org/10.5194/hess-25-2279-2021>, 2021.
- 1267 Barraza Bernadas, V., Grings, F., Restrepo-Coupe, N., and Huete, A.: Comparison of
1268 the performance of latent heat flux products over southern hemisphere forest
1269 ecosystems: estimating latent heat flux error structure using in situ measurements and
1270 the triple collocation method, *International Journal of Remote Sensing*, 39, 6300–
1271 6315, 2018.
- 1272 Bates, J. M. and Granger, C. W.: The combination of forecasts, *Journal of the*
1273 *Operational Research Society*, 20, 451–468, 1969.
- 1274 Chen, Z., Zhu, Z., Jiang, H., and Sun, S.: Estimating daily reference
1275 evapotranspiration based on limited meteorological data using deep learning and
1276 classical machine learning methods, *Journal of Hydrology*, 591,
1277 <https://doi.org/10.1016/j.jhydrol.2020.125286>, 2020.
- 1278 De Lannoy, G. J., Houser, P. R., Verhoest, N. E., Pauwels, V. R., and Gish, T. J.:
1279 Upscaling of point soil moisture measurements to field averages at the OPE3 test site,
1280 *Journal of Hydrology*, 343, 1–11, 2007.
- 1281 Deng, X., Zhu, L., Wang, H., Zhang, X., Tong, C., Li, S., and Wang, K.: Triple
1282 Collocation Analysis and In Situ Validation of the CYGNSS Soil Moisture Product,
1283 *IEEE Journal of Selected Topics in Applied Earth Observations and Remote Sensing*,
1284 16, 1883–1899, <https://doi.org/10.1109/jstars.2023.3235111>, 2023.
- 1285 Dong, J. and Crow, W. T.: An Improved Triple Collocation Analysis Algorithm for
1286 Decomposing Autocorrelated and White Soil Moisture Retrieval Errors, *Journal of*
1287 *Geophysical Research: Atmospheres*, 122, 13,081–13,094,
1288 <https://doi.org/10.1002/2017jd027387>, 2017.
- 1289 Dong, J., Crow, W. T., Duan, Z., Wei, L., and Lu, Y.: A double instrumental variable
1290 method for geophysical product error estimation, *Remote Sensing of Environment*,
1291 225, 217–228, <https://doi.org/10.1016/j.rse.2019.03.003>, 2019.
- 1292 Dong, J., Wei, L., Chen, X., Duan, Z., and Lu, Y.: An instrument variable based
1293 algorithm for estimating cross-correlated hydrological remote sensing errors, *Journal*
1294 *of Hydrology*, 581, 124413, <https://doi.org/10.1016/j.jhydrol.2019.124413>, 2020a.
- 1295 Dong, J., Lei, F., and Wei, L.: Triple Collocation Based Multi-Source Precipitation
1296 Merging, *Frontiers in Water*, 2, <https://doi.org/10.3389/frwa.2020.00001>, 2020b.
- 1297 Dong, J., Crow, W. T., Chen, X., Tangdamrongsub, N., Gao, M., Sun, S., Qiu, J., Wei,

1298 L., Gao, H., and Duan, Z.: Statistical uncertainty analysis-based precipitation merging
1299 (SUPER): A new framework for improved global precipitation estimation, *Remote*
1300 *Sensing of Environment*, 283, 113299, <https://doi.org/10.1016/j.rse.2022.113299>,
1301 2022.

1302 Draper, C., Reichle, R., de Jeu, R., Naeimi, V., Parinussa, R., and Wagner, W.:
1303 Estimating root mean square errors in remotely sensed soil moisture over continental
1304 scale domains, *Remote Sensing of Environment*, 137, 288–298, 2013.

1305 Duan, Z., Duggan, E., Chen, C., Gao, H., Dong, J., and Liu, J.: Comparison of
1306 traditional method and triple collocation analysis for evaluation of multiple gridded
1307 precipitation products across Germany, *Journal of Hydrometeorology*,
1308 <https://doi.org/10.1175/JHM-D-21-0049.1>, 2021.

1309 ECMWF, S. P.: In IFS documentation CY40R1 Part IV: Physical Processes, ECMWF:
1310 Reading, UK, 111–113, 2014.

1311 Ershadi, A., McCabe, M. F., Evans, J. P., Chaney, N. W., and Wood, E. F.: Multi-site
1312 evaluation of terrestrial evaporation models using FLUXNET data, *Agricultural and*
1313 *Forest Meteorology*, 187, 46–61, <https://doi.org/10.1016/j.agrformet.2013.11.008>,
1314 2014.

1315 Feng, Y., Cui, N., Zhao, L., Hu, X., and Gong, D.: Comparison of ELM, GANN,
1316 WNN and empirical models for estimating reference evapotranspiration in humid
1317 region of Southwest China, *Journal of Hydrology*, 536, 376–383,
1318 <https://doi.org/10.1016/j.jhydrol.2016.02.053>, 2016.

1319 Gan, R., Zhang, Y., Shi, H., Yang, Y., Eamus, D., Cheng, L., Chiew, F. H., and Yu,
1320 Q.: Use of satellite leaf area index estimating evapotranspiration and gross
1321 assimilation for Australian ecosystems, *Ecohydrology*, 11, e1974, 2018.

1322 Gentine, P., Massmann, A., Lintner, B. R., Hamed Alemohammad, S., Fu, R., Green,
1323 J. K., Kennedy, D., and Vilà-Guerau de Arellano, J.: Land–atmosphere interactions in
1324 the tropics – a review, *Hydrology and Earth System Sciences*, 23, 4171–4197,
1325 <https://doi.org/10.5194/hess-23-4171-2019>, 2019.

1326 Gruber, A., Su, C., Crow, W. T., Zwieback, S., Dorigo, W., and Wagner, W.:
1327 Estimating error cross-correlations in soil moisture data sets using extended
1328 collocation analysis, *Journal of Geophysical Research: Atmospheres*, 121, 1208–1219,
1329 2016a.

1330 Gruber, A., Su, C.-H., Zwieback, S., Crow, W., Dorigo, W., and Wagner, W.: Recent
1331 advances in (soil moisture) triple collocation analysis, *International Journal of*
1332 *Applied Earth Observation and Geoinformation*, 45, 200–211,
1333 <https://doi.org/10.1016/j.jag.2015.09.002>, 2016b.

1334 Gruber, A., Dorigo, W. A., Crow, W., and Wagner, W.: Triple Collocation-Based
1335 Merging of Satellite Soil Moisture Retrievals, *IEEE Trans. Geosci. Remote Sensing*,
1336 55, 6780–6792, <https://doi.org/10.1109/TGRS.2017.2734070>, 2017.

1337 Gruber, A., Scanlon, T., van der Schalie, R., Wagner, W., and Dorigo, W.: Evolution
1338 of the ESA CCI Soil Moisture climate data records and their underlying merging
1339 methodology, *Earth System Science Data*, 11, 717–739, <https://doi.org/10.5194/essd->

1340 11-717-2019, 2019.

1341 Gruber, A., De Lannoy, G., Albergel, C., Al-Yaari, A., Brocca, L., Calvet, J. C.,
1342 Colliander, A., Cosh, M., Crow, W., Dorigo, W., Draper, C., Hirschi, M., Kerr, Y.,
1343 Konings, A., Lahoz, W., McColl, K., Montzka, C., Muñoz-Sabater, J., Peng, J.,
1344 Reichle, R., Richaume, P., Rüdiger, C., Scanlon, T., van der Schalie, R., Wigneron, J.
1345 P., and Wagner, W.: Validation practices for satellite soil moisture retrievals: What
1346 are (the) errors?, *Remote Sensing of Environment*, 244, 111806,
1347 <https://doi.org/10.1016/j.rse.2020.111806>, 2020.

1348 Gupta, H. V., Kling, H., Yilmaz, K. K., and Martinez, G. F.: Decomposition of the
1349 mean squared error and NSE performance criteria: Implications for improving
1350 hydrological modelling, *Journal of hydrology*, 377, 80–91, 2009.

1351 Han, S. and Tian, F.: A review of the complementary principle of evaporation: from
1352 the original linear relationship to generalized nonlinear functions, *Hydrology and
1353 Earth System Sciences*, 24, 2269–2285, <https://doi.org/10.5194/hess-24-2269-2020>,
1354 2020.

1355 Hao, Y., Baik, J., and Choi, M.: Combining generalized complementary relationship
1356 models with the Bayesian Model Averaging method to estimate actual
1357 evapotranspiration over China, *Agricultural and Forest Meteorology*, 279, 107759,
1358 <https://doi.org/10.1016/j.agrformet.2019.107759>, 2019.

1359 Hersbach, H., Bell, B., Berrisford, P., Hirahara, S., Horányi, A., Muñoz-Sabater, J.,
1360 Nicolas, J., Peubey, C., Radu, R., Schepers, D., Simmons, A., Soci, C., Abdalla, S.,
1361 Abellan, X., Balsamo, G., Bechtold, P., Biavati, G., Bidlot, J., Bonavita, M., Chiara,
1362 G., Dahlgren, P., Dee, D., Diamantakis, M., Dragani, R., Flemming, J., Forbes, R.,
1363 Fuentes, M., Geer, A., Haimberger, L., Healy, S., Hogan, R. J., Hólm, E., Janisková,
1364 M., Keeley, S., Lalouaux, P., Lopez, P., Lupu, C., Radnoti, G., Rosnay, P., Rozum, I.,
1365 Vamborg, F., Villaume, S., and Thépaut, J.: The ERA5 global reanalysis, *Quarterly
1366 Journal of the Royal Meteorological Society*, 146, 1999–2049,
1367 <https://doi.org/10.1002/qj.3803>, 2020.

1368 Hoareau, N., Portabella, M., Lin, W., Ballabrera-Poy, J., and Turiel, A.: Error
1369 characterization of sea surface salinity products using triple collocation analysis,
1370 *IEEE Transactions on Geoscience and Remote Sensing*, 56, 5160–5168, 2018.

1371 Jia, Y., Li, C., Yang, H., Yang, W., and Liu, Z.: Assessments of three
1372 evapotranspiration products over China using extended triple collocation and water
1373 balance methods, *Journal of Hydrology*, 614, 128594, 2022.

1374 Jiang, C. and Ryu, Y.: Multi-scale evaluation of global gross primary productivity and
1375 evapotranspiration products derived from Breathing Earth System Simulator (BESS),
1376 *Remote Sensing of Environment*, 186, 528–547, 2016.

1377 Jiang, C., Ryu, Y., Fang, H., Myneni, R., Claverie, M., and Zhu, Z.: Inconsistencies of
1378 interannual variability and trends in long-term satellite leaf area index products, *Glob
1379 Chang Biol*, 23, 4133–4146, <https://doi.org/10.1111/gcb.13787>, 2017.

1380 Jiang, C., Guan, K., Pan, M., Ryu, Y., Peng, B., and Wang, S.: BESS-STAIR: a
1381 framework to estimate daily, 30 m, and all-weather crop evapotranspiration using

1382 multi-source satellite data for the US Corn Belt, *Hydrology and Earth System*
1383 *Sciences*, 24, 1251–1273, <https://doi.org/10.5194/hess-24-1251-2020>, 2020.

1384 Jiménez, C., Prigent, C., Mueller, B., Seneviratne, S. I., McCabe, M. F., Wood, E. F.,
1385 Rossow, W. B., Balsamo, G., Betts, A. K., Dirmeyer, P. A., Fisher, J. B., Jung, M.,
1386 Kanamitsu, M., Reichle, R. H., Reichstein, M., Rodell, M., Sheffield, J., Tu, K., and
1387 Wang, K.: Global intercomparison of 12 land surface heat flux estimates, *J. Geophys.*
1388 *Res.*, 116, D02102, <https://doi.org/10.1029/2010JD014545>, 2011.

1389 Jung, M., Koirala, S., Weber, U., Ichii, K., Gans, F., Camps-Valls, G., Papale, D.,
1390 Schwalm, C., Tramontana, G., and Reichstein, M.: The FLUXCOM ensemble of
1391 global land-atmosphere energy fluxes, *Sci Data*, 6, 74,
1392 <https://doi.org/10.1038/s41597-019-0076-8>, 2019.

1393 Khan, M. S., Liaqat, U. W., Baik, J., and Choi, M.: Stand-alone uncertainty
1394 characterization of GLEAM, GLDAS and MOD16 evapotranspiration products using
1395 an extended triple collocation approach, *Agricultural and Forest Meteorology*, 252,
1396 256–268, <https://doi.org/10.1016/j.agrformet.2018.01.022>, 2018.

1397 Kim, S., Pham, H. T., Liu, Y. Y., Marshall, L., and Sharma, A.: Improving the
1398 Combination of Satellite Soil Moisture Data Sets by Considering Error Cross
1399 Correlation: A Comparison Between Triple Collocation (TC) and Extended Double
1400 Instrumental Variable (EIVD) Alternatives, *IEEE Transactions on Geoscience and*
1401 *Remote Sensing*, 59, 7285–7295, <https://doi.org/10.1109/tgrs.2020.3032418>, 2021a.

1402 Kim, S., Sharma, A., Liu, Y. Y., and Young, S. I.: Rethinking satellite data merging:
1403 from averaging to SNR optimization, *IEEE Transactions on Geoscience and Remote*
1404 *Sensing*, 60, 1–15, 2021b.

1405 Kling, H., Fuchs, M., and Paulin, M.: Runoff conditions in the upper Danube basin
1406 under an ensemble of climate change scenarios, *Journal of Hydrology*, 424–425, 264–
1407 277, <https://doi.org/10.1016/j.jhydrol.2012.01.011>, 2012.

1408 Knoben, W. J. M., Freer, J. E., and Woods, R. A.: Technical note: Inherent
1409 benchmark or not? Comparing Nash–Sutcliffe and Kling–Gupta efficiency scores,
1410 *Hydrology and Earth System Sciences*, 23, 4323–4331, [https://doi.org/10.5194/hess-](https://doi.org/10.5194/hess-23-4323-2019)
1411 [23-4323-2019](https://doi.org/10.5194/hess-23-4323-2019), 2019.

1412 Koster, R. D., Liu, Q., Reichle, R. H., and Huffman, G. J.: Improved Estimates of
1413 Pentad Precipitation Through the Merging of Independent Precipitation Data Sets,
1414 *Water Resources Research*, 57, <https://doi.org/10.1029/2021wr030330>, 2021.

1415 Leuning, R., Zhang, Y., Rajaud, A., Cleugh, H., and Tu, K.: A simple surface
1416 conductance model to estimate regional evaporation using MODIS leaf area index and
1417 the Penman-Monteith equation, *Water Resources Research*, 44, 2008.

1418 Leuning, R., Zhang, Y. Q., Rajaud, A., Cleugh, H., and Tu, K.: Correction to “A
1419 simple surface conductance model to estimate regional evaporation using MODIS leaf
1420 area index and the Penman-Monteith equation,” *Water Resources Research*, 45,
1421 <https://doi.org/10.1029/2008wr007631>, 2009.

1422 Li, B., Rodell, M., Kumar, S., Beaudoin, H. K., Getirana, A., Zaitchik, B. F.,
1423 Goncalves, L. G., Cossetin, C., Bhanja, S., Mukherjee, A., Tian, S., Tangdamrongsub,

1424 N., Long, D., Nanteza, J., Lee, J., Policelli, F., Goni, I. B., Daira, D., Bila, M., Lannoy,
1425 G., Mocko, D., Steele-Dunne, S. C., Save, H., and Bettadpur, S.: Global GRACE Data
1426 Assimilation for Groundwater and Drought Monitoring: Advances and Challenges,
1427 *Water Resour. Res.*, 55, 7564–7586, <https://doi.org/10.1029/2018WR024618>, 2019a.

1428 Li, C., Tang, G., and Hong, Y.: Cross-evaluation of ground-based, multi-satellite and
1429 reanalysis precipitation products: Applicability of the Triple Collocation method
1430 across Mainland China, *Journal of Hydrology*, 562, 71–83,
1431 <https://doi.org/10.1016/j.jhydrol.2018.04.039>, 2018.

1432 Li, C., Yang, H., Yang, W., Liu, Z., Jia, Y., Li, S., and Yang, D.: Error
1433 Characterization of Global Land Evapotranspiration Products: Collocation-based
1434 approach, *Journal of Hydrology*, 128102, 2022.

1435 Li, C., Liu, Z., Tu, Z., Shen, J., He, Y., and Yang, H.: Assessment of global gridded
1436 transpiration products using the extended instrumental variable technique (EIVD),
1437 *Journal of Hydrology*, 623, 129880, <https://doi.org/10.1016/j.jhydrol.2023.129880>,
1438 2023a.

1439 Li, C., Liu, Z., Yang, W., Tu, Z., Han, J., Sien, L., and Hanbo, Y.: CAMELE:
1440 Collocation-Analyzed Multi-source Ensembled Land Evapotranspiration Data, ,
1441 <https://doi.org/10.5281/zenodo.8047038>, 2023b.

1442 Li, X., Gentine, P., Lin, C., Zhou, S., Sun, Z., Zheng, Y., Liu, J., and Zheng, C.: A
1443 simple and objective method to partition evapotranspiration into transpiration and
1444 evaporation at eddy-covariance sites, *Agricultural and Forest Meteorology*, 265, 171–
1445 182, <https://doi.org/10.1016/j.agrformet.2018.11.017>, 2019b.

1446 Li, X., Zhang, W., Vermeulen, A., Dong, J., and Duan, Z.: Triple collocation-based
1447 merging of multi-source gridded evapotranspiration data in the Nordic Region,
1448 *Agricultural and Forest Meteorology*, 335, 109451,
1449 <https://doi.org/10.1016/j.agrformet.2023.109451>, 2023c.

1450 Lian, X., Piao, S., Huntingford, C., Li, Y., Zeng, Z., Wang, X., Ciais, P., McVicar, T.
1451 R., Peng, S., Ottlé, C., Yang, H., Yang, Y., Zhang, Y., and Wang, T.: Partitioning
1452 global land evapotranspiration using CMIP5 models constrained by observations,
1453 *Nature Clim Change*, 8, 640–646, <https://doi.org/10.1038/s41558-018-0207-9>, 2018.

1454 Lin, C., Gentine, P., Huang, Y., Guan, K., Kimm, H., and Zhou, S.: Diel ecosystem
1455 conductance response to vapor pressure deficit is suboptimal and independent of soil
1456 moisture, *Agricultural and Forest Meteorology*, 250, 24–34, 2018.

1457 Loveland, T. R., Zhu, Z., Ohlen, D. O., Brown, J. F., Reed, B. C., and Yang, L.: An
1458 analysis of the IGBP global land-cover characterization process, *Photogrammetric
1459 engineering and remote sensing*, 65, 1021–1032, 1999.

1460 Lu, J., Wang, G., Chen, T., Li, S., Hagan, D. F. T., Kattel, G., Peng, J., Jiang, T., and
1461 Su, B.: A harmonized global land evaporation dataset from model-based products
1462 covering 1980–2017, *Earth System Science Data*, 13, 5879–5898,
1463 <https://doi.org/10.5194/essd-13-5879-2021>, 2021.

1464 Ma, N., Szilagyi, J., and Jozsa, J.: Benchmarking large-scale evapotranspiration
1465 estimates: A perspective from a calibration-free complementary relationship approach

1466 and FLUXCOM, *Journal of Hydrology*, 590,
1467 <https://doi.org/10.1016/j.jhydrol.2020.125221>, 2020.
1468 Majozi, N. P., Mannaerts, C. M., Ramoelo, A., Mathieu, R., Nickless, A., and Verhoef,
1469 W.: Analysing surface energy balance closure and partitioning over a semi-arid
1470 savanna FLUXNET site in Skukuza, Kruger National Park, South Africa, *Hydrology
1471 and Earth System Sciences*, 21, 3401–3415, [https://doi.org/10.5194/hess-21-3401-
1472 2017](https://doi.org/10.5194/hess-21-3401-2017), 2017.
1473 Martens, B., Miralles, D. G., Lievens, H., van der Schalie, R., de Jeu, R. A. M.,
1474 Fernández-Prieto, D., Beck, H. E., Dorigo, W. A., and Verhoest, N. E. C.:
1475 GLEAM v3: satellite-based land evaporation and root-zone soil moisture,
1476 *Geoscientific Model Development*, 10, 1903–1925, [https://doi.org/10.5194/gmd-10-
1477 1903-2017](https://doi.org/10.5194/gmd-10-1903-2017), 2017.
1478 McColl, K. A., Vogelzang, J., Konings, A. G., Entekhabi, D., Piles, M., and Stoffelen,
1479 A.: Extended triple collocation: Estimating errors and correlation coefficients with
1480 respect to an unknown target, *Geophysical Research Letters*, 41, 6229–6236,
1481 <https://doi.org/10.1002/2014gl061322>, 2014.
1482 Ming, W., Ji, X., Zhang, M., Li, Y., Liu, C., Wang, Y., and Li, J.: A Hybrid Triple
1483 Collocation-Deep Learning Approach for Improving Soil Moisture Estimation from
1484 Satellite and Model-Based Data, *Remote Sensing*, 14,
1485 <https://doi.org/10.3390/rs14071744>, 2022.
1486 Miralles, D., De Jeu, R., Gash, J., Holmes, T., and Dolman, A.: Magnitude and
1487 variability of land evaporation and its components at the global scale, *Hydrology and
1488 Earth System Sciences*, 15, 967–981, 2011.
1489 Miralles, D. G., Gentine, P., Seneviratne, S. I., and Teuling, A. J.: Land-atmospheric
1490 feedbacks during droughts and heatwaves: state of the science and current challenges,
1491 *Ann N Y Acad Sci*, 1436, 19–35, <https://doi.org/10.1111/nyas.13912>, 2019.
1492 Mu, Q., Zhao, M., and Running, S. W.: Improvements to a MODIS global terrestrial
1493 evapotranspiration algorithm, *Remote sensing of environment*, 115, 1781–1800, 2011.
1494 Muñoz-Sabater, J., Dutra, E., Agustí-Panareda, A., Albergel, C., Arduini, G., Balsamo,
1495 G., Boussetta, S., Choulga, M., Harrigan, S., Hersbach, H., Martens, B., Miralles, D.
1496 G., Piles, M., Rodríguez-Fernández, N. J., Zsoter, E., Buontempo, C., and Thépaut, J.-
1497 N.: ERA5-Land: a state-of-the-art global reanalysis dataset for land applications,
1498 *Earth Syst. Sci. Data*, 13, 4349–4383, <https://doi.org/10.5194/essd-13-4349-2021>,
1499 2021.
1500 Pan, S., Pan, N., Tian, H., Friedlingstein, P., Sitch, S., Shi, H., Arora, V. K., Haverd,
1501 V., Jain, A. K., Kato, E., Lienert, S., Lombardozzi, D., Nabel, J. E. M. S., Ottlé, C.,
1502 Poulter, B., Zaehle, S., and Running, S. W.: Evaluation of global terrestrial
1503 evapotranspiration using state-of-the-art approaches in remote sensing, machine
1504 learning and land surface modeling, *Hydrology and Earth System Sciences*, 24, 1485–
1505 1509, <https://doi.org/10.5194/hess-24-1485-2020>, 2020.
1506 Park, J., Baik, J., and Choi, M.: Triple collocation-based multi-source evaporation and
1507 transpiration merging, *Agricultural and Forest Meteorology*, 331, 109353, 2023.

1508 Pastorello, G., Trotta, C., Canfora, E., Chu, H., Christianson, D., Cheah, Y. W.,
 1509 Poindexter, C., Chen, J., Elbashandy, A., Humphrey, M., Isaac, P., Polidori, D.,
 1510 Reichstein, M., Ribeca, A., van Ingen, C., Vuichard, N., Zhang, L., Amiro, B.,
 1511 Ammann, C., Arain, M. A., Ardo, J., Arkebauer, T., Arndt, S. K., Arriga, N., Aubinet,
 1512 M., Aurela, M., Baldocchi, D., Barr, A., Beamesderfer, E., Marchesini, L. B.,
 1513 Bergeron, O., Beringer, J., Bernhofer, C., Berveiller, D., Billesbach, D., Black, T. A.,
 1514 Blanken, P. D., Bohrer, G., Boike, J., Bolstad, P. V., Bonal, D., Bonnefond, J. M.,
 1515 Bowling, D. R., Bracho, R., Brodeur, J., Brummer, C., Buchmann, N., Burban, B.,
 1516 Burns, S. P., Buysse, P., Cale, P., Cavagna, M., Cellier, P., Chen, S., Chini, I.,
 1517 Christensen, T. R., Cleverly, J., Collalti, A., Consalvo, C., Cook, B. D., Cook, D.,
 1518 Coursolle, C., Cremonese, E., Curtis, P. S., D'Andrea, E., da Rocha, H., Dai, X.,
 1519 Davis, K. J., Cinti, B., Grandcourt, A., Ligne, A., De Oliveira, R. C., Delpierre, N.,
 1520 Desai, A. R., Di Bella, C. M., Tommasi, P. D., Dolman, H., Domingo, F., Dong, G.,
 1521 Dore, S., Duce, P., Dufrene, E., Dunn, A., Dusek, J., Eamus, D., Eichelmann, U.,
 1522 ElKhidir, H. A. M., Eugster, W., Ewenz, C. M., Ewers, B., Famulari, D., Fares, S.,
 1523 Feigenwinter, I., Feitz, A., Fensholt, R., Filippa, G., Fischer, M., Frank, J., Galvagno,
 1524 M., et al.: The FLUXNET2015 dataset and the ONEFlux processing pipeline for eddy
 1525 covariance data, *Sci Data*, 7, 225, <https://doi.org/10.1038/s41597-020-0534-3>, 2020.
 1526 Priestley, C. H. B. and TAYLOR, R. J.: On the assessment of surface heat flux and
 1527 evaporation using large-scale parameters, *Monthly weather review*, 100, 81–92, 1972.
 1528 Qi, W., Liu, J., and Chen, D.: Evaluations and Improvements of GLDAS2.0 and
 1529 GLDAS2.1 Forcing Data's Applicability for Basin Scale Hydrological Simulations in
 1530 the Tibetan Plateau, *JGR Atmospheres*, 123, <https://doi.org/10.1029/2018JD029116>,
 1531 2018.
 1532 Qi, W., Liu, J., Yang, H., Zhu, X., Tian, Y., Jiang, X., Huang, X., and Feng, L.: Large
 1533 Uncertainties in Runoff Estimations of GLDAS Versions 2.0 and 2.1 in China, *Earth
 1534 and Space Science*, 7, e2019EA000829, <https://doi.org/10.1029/2019EA000829>, 2020.
 1535 Restrepo-Coupe, N., Albert, L. P., Longo, M., Baker, I., Levine, N. M., Mercado, L.
 1536 M., da Araujo, A. C., Christoffersen, B. O., Costa, M. H., Fitzjarrald, D. R., Galbraith,
 1537 D., Imbuzeiro, H., Malhi, Y., von Randow, C., Zeng, X., Moorcroft, P., and Saleska,
 1538 S. R.: Understanding water and energy fluxes in the Amazonia: Lessons from an
 1539 observation-model intercomparison, *Glob Chang Biol*, 27, 1802–1819,
 1540 <https://doi.org/10.1111/gcb.15555>, 2021.
 1541 Ribal, A. and Young, I. R.: Global Calibration and Error Estimation of Altimeter,
 1542 Scatterometer, and Radiometer Wind Speed Using Triple Collocation, *Remote
 1543 Sensing*, 12, <https://doi.org/10.3390/rs12121997>, 2020.
 1544 Rodell, M., Houser, P., Jambor, U., Gottschalck, J., Mitchell, K., Meng, C.-J.,
 1545 Arsenault, K., Cosgrove, B., Radakovich, J., and Bosilovich, M.: The global land data
 1546 assimilation system, *Bulletin of the American Meteorological society*, 85, 381–394,
 1547 2004.
 1548 Sheffield, J., Goteti, G., and Wood, E. F.: Development of a 50-Year High-Resolution
 1549 Global Dataset of Meteorological Forcings for Land Surface Modeling, *Journal of*

1550 Climate, 19, 3088–3111, <https://doi.org/10.1175/JCLI3790.1>, 2006.

1551 Stoffelen, A.: Toward the true near-surface wind speed: Error modeling and
1552 calibration using triple collocation, *Journal of Geophysical Research: Oceans*, 103,
1553 7755–7766, <https://doi.org/10.1029/97jc03180>, 1998.

1554 Su, C.-H. and Ryu, D.: Multi-scale analysis of bias correction of soil moisture,
1555 *Hydrology and Earth System Sciences*, 19, 17–31, 2015.

1556 Su, C.-H., Ryu, D., Crow, W. T., and Western, A. W.: Beyond triple collocation:
1557 Applications to soil moisture monitoring, *Journal of Geophysical Research:*
1558 *Atmospheres*, 119, 6419–6439, <https://doi.org/10.1002/2013jd021043>, 2014.

1559 Sun, J., McColl, K. A., Wang, Y., Rigden, A. J., Lu, H., Yang, K., Li, Y., and
1560 Santanello, J. A.: Global evaluation of terrestrial near-surface air temperature and
1561 specific humidity retrievals from the Atmospheric Infrared Sounder (AIRS), *Remote*
1562 *Sensing of Environment*, 252, <https://doi.org/10.1016/j.rse.2020.112146>, 2021.

1563 Towner, J., Cloke, H. L., Zsoter, E., Flamig, Z., Hoch, J. M., Bazo, J., Coughlan de
1564 Perez, E., and Stephens, E. M.: Assessing the performance of global hydrological
1565 models for capturing peak river flows in the Amazon basin, *Hydrology and Earth*
1566 *System Sciences*, 23, 3057–3080, <https://doi.org/10.5194/hess-23-3057-2019>, 2019.

1567 Tsamalis, C.: Clarifications on the equations and the sample number in triple
1568 collocation analysis using SST observations, *Remote Sensing of Environment*, 272,
1569 <https://doi.org/10.1016/j.rse.2022.112936>, 2022.

1570 Twine, T. E., Kustas, W., Norman, J., Cook, D., Houser, Pr., Meyers, T., Prueger, J.,
1571 Starks, P., and Wesely, M.: Correcting eddy-covariance flux underestimates over a
1572 grassland, *Agricultural and forest meteorology*, 103, 279–300, 2000.

1573 Vogelzang, J., Stoffelen, A., and Verhoef, A.: The Effect of Error Non-Orthogonality
1574 on Triple Collocation Analyses, *Remote Sensing*, 14, 4268, 2022.

1575 Wu, K., Ryu, D., Nie, L., and Shu, H.: Time-variant error characterization of SMAP
1576 and ASCAT soil moisture using Triple Collocation Analysis, *Remote Sensing of*
1577 *Environment*, 256, <https://doi.org/10.1016/j.rse.2021.112324>, 2021.

1578 Yang, Y., Roderick, M. L., Guo, H., Miralles, D. G., Zhang, L., Fatichi, S., Luo, X.,
1579 Zhang, Y., McVicar, T. R., Tu, Z., Keenan, T. F., Fisher, J. B., Gan, R., Zhang, X.,
1580 Piao, S., Zhang, B., and Yang, D.: Evapotranspiration on a greening Earth, *Nat Rev*
1581 *Earth Environ*, <https://doi.org/10.1038/s43017-023-00464-3>, 2023.

1582 Yilmaz, M. T. and Crow, W. T.: The optimality of potential rescaling approaches in
1583 land data assimilation, *Journal of Hydrometeorology*, 14, 650–660, 2013.

1584 Yilmaz, M. T. and Crow, W. T.: Evaluation of Assumptions in Soil Moisture Triple
1585 Collocation Analysis, *Journal of Hydrometeorology*, 15, 1293–1302,
1586 <https://doi.org/10.1175/JHM-D-13-0158.1>, 2014.

1587 Yilmaz, M. T., Crow, W. T., Anderson, M. C., and Hain, C.: An objective
1588 methodology for merging satellite- and model-based soil moisture products, *Water*
1589 *Resources Research*, 48, n/a-n/a, <https://doi.org/10.1029/2011wr011682>, 2012.

1590 Yin, G. and Park, J.: The use of triple collocation approach to merge satellite- and
1591 model-based terrestrial water storage for flood potential analysis, *Journal of*

1592 Hydrology, 603, <https://doi.org/10.1016/j.jhydrol.2021.127197>, 2021.
1593 Yin, L., Tao, F., Chen, Y., Liu, F., and Hu, J.: Improving terrestrial evapotranspiration
1594 estimation across China during 2000–2018 with machine learning methods, *Journal of*
1595 *Hydrology*, 600, <https://doi.org/10.1016/j.jhydrol.2021.126538>, 2021.
1596 Zhang, Y., Leuning, R., Hutley, L. B., Beringer, J., McHugh, I., and Walker, J. P.:
1597 Using long-term water balances to parameterize surface conductances and calculate
1598 evaporation at 0.05 spatial resolution, *Water Resources Research*, 46, 2010.
1599 Zhang, Y., Kong, D., Gan, R., Chiew, F. H. S., McVicar, T. R., Zhang, Q., and Yang,
1600 Y.: Coupled estimation of 500 m and 8-day resolution global evapotranspiration and
1601 gross primary production in 2002–2017, *Remote Sensing of Environment*, 222, 165–
1602 182, <https://doi.org/10.1016/j.rse.2018.12.031>, 2019.
1603 Zhao, M., Liu, Y., and Konings, A. G.: Evapotranspiration frequently increases during
1604 droughts, *Nature Climate Change*, 1–7, 2022.
1605 Zhu, G., Li, X., Zhang, K., Ding, Z., Han, T., Ma, J., Huang, C., He, J., and Ma, T.:
1606 Multi-model ensemble prediction of terrestrial evapotranspiration across north China
1607 using Bayesian model averaging, *Hydrological Processes*, 30, 2861–2879,
1608 <https://doi.org/10.1002/hyp.10832>, 2016.
1609 Zwieback, S., Su, C.-H., Gruber, A., Dorigo, W. A., and Wagner, W.: The impact of
1610 quadratic nonlinear relations between soil moisture products on uncertainty estimates
1611 from triple collocation analysis and two quadratic extensions, *Journal of*
1612 *Hydrometeorology*, 17, 1725–1743, 2016.
1613